

Evanescent Field Interactions in the Scattering from Cylinders with Applications in Super-Resolution

by

Peter Cornelius Pawliuk

B.A.Sc., The University of British Columbia, 2010

A THESIS SUBMITTED IN PARTIAL FULFILLMENT OF
THE REQUIREMENTS FOR THE DEGREE OF

DOCTOR OF PHILOSOPHY

in

The Faculty of Graduate Studies

(Electrical Engineering)

THE UNIVERSITY OF BRITISH COLUMBIA

(Vancouver)

August 2013

© Peter Cornelius Pawliuk 2013

Abstract

The diffraction limit defines the maximum resolution of an imaging system that collects and focuses waves. This limited resolution arises from the finite length of the waves used to create the image. Therefore, the only way to increase the resolution is to use higher frequencies with shorter wavelengths. For situations in which increasing the frequency is not possible or not desirable, super-resolution imaging techniques can be applied to overcome the diffraction limit. Super-resolution is possible with the inclusion of evanescent waves, which exhibit unlimited spatial frequencies.

Evanescent waves decay exponentially away from their surface of origin so they are difficult to recover. One way to recover evanescent wave information is to scatter the wave from a small object. This scattering converts part of the evanescent wave into radiation that can propagate into the far-field where it can be detected. In order to characterize this conversion, the two-dimensional scattering of evanescent fields from a single cylinder and from multiple cylinders is investigated. The scattering models are derived using an analytical approach where the electromagnetic fields are broken down into cylindrical waves so that the boundary conditions on the cylinders can be applied directly. The incident field can be formulated from a vector plane-wave spectrum, which allows for an arbitrary combination of radiative and evanescent waves. Multiple cylinders of various sizes can be used to approximate the scattering from many two-dimensional objects. For simulating the imaging of objects buried underneath a surface, or near a planar interface, the model is separated into two dielectric half-spaces.

An example of a super-resolution application for these models is the sim-

ulation of apertureless near-field scanning optical microscopy (ANSOM). In ANSOM, a probe is placed in the extreme near-field of an object in order to scatter the evanescent fields that are formed by the illumination of the object. Images created by ANSOM are fundamentally different from traditional images and are difficult to interpret. The simulations provide insight into how the images are formed and what information they contain.

Preface

Published Works

Below is a list of publications arising from work presented in this thesis and the chapter in which the work is located.

- © 2009 OSA. Reprinted, with permission, from P. Pawliuk and M. Yedlin, “Gaussian beam scattering from a dielectric cylinder, including the evanescent region,” *J. Opt. Soc. Amer. A*, vol. 26, no. 12, pp. 2558-2566, 2009. Chapter 2
- © 2010 OSA. Reprinted, with permission, from P. Pawliuk and M. Yedlin, “Gaussian beam scattering from a dielectric cylinder, including the evanescent region: erratum,” *J. Opt. Soc. Amer. A*, vol. 27, no. 2, pp. 166, 2010. Incorporated into Chapter 2
- © 2010 OSA. Reprinted, with permission, from P. Pawliuk and M. Yedlin, “Truncating cylindrical wave modes in two-dimensional multiple scattering,” *Opt. Lett.*, vol. 35, no. 23, pp. 3997-3999, 2010. Chapter 3
- © 2011 OSA. Reprinted, with permission, from P. Pawliuk and M. Yedlin, “Scattering from cylinders using the two-dimensional vector plane-wave spectrum,” *J. Opt. Soc. Amer. A*, vol. 28, no. 6, pp. 1177-1184, 2011. Chapter 4
- © 2012 OSA. Reprinted, with permission, from P. Pawliuk and M. Yedlin, “Scattering from cylinders using the two-dimensional vector

plane-wave spectrum: addendum,” J. Opt. Soc. Amer. A, vol. 29, no. 3, pp. 352-353, 2012. Incorporated into Chapter 4

- © 2012 IEEE. Reprinted, with permission, from P. Pawliuk and M. Yedlin, “Scattering From Cylinders Near a Dielectric Half-Space Using a General Method of Images,” IEEE Trans. Antennas Propag., vol. 60, no. 11, pp. 5296 - 5304, 2012. Chapter 5
- © 2013 IEEE. Reprinted, with permission, from P. Pawliuk and M. Yedlin, “Multiple Scattering Between Cylinders in Two Dielectric Half-Spaces,” IEEE Trans. Antennas Propag., vol. 61, no. 8, pp. 4220 - 4228, 2013. Chapter 6

Collaboration

In the papers above, I collaborated with my supervisor Dr. Matthew Yedlin. I performed the background research and the analytical derivations, I programmed the simulations and interpreted the results, and I wrote and submitted the papers. Dr. Yedlin offered feedback, insight, and direction for my work, related my work to that of previous authors, and helped to edit the papers.

Table of Contents

Abstract	ii
Preface	iv
Table of Contents	vi
List of Tables	x
List of Figures	xi
List of Abbreviations	xvii
Acknowledgements	xviii
Dedication	xix
1 Introduction	1
1.1 Motivation: Super-Resolution	1
1.2 Scattering Models	3
1.2.1 Single Cylinder	5
1.2.2 Multiple Cylinders	8
1.2.3 Multiple Cylinders Near a Dielectric Half-Space	11
1.3 Sample Application: ANSOM	14
2 Gaussian Beam Scattering from a Dielectric Cylinder, Including the Evanescent Region	18

2.1	Introduction	18
2.2	Incident Electric Field	20
2.2.1	Radiated Field	24
2.2.2	Evanescent Field	25
2.3	Scattered and Transmitted Waves	28
2.4	Magnetic Fields	29
2.5	Applying Boundary Conditions	30
2.6	Numerical Simulations	31
2.6.1	Numerical Analysis for the Incident Radiated Field	31
2.6.2	Numerical Analysis of the Evanescent Region	35
2.6.3	Scattering Effect of the Evanescent Field Incident on the Cylinder	37
2.7	Conclusion	42
3	Truncating Cylindrical Wave Modes in Two-Dimensional Multiple Scattering	43
3.1	Introduction	43
3.2	Lower Bound Limit	44
3.3	Upper Bound Limit	46
3.4	Scattering Simulations	47
3.5	Conclusion	50
4	Scattering from Cylinders Using the Two-Dimensional Vector Plane-Wave Spectrum	51
4.1	Introduction	51
4.2	Incident Electric Fields	54
4.2.1	Incident Radiated Fields	58
4.2.2	Incident Evanescent Fields	58
4.3	Scattered Fields	59
4.4	Transmitted Fields	61
4.5	Boundary Conditions	61

4.6	T-Matrix Formulation	64
4.7	Numerical Simulations	67
4.8	Conclusion	73
5	Scattering from Cylinders Near a Dielectric Half-Space Using a General Method of Images	74
5.1	Introduction	74
5.2	Algorithm Outline	76
5.3	Scattering Theory	77
5.3.1	V^i - Incident Field	78
5.3.2	V^r - Incident Field Reflection	79
5.3.3	V^s - Scattered Fields from Cylinders	82
5.3.4	V^d - Diffracted Fields from the Planar Interface	82
5.3.5	V^t Transmitted Fields Inside the Cylinders	86
5.3.6	Applying the Cylinders' Boundary Conditions	86
5.4	Numerical Simulations	89
5.5	Conclusion	95
6	Multiple Scattering Between Cylinders in Two Dielectric Half-Spaces	98
6.1	Introduction	98
6.2	Scattering Theory	100
6.2.1	V_p Principal Field	103
6.2.2	V_s Scattered Field from a Cylinder	105
6.2.3	V_c Field Inside a Cylinder	106
6.2.4	V_r Reflection from Planar Interface	106
6.2.5	V_t Transmission through Planar Interface	107
6.2.6	Applying the Cylinders' Boundary Conditions	109
6.2.7	Stationary Phase Approximation	112
6.3	Numerical Simulations	115
6.4	Conclusion	123

7 Apertureless Near-Field Scanning Optical Microscopy Simulations	124
7.1 Introduction	124
7.2 The Reference Images	126
7.3 Interpreting Collected Data	129
7.4 Demodulation	133
7.5 Interference of Waves	137
7.6 Tip-Object Interaction	140
7.7 Probe to Object Distance	142
7.8 Wavelength and Object Parameters	143
7.9 Conclusion	147
8 Summary and Conclusions	149
8.1 Future Work	153
Bibliography	155
 Appendices	
A Diffraction Limit	168
B Truncating Cylindrical Wave Modes for Very Small Cylinders	171
C Convergence of Finite Element Method Comparison	173

List of Tables

2.1	Numerical Comparison between the Cartesian Formula (2.23) and the Cylindrical Wave Representation (2.22) for the Evanescent Field	37
5.1	The matrices are linked to their corresponding equations.	88
C.1	The mesh size parameters of the finite element method are compared to the resulting error.	173

List of Figures

1.1	A basic imaging setup is shown.	1
1.2	The progression of the scattering models is shown.	4
1.3	A simple ANSOM imaging setup is shown.	15
2.1	Coordinate system and layout for a Gaussian beam emitted from (y_0, z_0) at any angle θ^{in} . The dielectric cylinder with radius a_0 and permittivity ϵ_2 is centred at the origin. The exterior region has permittivity ϵ_1 . The x coordinate is perpendicular to the $y - z$ plane.	20
2.2	The integration contour follows the path 1-2-3-4. The points 1 and 4 extend infinitely, parallel to the imaginary axis.	23
2.3	Cylindrical wave coefficients for the evanescent field of a Gaussian beam centred about the origin with $\beta = 5$ at a frequency of 1 GHz. The coefficients are purely real.	26
2.4	Spatial convergence of the evanescent field with increasing Bessel modes N . The field is taken along the y' axis at $z' = 0$ for a Gaussian beam with $\beta = 5$ at a frequency of 1 GHz.	27
2.5	Incident radiated part of a Gaussian beam with $\beta = 2.5$ at a frequency of 1 GHz scattering from a dielectric cylinder with radius $a_0 = 0.3\text{m}$ and relative permittivity $\epsilon = 10$. Displayed are the (a) incident field, (b) scattered field, (c) transmitted field inside the cylinder, (d) total outside field (a)+(b), and (e) a scaled version of the transmitted field. (a), (b), (c), and (d) have the same scaling.	32

2.6	Incident radiated part of a Gaussian beam with $\beta = 2.5$ at a frequency of 1 GHz scattering from a dielectric cylinder with radius $a_0 = 0.3\text{m}$ and relative permittivity $\epsilon = 1000$. Displayed are the (a) incident field, (b) scattered field, (c) transmitted field inside the cylinder, (d) total outside field (a)+(b), and (e) a scaled version of the transmitted field. (a), (b), (c), and (d) have the same scaling.	33
2.7	Incident radiated part of a Gaussian beam with $\beta = 2.5$ at a frequency of 1 GHz scattering from a dielectric cylinder with radius $a_0 = 0.03\text{m}$ and relative permittivity $\epsilon = 1000$. Displayed are the (a) incident field, (b) scattered field, (c) transmitted field inside the cylinder, (d) total outside field (a)+(b), and (e) a scaled version of the transmitted field. (a), (b), (c), and (d) have the same scaling.	34
2.8	Evanescent field along the y' axis at $z' = 0$ for a Gaussian beam with $\beta = 5$ at a frequency of 1 GHz.	35
2.9	Evanescent field for a Gaussian beam with $\beta = 5$ at a frequency of 1 GHz, generated from the Cartesian formula (2.23).	36
2.10	Evanescent field for a Gaussian beam with $\beta = 5$ at a frequency of 1 GHz, generated from the cylindrical wave formula (2.22).	37
2.11	Evanescent part of a Gaussian beam with $\beta = 2.5$ at a frequency of 1 GHz scattering from a dielectric cylinder with radius $a_0 = 0.03\text{m}$ and relative permittivity $\epsilon = 1000$. Displayed are the (a) incident field, (b) scattered field, (c) transmitted field inside the cylinder, (d) total outside field (a)+(b), and (e) a scaled version of the transmitted field. (a), (b), (c), and (d) have the same scaling.	39
2.12	The scattered field from Figure 2.11 showing three time stamps (a)-(c).	40

2.13	The scattered field from Figure 2.11 displaying real and imaginary parts. The sectional view is taken along the z' axis on the far side of the cylinder.	40
2.14	Evanescent part of a Gaussian beam with $\beta = 2.5$ at a frequency of 1 GHz scattering from a dielectric cylinder with radius $a_0 = 0.3\text{m}$ and relative permittivity $\epsilon = 1000$. Displayed are the (a) incident field, (b) scattered field, (c) transmitted field inside the cylinder, (d) total outside field (a)+(b), and (e) a scaled version of the transmitted field. (a), (b), (c), and (d) have the same scaling.	41
3.1	The minimal accuracy mode limits M_v are displayed for ka_v factors that are (a) small, (b) medium, and (c) large.	45
3.2	Multiple scattering of a Gaussian beam from 11 perfectly conducting cylinders with broadside incidence.	48
3.3	Multiple scattering of a Gaussian beam from 11 perfectly conducting cylinders with in-line incidence.	48
3.4	Matrix condition number compared to the mode limit. The results are identical for broadside and in-line incidence.	49
4.1	Geometry and coordinate systems for the cylinders and the incident field. The x direction is perpendicular to the page. . .	54
4.2	Triangle showing the coordinates of transformation in the Graf addition theorem (4.24)	60
4.3	Setup for the numerical simulations. The grating is made up of 41 conducting cylinders with $a = 0.005\text{m}$. The dimensions are not drawn to scale.	67
4.4	Far-field intensity (W/m) plot for scattering of the incident field, with aperture distribution $E_x^i(0, y') = \exp(-j1.1ky')$, from the grating.	68

4.5	Far-field intensity (W/m) plot for scattering of the incident field, with aperture distribution $E_x^i(0, y') = \exp(-j1.4ky')$, from the grating.	69
4.6	Far-field intensity (W/m) plot for scattering of the incident field, with aperture distribution $E_x^i(0, y') = \exp(-j1.7ky')$, from the grating.	69
4.7	Far-field intensity (W/m) plot for scattering of the incident field, with aperture distribution $E_x^i(0, y') = \exp(-j2ky')$, from the grating.	70
4.8	Far-field intensity (W/m) polar plot for scattering of the evanescent field of a square shaped beam.	71
4.9	Far-field intensity (W/m) plot for scattering of the evanescent field of a square beam for $-\pi/2 \leq \theta \leq 0$	72
4.10	Absolute value of the spatial frequency content of the incident evanescent field from k to $2k$	73
5.1	The coordinate systems and geometry for the scattering are shown. The z direction is normal to the page. Image cylinder v is not shown.	77
5.2	The integration contour $C1$ follows the path 1-2-3-4. The contour $C2$ includes the paths 1-2 and 3-4 only. The points 1 and 4 extend infinitely, parallel to the imaginary axis.	83
5.3	A Gaussian beam is scattered from three identical dielectric cylinders near a dielectric half-space. The incident Gaussian beam has a waist size of $w_0 = 1$, an amplitude factor of $E_0 = 1$, and a frequency $f = 1GHz$ ($\lambda \approx 0.3m$).	90
5.4	The error in \vec{L} between the Fourier series method with evanescent field corrections (5.39) and the plane-wave integral method (5.38) is shown for TM and TE polarizations.	91

5.5	The error in \vec{L} between the Fourier series method with (5.39) and without (5.40) evanescent field corrections is shown for TM and TE polarizations.	92
5.6	The error in \vec{L} between the Fourier series method with and without the true evanescent field interaction term $\mathbf{U2}$ is shown for TM and TE polarizations.	94
6.1	The coordinate systems and geometry for the scattering are shown. The z direction is normal to the page. The indices w and i refer to cylinders in the first medium and the indices v and u refer to cylinders in the second medium.	101
6.2	The break down of electromagnetic fields is depicted.	102
6.3	The scattering setup for comparing the presented method with the finite element method is shown.	116
6.4	The electric field norm across the planar interface is shown for both the presented method and the finite element method. The two methods produce similar results.	117
6.5	The scattering setup for two cylinders being moved away from the interface is shown.	118
6.6	The error for the approximate matrices and the scattering coefficients is given for the case when both cylinders are moved away from the interface.	119
6.7	The error for the approximate matrices and the scattering coefficients is given for the case when only one cylinder is moved away from the interface.	120
6.8	The scattering setup for simulations involving four cylinders is shown.	121
6.9	The error for the approximate matrices and the scattering coefficients is given for the case when four cylinders are separated from each other in the y direction.	121

7.1	The scattering setup for the ANSOM simulations is shown but the dimensions are not to scale. The z direction is normal to the page. The wavelength in free space is λ	126
7.2	The probe-tip is scanned across the image plane and its scattered power is recorded to create simulated ANSOM images. .	128
7.3	The electromagnetic intensity is compared to the electric field intensity across the image plane. TM polarization is used. . .	130
7.4	The electromagnetic intensity is compared to the magnetic field intensity across the image plane. TE polarization is used.	132
7.5	The first, second, and third harmonic signals are demodulated using homodyne detection.	136
7.6	Altered ANSOM images are shown where the probe-tip samples only the scattered field from the object.	138
7.7	The ANSOM images for TM polarization with and without tip-object coupling are shown.	141
7.8	ANSOM images are shown for various distances separating the half-space and the probe. TE polarization was used.	143
7.9	The ANSOM images for TE polarization with different incident wavelengths are shown.	144
7.10	The ANSOM images for TE polarization with different object cylinder depths are shown.	145
7.11	The ANSOM images for TE polarization with different object cylinder radii are shown.	145
7.12	The ANSOM images for TE polarization with different object cylinder separation distances are shown.	146
A.1	A basic imaging setup is shown, copied from Figure 1.1.	168

List of Abbreviations

AFM atomic force microscope

ANSOM apertureless near-field scanning optical microscopy

DNG double negative materials

FFT fast Fourier transform

GLMT generalized Lorenz-Mie theory

GMI general method of images

GPR ground penetrating radar

MRI magnetic resonance imaging

NSOM near-field scanning optical microscopy

PEC perfect electric conductor

PEMC perfect electromagnetic conductor

PMC perfect magnetic conductor

TE transverse electric

TM transverse magnetic

VPWS vector plane-wave spectrum

Acknowledgements

I would like to acknowledge the mentoring provided by my supervisor Dr. Matthew Yedlin throughout the development of my research. His insight and guidance have been a fundamental source of support for me over the past few years. I am also grateful for useful discussions with Daryl Van Vorst.

Funding support for this research was provided by the Natural Sciences and Engineering Research Council of Canada.

To my father Reg Pawliuk for encouraging me to pursue this research.

Chapter 1

Introduction

1.1 Motivation: Super-Resolution

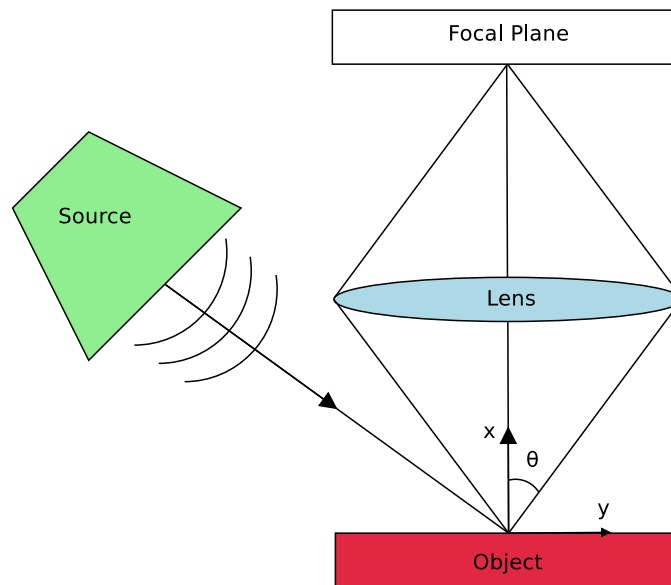


Figure 1.1: A basic imaging setup is shown.

A basic imaging setup is shown in Figure 1.1. The object to be studied is illuminated with waves by a source. The waves scatter from the object in all directions and some of these scattered waves are collected by the lens and refocused back onto the focal plane. The purpose of the imaging system is to reproduce, on the focal plane, the scattered fields emanating from the surface of the object. The wave distribution at the surface of the object contains valuable information about the size, shape, and properties of the

object. However, there are limitations on how well the imaging system can reproduce this distribution on the focal plane.

All imaging systems that use propagating waves to collect data are subject to a maximum resolution limit known as the diffraction limit. The diffraction limit was first described by Ernst Karl Abbe in the nineteenth century [1]. The diffraction limit defines the maximum resolution of an imaging system to be

$$d = \frac{\lambda}{2NA} \quad (1.1)$$

where λ is the wavelength and $NA = n \sin(\theta)$ is the numerical aperture of the imaging system. The numerical aperture depends on n , the refractive index of the background medium, and the half-angle θ shown in Figure 1.1. In the limit as the aperture becomes infinitely large or half-encircles the object, the diffraction limit becomes $d = \lambda/2$. A derivation of the diffraction limit using Fourier optics is provided in Appendix A.

Although the resolution at the focal plane is subject to the diffraction limit, the resolution of the wave-field at the surface of the object is unlimited. The wave-field must be capable of taking on an arbitrary form with unlimited spatial resolution in order to satisfy the object's boundary conditions during the scattering. Unlimited resolution cannot be satisfied by radiative waves alone, which have a maximum spatial frequency that is determined by their wavelength. However, unlimited higher spatial frequencies are possible with evanescent waves.

Evanescent waves are formed during scattering, and travel along the surface of objects. Evanescent waves are super-oscillatory along the source or scattering surface from which they originate; this means that their spatial frequency exceeds the wavenumber k [2]. It is this super-oscillatory property that allows evanescent waves to provide super-resolution. Away from the source or scattering surface, the evanescent waves die away exponentially. Evanescent waves store energy locally and do not transfer energy outward like radiation. Thus, the evanescent waves cannot be collected at the lens nor

recovered at the focal plane. Without these evanescent waves, an imaging system is said to be diffraction limited and cannot obtain resolution beyond $d = \lambda/2$.

If the data contained in the evanescent waves could be recovered, the resolution of an imaging system could be extended indefinitely. There are three primary methods for recovering evanescent field data: near-field detection, metamaterial super-lenses, and scattering. Near-field detection is simply attempting to measure the wave fields extremely close to the surface of the object where the evanescent waves have a significant presence. Metamaterial super-lenses are man-made materials that exhibit negative values of permittivity and permeability [3]. These super-lenses are able to convert the exponential decay of evanescent waves into exponential growth. The focus of this thesis is on the third method: the conversion of evanescent waves into radiation through scattering.

When an evanescent wave is incident upon a scattering body, part of its energy can be converted into radiation. This radiation can be collected in the far-field and used to recover the evanescent wave's super-resolution data. Several scattering models are developed to investigate and characterize the scattering of evanescent waves into radiation for applications in super-resolution imaging and focusing. The models are based on the two-dimensional scattering from cylinders.

1.2 Scattering Models

The scattering models developed in this thesis are analytical or a combination of analytical and numerical components. Analytical models were chosen because they provide more insight into the scattering interactions than purely numerical models. This is important when we are trying to characterize a specific interaction like the conversion of evanescent waves into radiation. Also, these analytical models do not require a spatial discretization, which

allows them to easily handle subwavelength phenomenon without resolution limits. The far-field data can also be obtained easily from the scattering solutions.

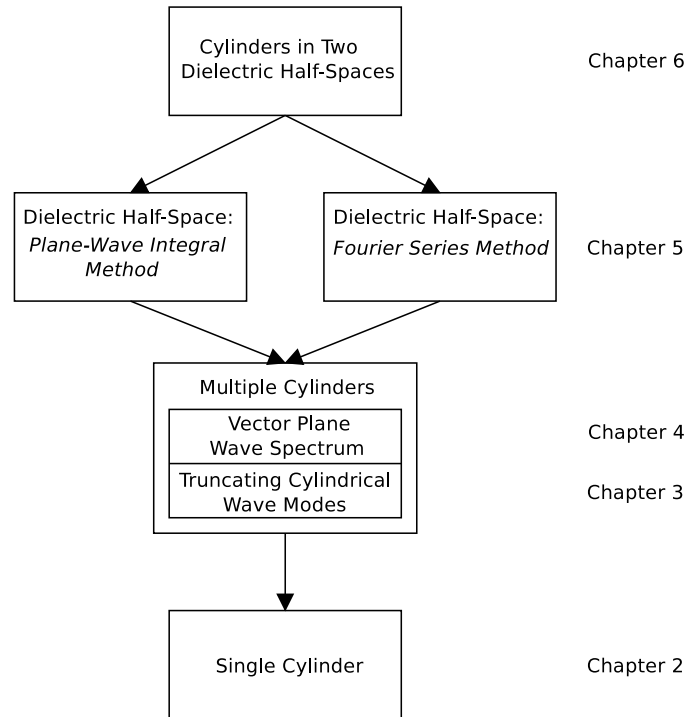


Figure 1.2: The progression of the scattering models is shown.

There are four scattering models that build on each other: the scattering from one cylinder in Chapter 2, the scattering from multiple cylinders in Chapter 4, the scattering from cylinders near a dielectric half-space in Chapter 5, and the scattering from cylinders on both sides of a dielectric half-space in Chapter 6. The progression of the scattering models is outlined in Figure 1.2. Finally, the scattering models are applied to ANSOM super-resolution imaging simulations in Chapter 7.

Building on the work of previous authors, these new scattering models introduce the scattering of evanescent fields and the extension to include cylinders on both sides of a dielectric half-space. In Chapters 2 and 4, inci-

dent field coefficients for evanescent fields are derived for the first time. In Chapters 5 and 6, the scattering models are extended to include a permeable half-space for simulating the imaging of buried objects or objects on a surface. There is a particular emphasis on near-field interactions and the modelling of evanescent waves.

1.2.1 Single Cylinder

Analytical solutions to Maxwell's equations for the scattering of electromagnetic waves from simple geometrical objects such as cylinders and spheres has been considered since the beginning of the twentieth century. The first analytical solutions for the scattering of a plane-wave from a sphere were produced by Mie [4] and Lorenz [5]. Mie produced his solution to the scattering problem in 1908, deriving his work from Maxwell's equations. Previously in 1890, Lorenz had produced an equivalent solution but had derived his work from a mechanical theory of aether [6]. Originally Mie theory, or Lorenz-Mie theory, referred to their analytical solution to the scattering from spherical particles. Today referring to Mie theory, or Lorenz-Mie theory, indicates that the scattering solution is based on the exact Maxwell's equations and an application of boundary conditions that involves separation of the coordinates. The advantages of such a solution include a fast computational implementation, an unbounded spatial domain, and a field representation in terms of scattering coefficients.

The first exact solutions of Maxwell's equations for the scattering from a single circular cylinder were presented by Lord Raleigh in 1918 [7]. Since then authors have considered many variations of this single scattering scenario. Cylinders with different electromagnetic properties have been considered, including conductors, homogeneous and inhomogeneous dielectrics, ferrite cylinders, meta-materials, anisotropic cylinders, cylindrical shells, and multilayered cylinders [8–10]. Variations on the geometrical setup, including oblique incidence, off-axis beam incidence, and elliptical cylinders, have

also been considered [11–14]. In each case the authors followed the same general approach that was instituted by Mie when he derived the scattering of a plane-wave from a sphere [4]. The exact Maxwell’s equations are applied to the fields and the boundary conditions are satisfied by separating the coordinates tangential to the surface of the cylinders.

The simplest case to consider for the scattering problem is that of plane-wave incidence. The incident plane-wave has a simple representation as a weighted sum of Bessel functions in cylindrical coordinates. For cylindrical scattering it is essential that the incident fields be expressed as an infinite sum of cylindrical wave modes using Bessel functions. This allows the boundary conditions to be applied to each mode separately, leading to a closed form solution for the scattering coefficients. The case of beam incidence is more complicated. For Gaussian beams, there is only an analytical solution for the paraxially approximated beam and its higher order corrections [15,16]. This is due to the fact that Maxwell’s equations cannot be solved exactly for such a beam. An exact representation for a Gaussian beam is possible through use of the plane-wave spectrum technique which represents an arbitrary electric field as an infinite sum of homogeneous and inhomogeneous plane-waves travelling in various directions [17]. The plane-wave spectrum integral, however, must be solved numerically as no closed form solution exists.

For the two-dimensional scattering from cylinders, a two-dimensional Gaussian beam is used. The two-dimensional beam is uniform in the direction of the cylinder axis. This simplification exploits the fact that the cylinder is also taken to be infinite and uniform along its axis. Using a three dimensional Gaussian beam severely complicates the scattering problem by introducing field components that are incident at an oblique angle to the cylinder.

Gaussian beam incidence upon an infinite circular cylinder was first considered by Alexopoulos and Park in 1972 [18]. Early work with Gaussian beams was difficult because the incident beam coefficients had to be numer-

ically computed as sums or integrals [12, 18]. In 1982 Kozaki [19] found a way to calculate the incident beam coefficients for a paraxial Gaussian beam using a closed form equation. The speed and accuracy of using this closed form expression over the previous integration or summation methods was immense. Kozaki [19, 20] also provided closed form equations for a second order paraxial approximation, and indicated a method for obtaining higher order corrections. However, the higher order corrections become tedious and inaccurate as the beam waist approaches the wavelength of radiation. The paraxial approximation, even at higher orders of correction, still completely eliminates the evanescent region and replaces it with erroneous results. For analysis of the evanescent fields, which become more significant as the beam waist decreases relative to the wavelength, the closed form solution provided by Kozaki cannot be used. Some authors noted this important limitation in their work and chose not to use a paraxial approximation [13].

In Chapter 2 an analysis is made of the full radiative and evanescent regions of a Gaussian beam scattering from a dielectric cylinder. Previous authors focused primarily on the scattering of radiative waves from a cylinder, whereas the focus of this analysis is on evanescent wave incidence. Incident field coefficients are developed for evanescent fields and their properties are examined. In the numerical simulations, the conversion of incident evanescent waves into radiation through scattering is demonstrated. This conversion is the mechanism responsible for spatial super-resolution. The use of a Gaussian beam was motivated by its ability to model more complicated field patterns by acting as a basis function [21]. However, if evanescent fields are to be included in the analysis of the Gaussian beam, then the plane-wave spectrum method must be used. The plane-wave spectrum then requires numerical integration which eliminates the benefit of using Gaussian beams as basis functions. Therefore, in our next model we use the vector plane-wave spectrum (VPWS) to create arbitrary radiative and evanescent fields.

1.2.2 Multiple Cylinders

Multiple scattering problems are significantly more involved than the single scattering case. In the single scattering case there are only two boundary condition equations and two unknowns, the scattering and transmission coefficients. Each cylindrical wave mode reacts independently in the scattering, allowing for a closed form solution. In the multiple scattering case we have an infinite matrix solution which accounts for the interaction of radiation coupling between cylinders. The use of the Graf addition theorem, for shifting cylindrical functions from one origin to another, causes the translated scattered fields to contain two infinite sums. Only one of these sums cancels in the application of the boundary conditions, leaving the other sum in the solution. The multiple scattering solution relates the scattering coefficients of each cylinder to those of every other cylinder.

The general solution to the multiple scattering of radiation from circular cylinders was first proposed by Twersky in 1952 [22]. Twersky's first mathematical derivation used a simplified approach where all the cylinders were perfectly conducting, although he mentions that his methods could be extended to include any cylinder type. His solution sought to calculate the excitation of one cylinder by combining the incident field and the scattered fields produced by the other cylinders. The boundary conditions are applied around each cylinder simultaneously and include the contributions from the scattered fields due to the presence of the other cylinders. The solution to the set of boundary condition equations is presented as an iterative procedure where each successive order of scattering is calculated from the previous order. The matrix solution was introduced in later work (1965) by Burke, Censor, and Twersky [23]. However, they applied the matrix solution to a more complicated scenario where the cylinders were of arbitrary shape rather than circular.

In 1970 Olaofe solved the boundary value problem for multiple circular cylinders to yield a solution in terms of an infinite set of linear equations [24,

25]. Olaofe states that these equations can be solved using matrix methods or iterative methods, as was done by Twersky [22,23]. The general equation for the infinite set of linear equations is presented but it is not broken down into a matrix solution. Olaofe used his solution to derive equations for the extinction, back-scattering cross section, and total-scattering cross section for the multiple scattering from circular cylinders.

Experimental results were compared to numerical simulations by Young and Bertrand in 1975 [26]. The multiple scattering from two cylinders with plane-wave illumination was investigated using the matrix inversion method, the iterative method and direct experimental measurement. They reported a good agreement between their calculations and their measurements. They noted that the matrix method was more efficient than the iterative method. The efficiency and accuracy of the matrix method in computing multiple scattering problems was confirmed by Elsherbeni [27] who compared it to the iterative method and two other computational electromagnetic techniques. The matrix method was shown to be the most flexible technique, as it can be applied to any scenario regardless of the cylinder radii and separation distance.

Later, these methods were expanded upon by many authors. The matrix method for multiple circular conducting cylinders was explicitly derived and numerically simulated by Ragheb and Hamid in 1985 [28]. They used the matrix method as a reference to compare other approximate methods to. Bever and Allebach [29] performed numerical simulations for the case of a planar array of dielectric cylinders. They used their results to investigate the convergence of the iterative method and the conditioning of the matrix method. Polewski [8] extended the scattering of a plane-wave by cylinders to include the effects of conducting, lossy dielectric, ferrite, and pseudo-chiral cylinders. Another advanced extension was given by Henin et al. [30], who extended the scattering geometry to include oblique incidence between the plane-wave and the cylinder axes.

To compute the scattering from multiple cylinders, the number of cylindrical wave modes used to model the scattered fields needs to be truncated. In Chapter 3 the truncation of cylindrical wave modes is considered in terms of model accuracy and matrix conditioning. If the number of modes is truncated too soon, the accuracy of the solution will be compromised. In multiple scattering, if the number of modes is truncated too late, the matrix inversion will become ill-conditioned, producing erroneous results. Therefore, in order to maximize the accuracy of the solution, it is necessary to have proper modal truncation. Since, the modal truncation is primarily dependant on the size of the cylinder relative to the wavelength, it may be necessary to have separate truncation limits for each cylinder involved in the scattering. This analysis is applicable to all cylindrical scattering models and helps to maximize the accuracy of the solutions.

Gaussian beam illumination in the multiple scattering from circular cylinders was first investigated by Kojima et al. [31], and also by Sugiyama and Kozaki [32]. Sugiyama and Kozaki used the matrix inversion technique to calculate the scattering of a Gaussian beam from two cylinders of different radii. They also performed experiments to verify their results. Kojima et al. investigated higher order beam modes [31]. For a Gaussian beam scattering from dielectric cylinders, Yokota et al. [33] derived the matrix solution and applied it to a scenario with eight cylinders. Elsherbeni et al. also considered this problem but used the iterative procedure [34]. Most authors used the paraxial Gaussian beam representation which contains no evanescent field components [31–33]. Only Yang et al. [35] provided a means of including the evanescent components into their multiple scattering solution.

Using plane-waves and Gaussian beams, previous authors have primarily focused on radiative incidence. In Chapter 4 the vector plane-wave spectrum (VPWS) is scattered from multiple dielectric and conducting cylinders. The VPWS allows for both polarization states and arbitrary radiative and evanescent components in the incident field. The scattering of evanescent

waves from arrays of cylinders is particularly important for applications in super-resolution imaging and microwave source location. Fink et al. [36] and Lerosey et al. [37] demonstrated that an array of cylindrical scatterers could partially convert an evanescent field into radiation and vice-versa. By using time-reversal techniques, they were able to differentiate signals sent to antennas that were spaced only $\lambda/30$ apart. Malyuskin and Fusco [38] also demonstrated subwavelength source resolution using cylindrical near-field scatterers.

1.2.3 Multiple Cylinders Near a Dielectric Half-Space

To simulate a more realistic imaging setup, a dielectric half-space was incorporated into the scattering model. This model allows the imaging of objects on top or inside of a substrate to be simulated. The scattering from buried cylinders is important for applications such as ground penetrating radar (GPR), detection of underground landmines, tunnels, conduits, and pipes, underground communications, and biological imaging [39–41]. In Chapter 7, the scattering models we present will be applied to imaging simulations of apertureless near-field scanning optical microscopy (ANSOM), which is described in Section 1.3.

The introduction of a perfectly conducting plane into the multiple scattering geometry is easily incorporated through the method of images. The method of images allows the multiple scattering between the conducting plane and the cylinders to be modelled by the interaction of the real cylinders with image cylinders. Twersky used the method of images to model a single cylinder above a conducting plane as the scattering from two cylinders [42]. Bertrand and Young [43] also used the method of images for cylindrical scattering and compared it to experimental results. The scattering from cylinders partially buried in a conducting plane was investigated by Rao and Barakat [44, 45].

For dielectric half-spaces, the reflection of waves depends on the angle of

incidence. Vdeen and Ngo [46] used an approximate method of images for dielectric half-spaces, where all the incident waves were assumed to strike at normal incidence. This approximation is only accurate when the cylinders are sufficiently separated from the planar interface. Coatanhay and Conoir [47, 48] developed a more accurate general method of images (GMI) for cylinders in front of a dielectric half-space. The GMI uses a Fourier series to convert the plane-wave reflection coefficients for the planar interface into a cylindrical form. In this form, a modified image cylinder can be represented using a cylindrical reflection coefficient matrix. This solution accounts for the angular dependence of the reflections from the planar interface but is limited for evanescent waves. Depending on the form of the plane-wave reflection coefficients, the Fourier series will only converge for a certain range of the complex angles that arise in evanescent waves.

A solution that is valid for all evanescent wave interactions is made possible through the use of the plane-wave integral method. The Sommerfeld integral is used to convert cylindrical waves into a sum of plane-waves [49], so that the planar reflection coefficients can be applied directly. This method is accurate for small distances between the cylinders and the dielectric half-space, however, it requires a significant amount of numerical integration [50, 51]. Frezza et al. [52] presented the scattering from multiple cylinders near a vacuum-plasma interface using a general approach that could be applied to any reflective planar surface. The scattering of a single conducting cylinder in front of a generally reflective planar surface was presented by Borghi et al. [53] and subsequently extended to multiple cylinders [54].

In Chapter 5 the Fourier series method is derived along side the plane-wave integral method in order to compare the two methods. Using a Fourier series to transform the reflection coefficients is applied in vector electromagnetic scattering for the first time. The Fourier series method is much faster and more intuitive to implement than the plane-wave integration method, but may cause errors for evanescent waves coupling between the cylinders

and the planar interface. Evanescent field correction terms are derived for the Fourier series method to correct for these errors. Simulations for both polarizations demonstrate the convergence of the Fourier series method as the cylinders are separated from the interface.

The case of a buried cylinder can be considered if the incident field originates in the half-space that does not contain the cylinders. Ciambra et al. [40] considered a cylindrical wave approach for the scattering from a single cylinder buried in a dielectric half-space. This was extended to multiple cylinders by Di Vico et al. [55]. The scattering of a perfect electromagnetic conductor (PEMC) cylinder buried in a dielectric half-space was considered by Ahmed and Naqvi [39]. Lee and Grzesik [56] derived a solution for the scattering from multilayered cylinders buried in a dielectric half-space with oblique incidence. For the buried case, the incident field must be transmitted into the second half-space before the scattering is considered. The transmission of the cylinders' scattered fields back into the first half-space is also considered using the Sommerfeld integral to convert cylindrical waves into plane-waves.

The scattering from cylinders embedded in a finite dielectric slab is even more complicated because of the infinite number of reflections within the slab. Frezza et al. derived an algorithm for the scattering from multiple cylinders embedded in a dielectric slab, for both conducting [57] and dielectric [41] cylinders. In these algorithms, the number of multiple reflections within the dielectric slab must be truncated to a finite amount. Lee [58] derived a similar solution for the scattering from multilayered cylinders embedded in a dielectric slab with oblique incidence.

The scattering from cylinders on both sides of a dielectric half-spaces is introduced in Chapter 6. In previous work, all the cylinders have been contained in one of the two half-spaces or inside of a slab. This new scattering algorithm accounts for the multiple scattering interactions between cylinders on opposite sides of a dielectric half-space. To avoid the numerical integration that arises from the plane-wave spectrum of cylindrical waves, the method

of stationary phase is employed. This method provides an accurate approximation when the cylinders are sufficiently separated from the interface. The numerical simulations demonstrate the accuracy of the approximation in different scenarios.

The final model presented in Chapter 6 is suitable for simulating ANSOM with a probe on one side of the dielectric half-space and buried objects on the other side. These simulations are presented in Chapter 7, and are used as an example of how these models can be useful in super-resolution applications. There are many other applications for these models including the analysis of metamaterials and photonic crystals, and ground penetrating radar (GPR) simulations, which are discussed briefly in Section 8.1.

1.3 Sample Application: ANSOM

In 1928, Synge [59] proposed a subwavelength imaging system that used a small hole punched in a metallic plate. A subwavelength portion of an object could be illuminated by placing the plate in the near-field of the object. These early subwavelength images were produced using near-field scanning techniques at microwave frequencies. Ash and Nicholls [60] built a near-field scanning microscope that used a small hole in a thin diaphragm to illuminate a subwavelength portion of an object. The object was vibrated at a specific frequency in order to differentiate the small scattering effect amid the large background radiation signal. Their experiments demonstrated resolution capabilities of $\lambda/60$. They concluded with the suggestion of adapting their techniques for infrared or optical frequencies.

Near-field scanning optical microscopy (NSOM) techniques were developed later using subwavelength illumination or collection methods [61]. For the illumination method, a small aperture is fabricated at the end of an optical fiber, which allows objects to be illuminated by a subwavelength focal spot. The aperture is scanned across the image and the scattered power from

the object is collected to recreate an image. For the collection method, the objects are illuminated from the far-field and the small aperture is used to collect the scattered fields from a subwavelength spot on the objects. The size of the subwavelength aperture determines the resolution of the device but is limited by the skin depth of the metal aperture. The apertures are scanned across a two-dimensional plane and the data is collected one pixel at a time. Three imaging modes can be used in NSOM: constant height, constant intensity, and constant distance [61, 62]. In the constant height mode, the probe is scanned across a flat plane above the base of the object. In constant intensity mode, the probe is forced to adjust its height above the object such that the measured intensity is kept constant. In constant distance mode, the probe follows the contours of the object with the separation distance being fixed. The resolution of these methods is in the range of 30-100nm [63–65].

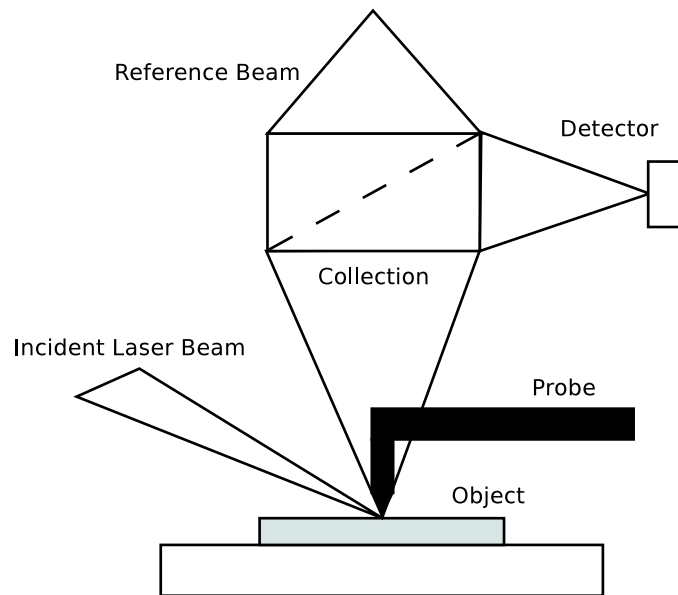


Figure 1.3: A simple ANSOM imaging setup is shown.

Apertureless near-field scanning optical microscopy (ANSOM) is the most

powerful of the subwavelength imaging techniques because the probe-tip does not need an aperture, and therefore it can be much finer [63, 66]. A basic imaging setup for ANSOM is shown in Figure 1.3. In ANSOM, the probe is just a metallic or semiconductor rod with an extremely fine tip. This rod is vibrated in the direction normal to the object's surface so that the scattered power from the probe-tip can be demodulated and distinguished from the background signal. An atomic force microscope (AFM) is used to perform the modulation and to calculate the distance from the probe-tip to the surface of the object. When used together, the AFM and ANSOM techniques provide both the topographical and optical properties of the object [66]. Surface plasmon waves are often used to obtain a field enhancement at the apex of the probe-tip, which greatly improves the signal to noise ratio [67]. The resolution limits of ANSOM have been reported around 3-10nm [63, 64].

The net effect of the demodulation in ANSOM is believed to be proportional to the scattered power emanated by the probe-tip [68, 69]. The probe-tip scatters light from the extreme near-field of the object, which contains strong evanescent field components. These evanescent fields are converted into radiation by the probe, transmitted to the far-field, and recorded by the detector. The evanescent field conversion is responsible for the increase in spatial resolution of the images. The background signal is much greater than the small modulation of the probe-tip's scattered field, which makes the data collection difficult. By adding a strong reference signal with a controllable phase, the background signal can be suppressed through homodyne detection. This method of measurement also allows for phase recovery [70, 71]. Using a florescent tip in order to separate the probe-tip's scattered field through frequency differentiation has also been proposed [65].

Subwavelength images are useful in many fields including research, medicine, and manufacturing. Because of their ability to extract electromagnetic fields with high precision, they have been useful for characterizing surface plasmon polaritons in nano-devices [64]. This has been particularly important for

chemical and biochemical sensors that depend on plasmon resonance shifts and local field enhancements [71].

In Chapter 7, the cylindrical scattering models are used to provide simulations of ANSOM images. The insight provided by these analytical scattering models is exploited to characterize and interpret the images.

Chapter 2

Gaussian Beam Scattering from a Dielectric Cylinder, Including the Evanescent Region

2.1 Introduction

In this paper we will investigate the scattering of a two-dimensional Gaussian beam from a homogeneous dielectric cylinder. The effects of the evanescent field incident on the cylinder will be a key aspect of our analysis.

Much work on the scattering of electromagnetic waves from cylinders and spheres has already been conducted. In 1908, Gustav Mie published a famous paper on the interaction of a plane-wave and a sphere [4]. Because of a prior version of similar work by Lorenz [5], the theory became known as Lorenz-Mie theory, or in the case of an arbitrary beam, generalized Lorenz-Mie theory (GLMT). An in-depth history of the GLMT has been produced by Gouesbet [6]. A general theoretical framework for the scattering of an arbitrarily shaped beam by an infinite cylinder has also been given by Gouesbet [72]. Practical Gaussian beam models with simulations have been produced by Ren et al. [73] and Mees et al. [74]. These authors use the Davis framework for representing the Gaussian beam. The Davis framework does not satisfy Maxwell's equations, but it approaches a correct solution to Maxwell's equations at higher orders [73]. This paper does not utilize the Davis framework.

Gaussian beams are most commonly analyzed in their paraxial form. This

form may be derived by approximating a plane-wave spectrum as being focused over a small angular range [75]. Many previous authors [9, 10, 12, 20, 76] have ignored the evanescent field by using such a paraxial approximation. This approximation eliminates the evanescent field entirely. Other authors [13, 34] used a plane-wave spectrum approach that did not include a description of the beam coefficients A_n in the evanescent region. Yang et al. [35] mentions that the evanescent field scattering from a dielectric cylinder creates propagating harmonics. However, they conclude that the evanescent field effects are insignificant for their application and can be ignored.

In this paper we will fully analyze the cylindrical beam coefficients A_n so that we can compute the full scattering effect of the evanescent field. This computation is important when the evanescent field is converted into a significant propagating field. For completeness we will allow the beam to have any initial offset (y_0, z_0) and any angle of propagation θ^{in} . The layout and coordinate system are shown in Figure 2.1. We will begin by deriving solutions to the wave equation for the incident, scattered, and transmitted waves. Then to solve the scattering problem we will equate the electromagnetic boundary conditions at the cylinder surface $\rho = a_0$. The final results will include numerical simulations of the scattering of the radiated field and of the evanescent field.

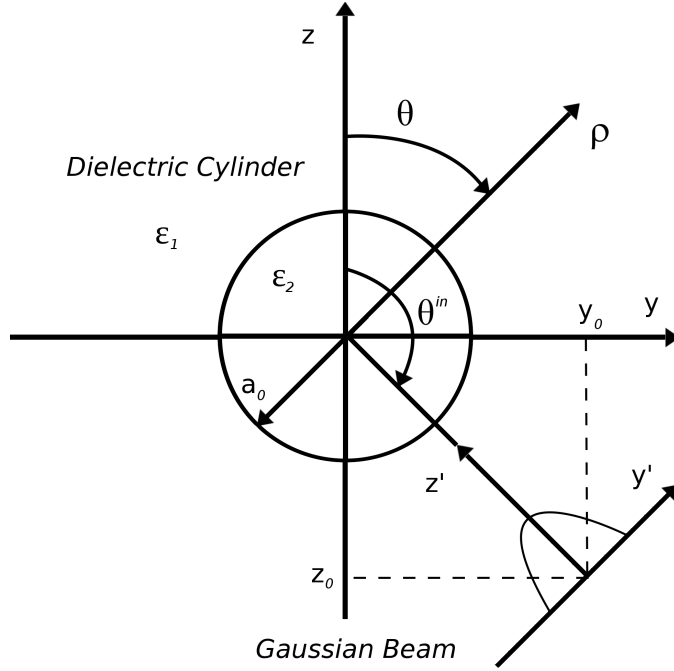


Figure 2.1: Coordinate system and layout for a Gaussian beam emitted from (y_0, z_0) at any angle θ^{in} . The dielectric cylinder with radius a_0 and permittivity ϵ_2 is centred at the origin. The exterior region has permittivity ϵ_1 . The x coordinate is perpendicular to the $y - z$ plane.

2.2 Incident Electric Field

The incident electric field can be represented by a plane-wave spectrum with a Gaussian aperture distribution [17]. First we start with a two-dimensional plane-wave spectrum equation for a wave travelling in the z' direction from an arbitrary point (y_0, z_0) as shown in Figure 2.1. For now we will use the altered coordinate system (x, y', z') . We will be using transverse magnetic (TM) polarization with the electric field in the x direction tangential to the cylinder at all points. In the three-dimensional Gaussian beam case, a planar polarization cannot satisfy Maxwell's equations [77]. Since we are using a two-dimensional Gaussian beam, we are able to use a planar polarization and

still satisfy Maxwell's equations.

Our plane-wave spectrum is given by (2.1), where α and γ are the y' and z' components of the wave-vector \mathbf{k} , respectively:

$$E_x^i(y', z') = \frac{\exp(j\omega t)}{2\pi} \int_{-\infty}^{\infty} F(\alpha) \exp[-j(\alpha y' + \gamma z')] d\alpha. \quad (2.1)$$

When $|\alpha| > k$, we have entered the evanescent region where the plane-waves are inhomogeneous and decay exponentially away from the y' axis [78, 79]. This exponential decay in the direction of propagation means that the evanescent field will be significant in magnitude only close to the beam origin. To ensure that the evanescent field decays exponentially we need to adopt the correct sign conventions when we define γ in (2.2). Note that the evanescent region is only valid in one half-space $z' \geq 0$:

$$\gamma = \begin{cases} \sqrt{k^2 - \alpha^2} & |\alpha| \leq k \\ -j\sqrt{\alpha^2 - k^2} & |\alpha| > k \quad z' \geq 0 \end{cases} \quad (2.2)$$

The function $F(\alpha)$ is known as the angular spectrum of the field and can be computed [78, 79] by taking the inverse Fourier transform of the aperture distribution $f(y')$:

$$F(\alpha) = \int_{-\infty}^{\infty} f(y') \exp(j\alpha y') dy'. \quad (2.3)$$

The aperture distribution is the electric field taken across the y' axis at $z' = 0$, or

$$f(y') = E_x^i(y', 0). \quad (2.4)$$

We will define our Gaussian aperture distribution as

$$f(y') = E_0 \exp[-(\beta y')^2]. \quad (2.5)$$

Here β is the inverse of the beam width at (y_0, z_0) and E_0 is the amplitude

constant. Using our Gaussian distribution (2.5) to calculate the angular spectrum (2.3) we obtain the following result:

$$F(\alpha) = E_0 \frac{\sqrt{\pi}}{\beta} \exp\left(-\frac{\alpha^2}{4\beta^2}\right). \quad (2.6)$$

Now we substitute (2.6) into our plane-wave spectrum (2.1):

$$E_x^i(y', z') = \frac{E_0 \exp(j\omega t)}{2\sqrt{\pi}\beta} \int_{-\infty}^{\infty} \exp\left[-\frac{\alpha^2}{4\beta^2} - j(y'\alpha + z'\sqrt{k^2 - \alpha^2})\right] d\alpha. \quad (2.7)$$

Equation (2.7) contains the full description of a two-dimensional Gaussian beam in Cartesian coordinates. This representation satisfies Maxwell's equations, since its divergence is zero and it obeys the Helmholtz equation.

Holding to our sign conventions in (2.2) we will now convert our variable of integration in (2.7) into an angular function:

$$\sin(\phi) = \frac{\alpha}{k}, \quad (2.8)$$

with

$$\cos(\phi) = \begin{cases} \sqrt{1 - \sin^2(\phi)} & \sin^2(\phi) \leq 1 \\ -j\sqrt{\sin^2(\phi) - 1} & \sin^2(\phi) > 1 \quad z' \geq 0 \end{cases}, \quad (2.9)$$

to obtain

$$E_x^i(y', z') = \frac{E_0 k \exp(j\omega t)}{2\sqrt{\pi}\beta} \int_{-\pi/2 - j\infty}^{\pi/2 + j\infty} \exp\left\{-\frac{k^2 \sin^2(\phi)}{4\beta^2} - jk[y' \sin(\phi) + z' \cos(\phi)]\right\} \cos(\phi) d\phi, \quad (2.10)$$

where the integration contour is shown in Figure 2.2.

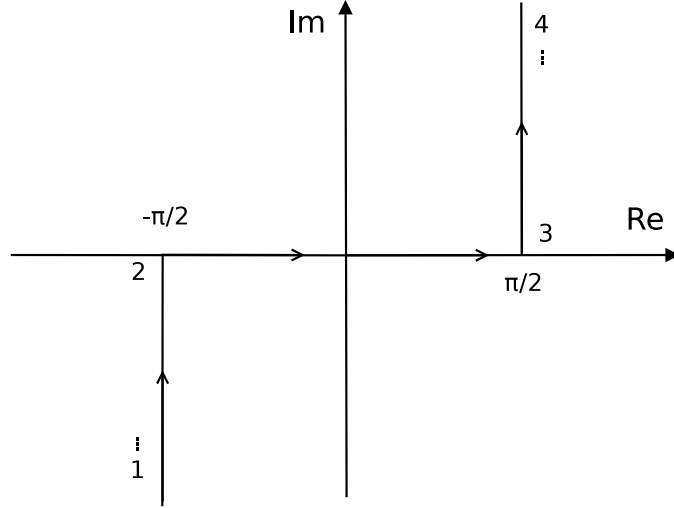


Figure 2.2: The integration contour follows the path 1-2-3-4. The points 1 and 4 extend infinitely, parallel to the imaginary axis.

Now we will transform the coordinates (x, y', z') into (x, ρ, θ) using (2.11) and (2.12) [35, 80]:

$$y' = -[\rho \sin(\theta) - y_0] \cos(\theta^{in}) + [\rho \cos(\theta) - z_0] \sin(\theta^{in}), \quad (2.11)$$

$$z' = -[\rho \sin(\theta) - y_0] \sin(\theta^{in}) - [\rho \cos(\theta) - z_0] \cos(\theta^{in}). \quad (2.12)$$

After simplifying the exponentials using trigonometric identities we obtain

$$E_x^i(\rho, \theta) = \frac{E_0 k \exp(j\omega t)}{2\sqrt{\pi}\beta} \int_{-\pi/2-j\infty}^{\pi/2+j\infty} \exp\left[-\frac{k^2 \sin^2(\phi)}{4\beta^2} + jk\rho \cos(\theta - \theta^{in} - \phi) - jk\rho_0 \cos(\theta_0 - \theta^{in} - \phi)\right] \cos(\phi) d\phi. \quad (2.13)$$

According to the restrictions in (2.9), the electric field in (2.13) is valid only in the region $z' \geq 0$. The equation will be invalid for $z' < 0$ because the evanescent field will not decay exponentially in that region.

Using Bessel function expansions [81], we can define the following identity:

$$\exp[jk\rho \cos(\theta - \theta^{in} - \phi)] = \sum_{n=-\infty}^{\infty} j^n \exp[jn(\theta - \theta^{in} - \phi)] J_n(k\rho). \quad (2.14)$$

Now we can represent our Gaussian beam as a sum of cylindrical waves (2.15) with weights (2.16):

$$E_x^i(\rho, \theta) = \exp(j\omega t) \sum_{n=-\infty}^{\infty} j^n \exp(jn\theta) J_n(k\rho) A_n, \quad (2.15)$$

$$A_n = \frac{E_0 k \exp(-jn\theta^{in})}{2\sqrt{\pi}\beta} \int_{-\pi/2-j\infty}^{\pi/2+j\infty} \exp\left[-\frac{k^2 \sin^2(\phi)}{4\beta^2} - jn\phi - jk\rho_0 \cos(\theta_0 - \theta^{in} - \phi)\right] \cos(\phi) d\phi. \quad (2.16)$$

2.2.1 Radiated Field

The radiated field corresponds to $|\alpha| \leq k$ or $|\sin(\phi)| \leq 1$, so we can separate the radiated portion of the beam shape coefficients (2.16) from the evanescent part:

$$A_n^{rad} = \frac{E_0 k \exp(-jn\theta^{in})}{2\sqrt{\pi}\beta} \int_{-\pi/2}^{\pi/2} \exp\left[-\frac{k^2 \sin^2(\phi)}{4\beta^2} - jn\phi - jk\rho_0 \cos(\theta_0 - \theta^{in} - \phi)\right] \cos(\phi) d\phi. \quad (2.17)$$

Inside the radiated region there are only real angles so all the functions are bounded. There is no analytical solution to the integral in (2.17) so it must be computed numerically.

2.2.2 Evanescent Field

The evanescent field coefficients corresponds to $|\alpha| > k$ or $|\sin(\phi)| > 1$ in (2.16):

$$A_n^{evan} = \frac{E_0 k \exp(-jn\theta^{in})}{2\sqrt{\pi}\beta}. \quad (2.18)$$

$$\int_{\pi/2}^{\pi/2+j\infty} \exp\left[-\frac{k^2 \sin^2(\phi)}{4\beta^2} - jn\phi - jk\rho_0 \cos(\theta_0 - \theta^{in} - \phi)\right] \cos(\phi) d\phi +$$

$$\frac{E_0 k \exp(-jn\theta^{in})}{2\sqrt{\pi}\beta}.$$

$$\int_{-\pi/2-j\infty}^{-\pi/2} \exp\left[-\frac{k^2 \sin^2(\phi)}{4\beta^2} - jn\phi - jk\rho_0 \cos(\theta_0 - \theta^{in} - \phi)\right] \cos(\phi) d\phi.$$

We can simplify and combine the integrals in (2.18) by transforming the variables of integration. In the positive region $(\pi/2, \pi/2 + j\infty)$ we will use transformation (2.19), and in the negative region $(-\pi/2, -\pi/2 - j\infty)$ we will use transformation (2.20):

$$\phi = \frac{\pi}{2} + ju, \quad (2.19)$$

$$\phi = -\frac{\pi}{2} - ju. \quad (2.20)$$

After simplifying (2.18) we obtain

$$A_n^{evan} = \frac{E_0 k \exp(-jn\theta^{in})}{2\sqrt{\pi}\beta}. \quad (2.21)$$

$$\int_0^\infty \exp\left[-\frac{k^2 \cosh^2(u)}{4\beta^2}\right] \sinh(u) \{j^{-n} \exp[nu - jk\rho_0 \sin(\theta_0 - \theta^{in} - ju)] +$$

$$j^n \exp[-nu + jk\rho_0 \sin(\theta_0 - \theta^{in} + ju)]\} du.$$

The coefficients in the evanescent region A_n^{evan} increase exponentially for higher modes n . This behaviour is caused by the exponential growth of the field in the region $z' < 0$. However, the field is still valid in the $z' > 0$ region. We can see the general form of the coefficients $j^n A_n^{evan}$, which are purely real,

in Figure 2.3.

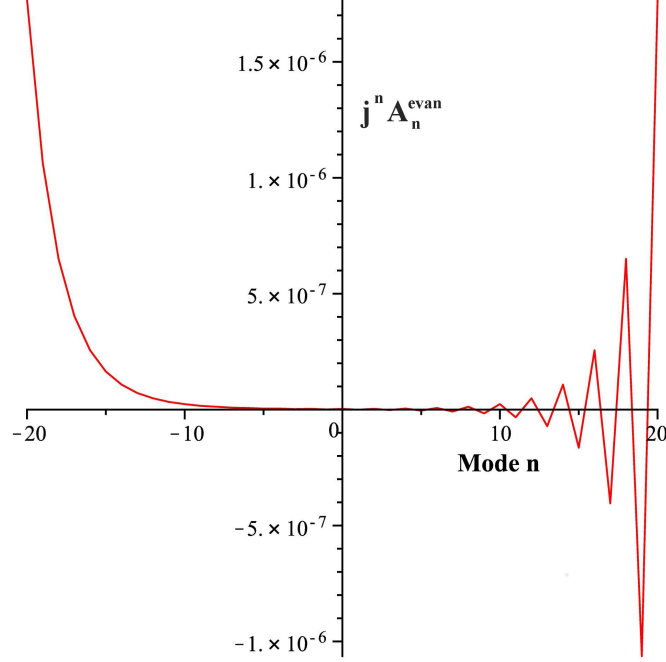


Figure 2.3: Cylindrical wave coefficients for the evanescent field of a Gaussian beam centred about the origin with $\beta = 5$ at a frequency of 1 GHz. The coefficients are purely real.

When numerically evaluating the evanescent field, the number of modes must be limited to some maximum value N :

$$E_x^{evan}(\rho, \theta) = \exp(j\omega t) \sum_{n=-N}^N j^n \exp(jn\theta) J_n(k\rho) A_n^{evan}. \quad (2.22)$$

The evanescent field in the $z' \geq 0$ region converges spatially as the number of modes N increases. This means that for a given number of modes N , the evanescent field given by (2.22) will converge within a specific radius $\rho < \rho_{conv}$. In Figure 2.4 we can see that as N is increased the field converges spatially outward. This convergence is similar to the convergence of the Taylor series of a sine or cosine. The spatial convergence of the evanescent

field makes it hard to compute the field at large distances from the origin. However, in general, the field in this region will have died off exponentially and become insignificant.

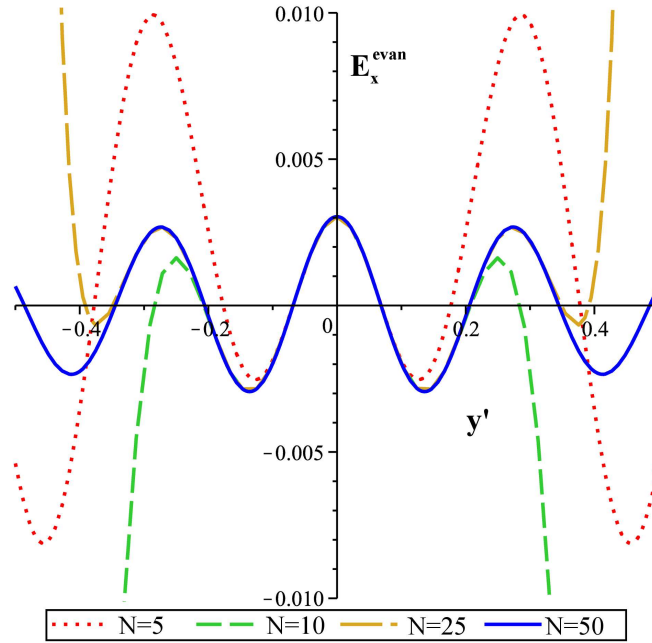


Figure 2.4: Spatial convergence of the evanescent field with increasing Bessel modes N . The field is taken along the y' axis at $z' = 0$ for a Gaussian beam with $\beta = 5$ at a frequency of 1 GHz.

As a reference, for accurate modelling of the entire evanescent region, we can use Cartesian coordinates. To obtain the evanescent field in Cartesian coordinates from (2.7) we limit the range of integration to $|\alpha| > k$

$$E_x^{evan}(y', z') = \frac{E_0 \exp(j\omega t)}{\sqrt{\pi}\beta} \int_k^\infty \exp\left(-\frac{\alpha^2}{4\beta^2} - z'\sqrt{\alpha^2 - k^2}\right) \cos(y'\alpha) d\alpha. \quad (2.23)$$

The advantage of using Cartesian coordinates is that the field no longer has spatial convergence issues. Our equations of coordinate transformation from

(x, y', z') to (x, y, z) are given by

$$y' = -(y - y_0) \cos(\theta^{in}) + (z - z_0) \sin(\theta^{in}), \quad (2.24)$$

$$z' = -(y - y_0) \sin(\theta^{in}) - (z - z_0) \cos(\theta^{in}). \quad (2.25)$$

To evaluate (2.23) the integral needs to be integrated numerically, as there is no analytical solution. For numerical integration, the upper integration limit must be truncated to $k \leq \alpha \leq \alpha_{max}$, where α_{max} depends on the beam width variable β . Larger values of β will demand a larger α_{max} value for accurate results.

2.3 Scattered and Transmitted Waves

The general solution of the wave equation in cylindrical coordinates is given by

$$E = \exp(\pm j\omega t) \exp(\pm jn\theta) [R J_n(k\rho) + S Y_n(k\rho)]. \quad (2.26)$$

Both the transmitted and scattered fields must be a weighted sum of cylindrical waves of this form.

For the transmitted field we must have $S = 0$ because Y_n is divergent for arguments approaching zero [82]. Therefore, the transmitted field (2.27) will have only J_n terms with weights $j^n C_n$:

$$E_x^t = \exp(j\omega t) \sum_{n=-\infty}^{\infty} j^n \exp(jn\theta) J_n(\sqrt{\epsilon} k\rho) C_n, \quad (2.27)$$

$$\epsilon = \epsilon_2 / \epsilon_1. \quad (2.28)$$

The scattered field is composed entirely of outward travelling waves that

are known to be represented by Hankel functions, where $H_n^{(2)}(x) = J_n(x) - j Y_n(x)$. The scattered field is represented as a sum of Hankel functions with weights $j^n B_n$:

$$E_x^s = \exp(j\omega t) \sum_{n=-\infty}^{\infty} j^n \exp(jn\theta) H_n^{(2)}(k\rho) B_n. \quad (2.29)$$

2.4 Magnetic Fields

To obtain the magnetic fields we use the Maxwell-Faraday law:

$$\nabla \times \mathbf{E} = -\frac{\partial \mathbf{B}}{\partial t}. \quad (2.30)$$

Since we have only an x component in the electric field, the curl simplifies to

$$\nabla \times \mathbf{E} = \left(\frac{1}{\rho} \frac{\partial E_x}{\partial \theta}\right) \hat{\rho} + \left(-\frac{\partial E_x}{\partial \rho}\right) \hat{\theta}. \quad (2.31)$$

After computation the resultant magnetic fields are as follows:

$$\begin{aligned} \mathbf{H}^i = & -\frac{\exp(j\omega t)}{\rho\omega\mu} \sum_{n=-\infty}^{\infty} j^n n \exp(jn\theta) J_n(k\rho) A_n \hat{\rho} \\ & -\frac{\exp(j\omega t)k}{\omega\mu} \sum_{n=-\infty}^{\infty} j^{n+1} \exp(jn\theta) J_n'(k\rho) A_n \hat{\theta}, \end{aligned} \quad (2.32)$$

$$\begin{aligned} \mathbf{H}^s = & -\frac{\exp(j\omega t)}{\rho\omega\mu} \sum_{n=-\infty}^{\infty} j^n n \exp(jn\theta) H_n^{(2)}(k\rho) B_n \hat{\rho} \\ & -\frac{\exp(j\omega t)k}{\omega\mu} \sum_{n=-\infty}^{\infty} j^{n+1} \exp(jn\theta) H_n^{(2)'}(k\rho) B_n \hat{\theta}, \end{aligned} \quad (2.33)$$

$$\mathbf{H}^t = -\frac{\exp(j\omega t)}{\rho\omega\mu} \sum_{n=-\infty}^{\infty} j^n n \exp(jn\theta) J_n(\sqrt{\epsilon}k\rho) C_n \hat{\rho} \quad (2.34)$$

$$-\frac{\exp(j\omega t)\sqrt{\epsilon}k}{\omega\mu} \sum_{n=-\infty}^{\infty} j^{n+1} \exp(jn\theta) J_n'(\sqrt{\epsilon}k\rho) C_n \hat{\theta}.$$

The primes on the Hankel and Bessel functions denote a derivative with respect to the whole argument.

2.5 Applying Boundary Conditions

To find the unknown coefficients B_n and C_n , we need to apply the boundary conditions at the interface of the cylinder and the surrounding medium $\rho = a_0$. At this interface, the tangential components of the electric field and magnetic field must be continuous:

$$E_x^i(a_0, \theta) + E_x^s(a_0, \theta) = E_x^t(a_0, \theta), \quad (2.35)$$

$$H_\theta^i(a_0, \theta) + H_\theta^s(a_0, \theta) = H_\theta^t(a_0, \theta). \quad (2.36)$$

Below are the expressions for the coefficients derived from the boundary conditions (2.35) and (2.36):

$$B_n = \frac{J_n(\sqrt{\epsilon}ka_0)J_n'(ka_0) - J_n(ka_0)J_n'(\sqrt{\epsilon}ka_0)\sqrt{\epsilon}}{\sqrt{\epsilon}J_n'(\sqrt{\epsilon}ka_0)H_n^{(2)}(ka_0) - J_n(\sqrt{\epsilon}ka_0)H_n^{(2)'}(ka_0)} A_n, \quad (2.37)$$

$$C_n = \frac{2j/(\pi ka_0)}{\sqrt{\epsilon}J_n'(\sqrt{\epsilon}ka_0)H_n^{(2)}(ka_0) - J_n(\sqrt{\epsilon}ka_0)H_n^{(2)'}(ka_0)} A_n. \quad (2.38)$$

We now have the full solution to our scattering problem. The results for the coefficients B_n (2.37) and C_n (2.38) are identical to those of previous authors [13, 20, 35].

2.6 Numerical Simulations

There are many unique situations in which we can apply the techniques we have derived. These situations include large/small cylinders, wide/narrow beam widths, normal/offset incidence, and high/low permittivity contrasts. All these factors will affect the fields that are produced in the scattering.

Simulations have been performed to determine the effects of a dielectric cylinder on the electromagnetic fields of a Gaussian beam. For completeness, simulations of incident radiated and evanescent waves have been included. A numerical analysis comparing the evanescent field in Cartesian coordinates with the cylindrical wave representation was also performed in order to show the convergence of the field. In all the subsequent figures an arrow displays the direction of incident beam propagation.

2.6.1 Numerical Analysis for the Incident Radiated Field

Within the radiated region we will analyze three cases. The first case involves a large cylinder $a_0 = 0.3\text{m}$ with a relative permittivity of $\epsilon = 10$. The second case uses the same size cylinder but with a relative permittivity of $\epsilon = 1000$. The third case uses a small cylinder $a_0 = 0.03\text{m}$ with the same permittivity as the second case. For all three cases the incident beam is identical with $\beta = 2.5$ at a frequency of 1GHz

The results of the simulations for the first case are shown in Figure 2.5. From the scattered field we can see that cylindrical waves are generated that propagate outward in all directions from the cylinder. The high scattered amplitude on the far side of the cylinder creates a cancellation of the incident field in order that a shadow may be created. Inside the cylinder we can see that there are six wave peaks [see figure 4e], which is consistent with the size of the cylinder and the relative wave speed. From the total outer field we note that there are high peaks of radiation on the illuminated side of the

cylinder.

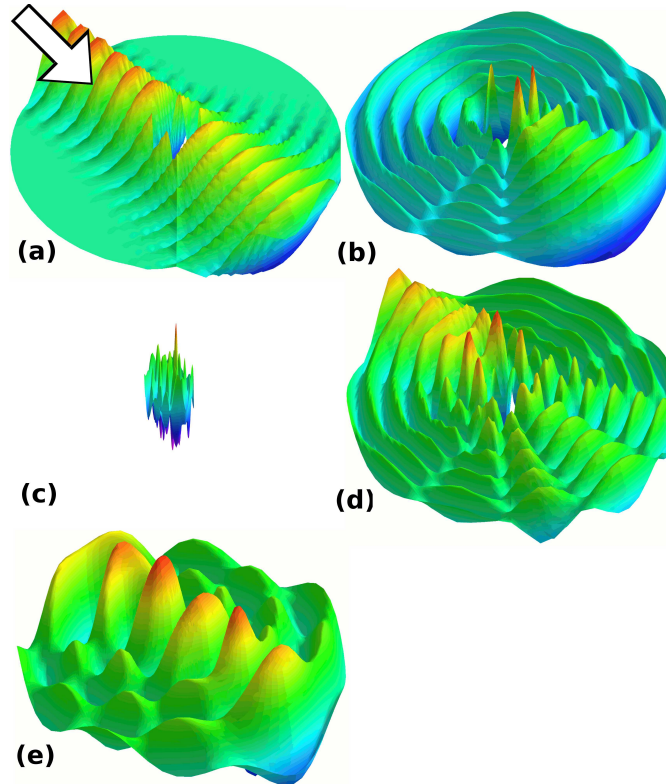


Figure 2.5: Incident radiated part of a Gaussian beam with $\beta = 2.5$ at a frequency of 1 GHz scattering from a dielectric cylinder with radius $a_0 = 0.3\text{m}$ and relative permittivity $\epsilon = 10$. Displayed are the (a) incident field, (b) scattered field, (c) transmitted field inside the cylinder, (d) total outside field (a)+(b), and (e) a scaled version of the transmitted field. (a), (b), (c), and (d) have the same scaling.

The second case is shown in Figure 2.6. By comparing these results with those of the first case, we can determine the effects of increasing the dielectric permittivity. The high permittivity cylinder causes stronger reflection and weaker transmission. In the total outer field we can see that the region behind the cylinder is lower in amplitude; it has become a stronger shadow region. Inside the cylinder there are many waves because the wave speed is

31.6228 times slower. The large reduction in speed inside the cylinder also causes a focusing effect. The incident waves are focused toward the centre of the cylinder and then dispersed.

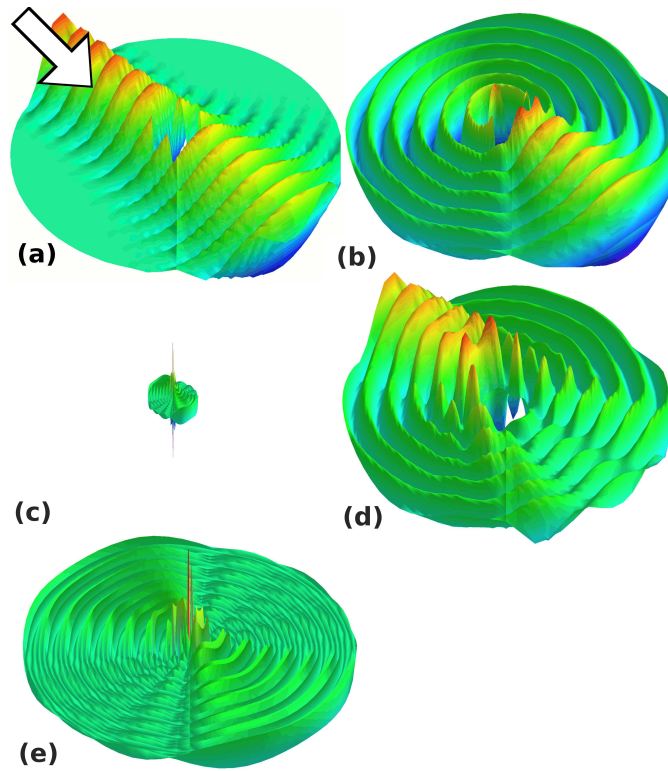


Figure 2.6: Incident radiated part of a Gaussian beam with $\beta = 2.5$ at a frequency of 1 GHz scattering from a dielectric cylinder with radius $a_0 = 0.3\text{m}$ and relative permittivity $\epsilon = 1000$. Displayed are the (a) incident field, (b) scattered field, (c) transmitted field inside the cylinder, (d) total outside field (a)+(b), and (e) a scaled version of the transmitted field. (a), (b), (c), and (d) have the same scaling.

Case three is displayed in Figure 2.7. We have now reduced the cylinder radius by 10 times, so that it is much smaller than one wavelength of radiation in the surrounding medium. The scattered field is becoming cylindrically symmetric. In our previous simulations, the cylinder had multiple radiation

phases incident on its surface at any time. Now the radiation phase incident on the outside of the cylinder is nearly the same at all points. This causes the field to permeate the cylinder uniformly as inward travelling cylindrical waves.

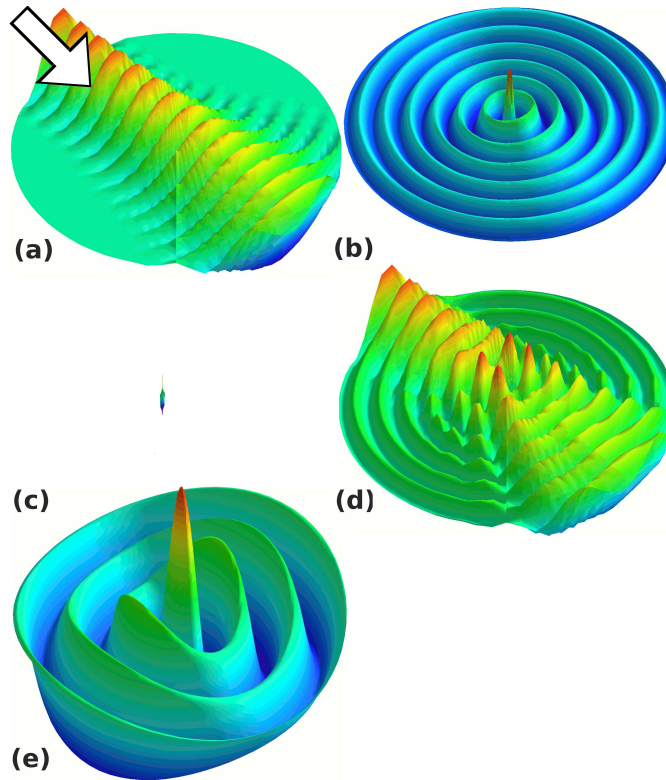


Figure 2.7: Incident radiated part of a Gaussian beam with $\beta = 2.5$ at a frequency of 1 GHz scattering from a dielectric cylinder with radius $a_0 = 0.03\text{m}$ and relative permittivity $\epsilon = 1000$. Displayed are the (a) incident field, (b) scattered field, (c) transmitted field inside the cylinder, (d) total outside field (a)+(b), and (e) a scaled version of the transmitted field. (a), (b), (c), and (d) have the same scaling.

2.6.2 Numerical Analysis of the Evanescent Region

First, we analyze the evanescent region in the Cartesian coordinates of (2.23), as it will stand as a reference for us to compare the cylindrical wave case with. All of the following simulations were performed with a frequency of 1GHz and a beam width variable $\beta = 5$.

Figure 2.8 and Figure 2.9 show the general shape of a Gaussian beam's evanescent field. The evanescent field has a Gaussian envelope in the y' direction (see Figure 2.8) and decays exponentially in the positive and negative z' directions (see Figure 2.9). The evanescent field has only a real part and therefore oscillates like a standing wave without propagating. The maximum amplitude of this evanescent field is approximately 0.003 for an amplitude constant $E_0 = 1$. The distance between peaks comparable to the wavelength of the radiation.

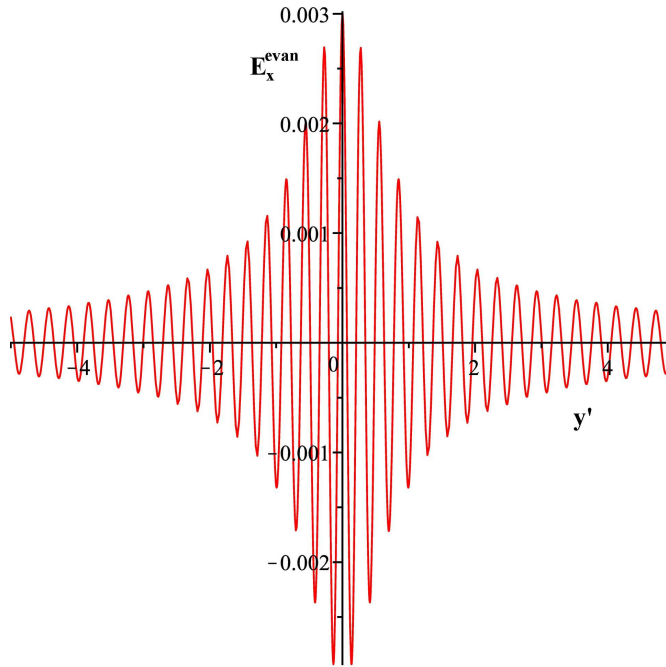


Figure 2.8: Evanescent field along the y' axis at $z' = 0$ for a Gaussian beam with $\beta = 5$ at a frequency of 1 GHz.

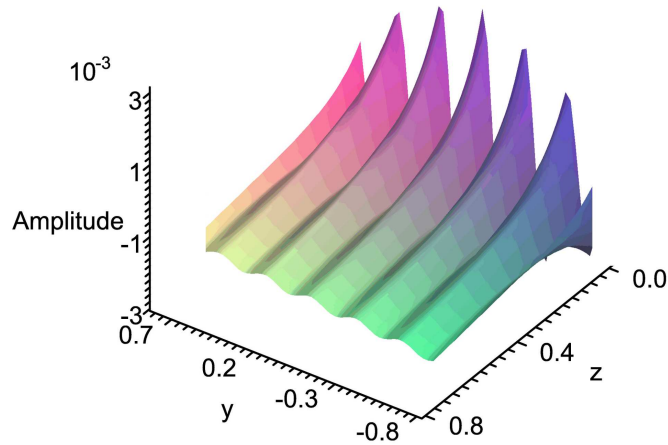


Figure 2.9: Evanescent field for a Gaussian beam with $\beta = 5$ at a frequency of 1 GHz, generated from the Cartesian formula (2.23).

Now we will compare the results obtained in the Cartesian analysis with equivalent simulations using our cylindrical wave representation from (2.22). Table 2.1 compares the fields produced by the cylindrical wave formula (2.22) within the convergent region $\rho < \rho_{conv}$, with those of the Cartesian formula (2.23). The results from the two formulas within the convergent region are extremely close. The tiny percentage of error is most likely due to the imperfection of numerical integration. An evanescent field plot from the cylindrical wave equation is shown in Figure 2.10 and can be compared with the equivalent Cartesian plot in Figure 2.9.

Table 2.1: Numerical Comparison between the Cartesian Formula (2.23) and the Cylindrical Wave Representation (2.22) for the Evanescent Field

y'	z'	Cartesian	Cylindrical Waves $N = 100$
0	0	$3.036954670 \times 10^{-3}$	$3.036954703 \times 10^{-3}$
0	0.1	$1.420888146 \times 10^{-3}$	$1.420888145 \times 10^{-3}$
0	0.2	$7.718096192 \times 10^{-4}$	$7.718096156 \times 10^{-4}$
0	0.3	$4.680267318 \times 10^{-4}$	$4.680267350 \times 10^{-4}$
0	0.4	$3.080132582 \times 10^{-4}$	$3.080132516 \times 10^{-4}$
0.1	0	$-1.978901439 \times 10^{-3}$	$-1.978901438 \times 10^{-3}$
0.2	0	$-3.710670998 \times 10^{-4}$	$-3.710670940 \times 10^{-4}$
0.3	0	$2.217569218 \times 10^{-3}$	$2.217569234 \times 10^{-3}$
0.4	0	$-2.250000000 \times 10^{-3}$	$-2.250344039 \times 10^{-3}$

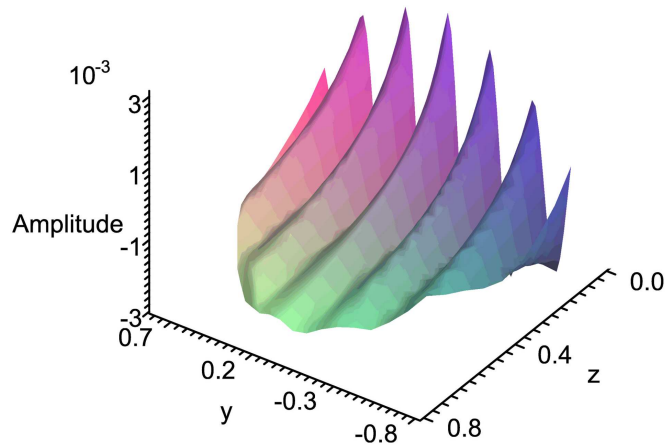


Figure 2.10: Evanescent field for a Gaussian beam with $\beta = 5$ at a frequency of 1 GHz, generated from the cylindrical wave formula (2.22).

2.6.3 Scattering Effect of the Evanescent Field Incident on the Cylinder

Two cases were simulated for the evanescent field scattering from a dielectric cylinder. The first case involves a small cylinder $a_0 = 0.03\text{m}$ with relative permittivity $\epsilon = 1000$. The second case has a larger cylinder $a_0 = 0.3\text{m}$ with

the same permittivity. The Gaussian beam used to model these simulations is the same as in the radiation simulations above. The distance from the cylinder edge to the beam origin is fixed at 0.7m so that enough evanescent field amplitude remains to enable us to visualize the scattering.

The results of the simulation for the first case are shown in Figure 2.11. The scattered field displayed in three time frames in Figure 2.12 demonstrates that propagating cylindrical waves are formed by the reflections at the cylinder boundary. Figure 2.13 plots the real and imaginary parts of the scattered field on the far side of the cylinder. The incident evanescent field contains a real part only. From Figure 2.13 we can see that an imaginary component 90° out of phase with the real component has been introduced. These newly formed radiating waves have the same frequency as the original Gaussian beam; there are no harmonics. The amplitude of this radiation approaches the amplitude of the evanescent field at the cylinder boundary asymptotically as the relative permittivity of the cylinder is increased. The phase of the radiation at the cylinder boundary also shifts asymptotically to 180° as the permittivity is increased.

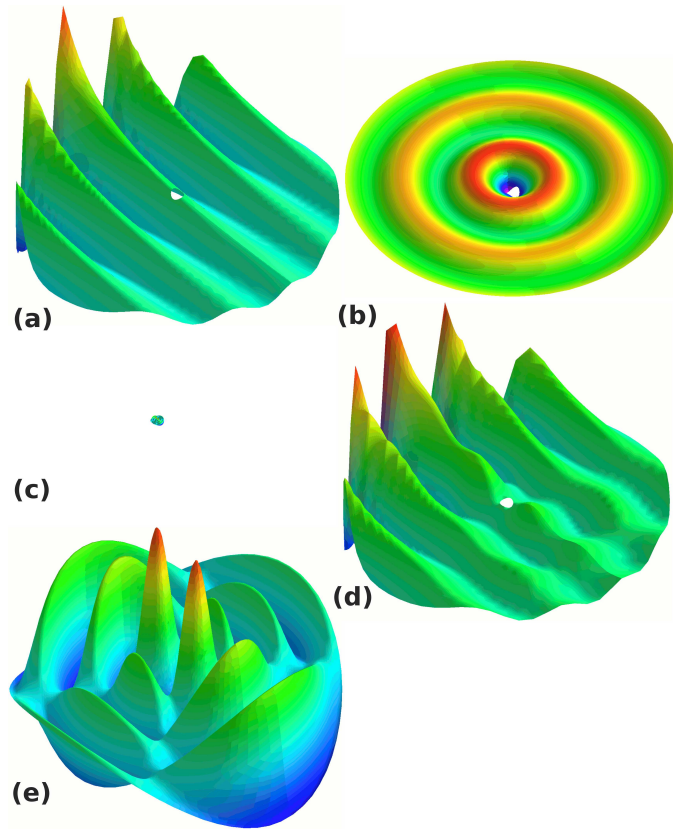


Figure 2.11: Evanescent part of a Gaussian beam with $\beta = 2.5$ at a frequency of 1 GHz scattering from a dielectric cylinder with radius $a_0 = 0.03\text{m}$ and relative permittivity $\epsilon = 1000$. Displayed are the (a) incident field, (b) scattered field, (c) transmitted field inside the cylinder, (d) total outside field (a)+(b), and (e) a scaled version of the transmitted field. (a), (b), (c), and (d) have the same scaling.

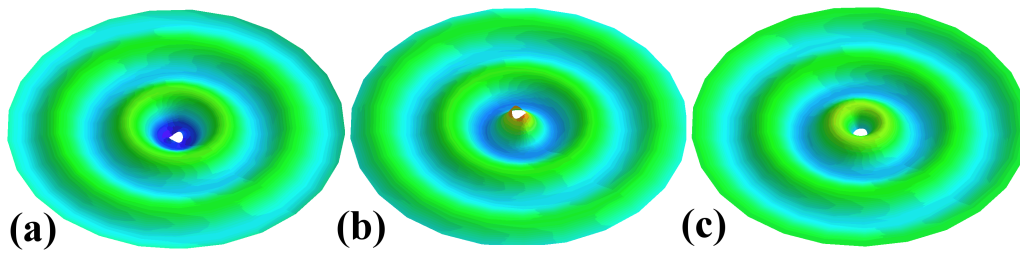


Figure 2.12: The scattered field from Figure 2.11 showing three time stamps (a)-(c).

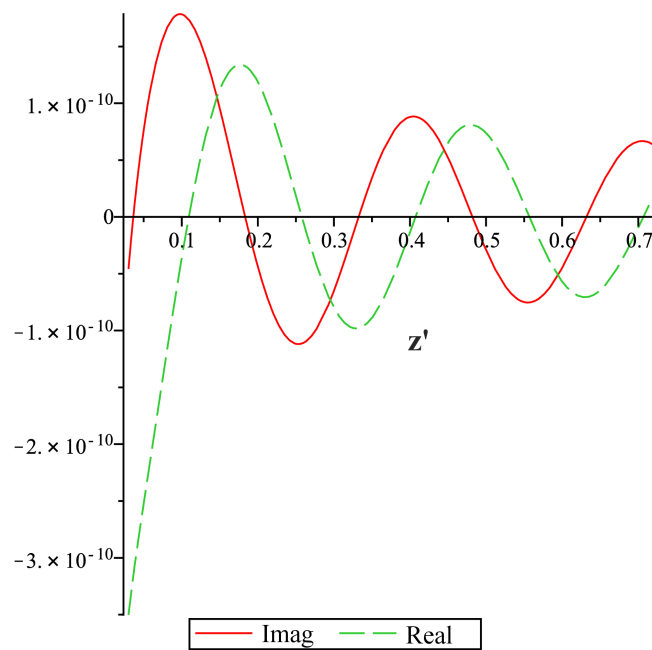


Figure 2.13: The scattered field from Figure 2.11 displaying real and imaginary parts. The sectional view is taken along the z' axis on the far side of the cylinder.

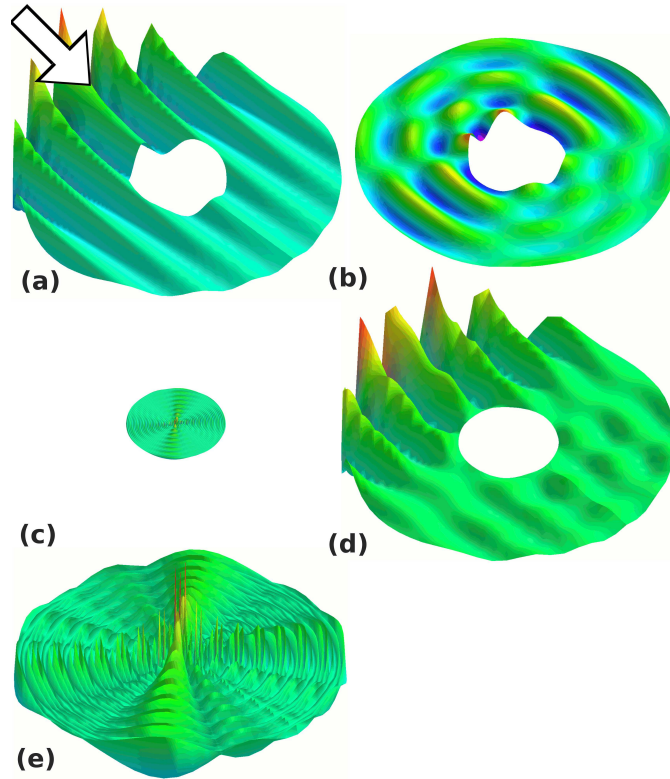


Figure 2.14: Evanescent part of a Gaussian beam with $\beta = 2.5$ at a frequency of 1 GHz scattering from a dielectric cylinder with radius $a_0 = 0.3\text{m}$ and relative permittivity $\epsilon = 1000$. Displayed are the (a) incident field, (b) scattered field, (c) transmitted field inside the cylinder, (d) total outside field (a)+(b), and (e) a scaled version of the transmitted field. (a), (b), (c), and (d) have the same scaling.

The second case is shown in Figure 2.14. The scattered field still contains propagating waves in the case of the large cylinder. The wave interference effects taking place in the scattered and transmitted fields are qualitatively the same as in the previous case. The only difference is that the scattered waves are not as uniformly distributed as in the small cylinder case.

2.7 Conclusion

A full analysis, including the evanescent region, of a two-dimensional Gaussian beam scattering from a homogeneous dielectric cylinder was performed. For the radiated region the results were common to those of other papers [10, 13, 20]. The calculation and analyses performed within the evanescent region provided a more complete description of the scattered fields. We were able to obtain expressions for the evanescent field in Cartesian coordinates and in cylindrical coordinates as a sum of weighted cylindrical waves. Within the evanescent region the sum of weighted cylindrical waves was found to converge spatially outward as we increased the number of Bessel modes. The evanescent field scattering from a dielectric cylinder was shown to create propagating waves in all directions. This scattering takes energy that is normally stored in the near-field of the incident Gaussian beam and transforms it into radiation energy. The strength of these newly formed propagating waves depends on the amplitude of the evanescent field incident on the cylinder surface and on the permittivity of the dielectric cylinder. To maximize this radiating effect one would place a high permittivity cylinder as close to the beam origin as possible.

Chapter 3

Truncating Cylindrical Wave Modes in Two-Dimensional Multiple Scattering

3.1 Introduction

The two-dimensional multiple scattering of plane-waves and Gaussian beams by infinite circular cylinders has been considered by several authors [24, 26–29, 83]. The technique involves representing the incident, scattered, and transmitted waves as infinite sums of cylindrical wave modes:

$$E(\rho_v, \theta_v) = \exp(j\omega t) \sum_{n=-\infty}^{\infty} j^{-n} \exp(jn\theta_v) Z_n(k\rho_v) {}_v b_n, \quad (3.1)$$

with coefficients ${}_v b_n$. The function Z is a Bessel function of the first kind for incident and transmitted fields and for scattered fields it is a Hankel function. Once in this form, the boundary conditions can be applied at the surface of each cylinder and solved in terms of a matrix inversion. However, in order to calculate the scattering matrix or any of the electromagnetic fields, the infinite sum of cylindrical wave modes must be truncated to some maximum magnitude limit M_v . A unique M_v may be used for each cylinder v involved in the multiple scattering. In this chapter we discuss how the background wavenumber k , the cylinder radii a_v , the inter-cylinder separation d , and the cylinder permittivities ϵ_v define appropriate upper and lower bounds on the

limit M_v .

Many previous authors chose the limit M_v by iteratively analyzing the convergence of a given scattering setup [29, 83]. Others chose to make linear estimates, which are good for mid-range ka_v values [26–28]. For dielectric cylinders, Elsherbeni [27] suggests the use of $M_v \approx 3k_v a_v$, which becomes excessive for large ϵ . For conducting cylinders, Ragheb and Hamid [28] used $M_v \approx 3ka_v$, with the restriction that ka_v is reasonably large. For two cylinders, Young and Bertrand [26] suggest using $M_v \approx 2ka_v$ when the cylinders are sufficiently separated $d \gg a$. They also indicate that for low values of ka_v , five to ten extra modes are necessary.

3.2 Lower Bound Limit

The lower bound limit of M_v is necessitated by the fact that we need enough modes to represent the electromagnetic fields at the cylinder boundary with sufficient precision. This limit is determined solely by the wavenumber k in the surrounding medium and the radius of the cylinders a . The factor ka_v determines the bounds beyond which further cylindrical wave modes become severely attenuated in the scattering. The lower bound mode limit for accuracy will be similar for the single and multiple scattering cases because we can consider the multiple scattering case in terms of its iterative solution. The iterative solution involves recursively applying the single scattering solution to obtain a convergent total field. Every time the single scattering solution is applied, the same range of modes will be attenuated due to the ka_v factor. By analyzing the single scattering coefficients of conducting (3.2) and dielectric (3.3) cylinders with the incident field coefficient factor removed,

$${}_v f_n = -\frac{J_n(ka_v)}{H_n^{(2)}(ka_v)}, \quad (3.2)$$

$${}_v f_n = \frac{J_n'(ka_v) J_n(\sqrt{\epsilon_{rv}} ka_v) - \sqrt{\epsilon_{rv}} J_n(ka_v) J_n'(\sqrt{\epsilon_{rv}} ka_v)}{\sqrt{\epsilon_{rv}} H_n^{(2)}(ka_v) J_n'(\sqrt{\epsilon_{rv}} ka_v) - H_n^{(2)'}(ka_v) J_n(\sqrt{\epsilon_{rv}} ka_v)}, \quad (3.3)$$

we can determine proper lower bound mode limits for various values of ka_v . The single scattering coefficients (3.2) and (3.3) apply to transverse magnetic (TM) polarization, where the electric field is directed along the cylinder axes. For transverse electric (TE) polarization, the mode limits are similar except for the case of extremely small cylinders which is covered in appendix B.

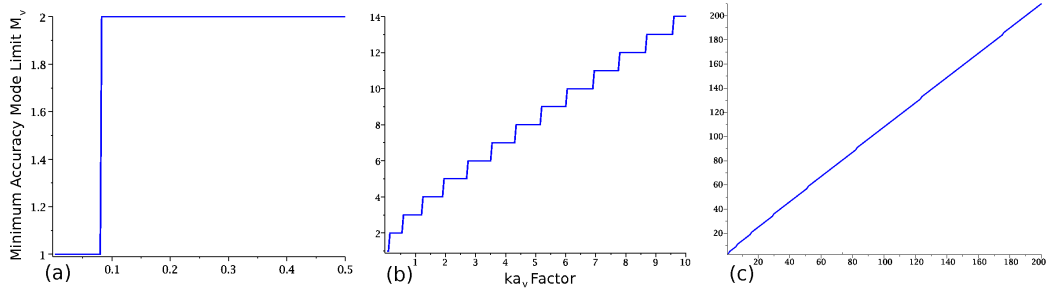


Figure 3.1: The minimal accuracy mode limits M_v are displayed for ka_v factors that are (a) small, (b) medium, and (c) large.

The coefficient factors (3.2) and (3.3) act like filters on the incident field coefficients, attenuating modes beyond a limit determined by ka_v . The filter widths of the conducting, dielectric, and lossy dielectric cylinders are very similar, even for very weak permittivity dielectrics. Since the filter widths never vary by more than one or two modes between the three cases, we can characterize the conducting cylinder case, which always has highest mode requirements, and use it for all three cases. Our lower bound limit on M_v is the first mode that causes the magnitude of the scattering coefficient to drop below 1% of its largest value. Plots of the mode limit M_v for minimal accuracy representation under these conditions are shown in Figure 3.1. Using a mode limit below this minimal accuracy representation may result in completely misrepresented fields in the multiple scattering solution. Two linear equations (3.4) were fitted to the plots (b) and (c) in Figure 3.1 so

that the minimum mode limits could be easily calculated:

$$\begin{aligned} M_v &= [1.0302ka_v + 4.5585]_{ceil} & 10 \leq ka_v \leq 200 \\ M_v &= [1.2174ka_v + 2.0578]_{ceil} & 0.5 \leq ka_v \leq 10 \end{aligned} \quad (3.4)$$

For the small ka_v from (a) in Figure 3.1) a linear approximation is not appropriate so we use a discrete definition

$$M_v = \begin{cases} 2 & 0.08125 \leq ka_v \leq 0.5 \\ 1 & ka_v < 0.08125 \end{cases} \quad (3.5)$$

The extinction and scattering cross sections will also converge to a minimal accuracy representation at the minimum mode limit, and increase in accuracy as M_v is raised. Olaofe [24] calculated the extinction cross section for the scattering of a plane-wave from multiple cylinders:

$$C_{ext} = \frac{4}{k} \operatorname{Re}\left\{ \sum_{n=-\infty}^{\infty} \sum_{v=1}^N {}_v b_n \exp[-jkd_{1v} \cos(\phi_{1v})] \right\}, \quad (3.6)$$

and also outlined the calculation of the scattering cross section. However, when the cylinders are non-absorbing, the scattering cross section is equal to the extinction cross section in (3.6). Since the extinction cross section is proportional to a sum of the scattering coefficients ${}_v b_n$, it will converge as all the coefficients of significant magnitude are included in the sum. Our minimal accuracy requirements ensure that all coefficients of significant magnitude will be included.

3.3 Upper Bound Limit

The upper bound limit of M_v is due to matrix conditioning. As we increase M_v , the condition number of our multiple scattering matrix increases. A large condition number indicates that the matrix is unstable and may produce

erroneous results when an attempt is made to invert it. The matrix condition number is obtained from a singular value decomposition by taking the ratio of the largest singular value divided by the smallest. There tends to be a threshold after which the condition number begins to increase drastically for every increase in the mode limit M_v . Using a mode limit beyond the threshold will increase the risk of errors in the matrix inversion. Therefore, we will define our upper-bound limit of M_v to be the threshold where the scattering matrix condition numbers begin to increase exponentially.

Aside from the mode limit, the condition number is affected by the background wavenumber k , the cylinder radii a_v , the separation between cylinders d , and the permittivities of the cylinders ϵ_v . These parameters define the rigid structure created by the multiple cylinders, but there is no restriction on the rotational orientation of the structure. The condition number will also be completely independent of the incident field, because the scattering matrix that we invert is independent of the incident field.

3.4 Scattering Simulations

The multiple scattering scenarios of Figure 3.2 and Figure 3.3 were each simulated for separation distances $d = 1.1\lambda$ and $d = 2.2\lambda$. Each simulation consisted of calculating the condition number of the scattering matrix for a given mode limit M_v . All the mode limits from 1 to 20 were simulated. As we would expect, the condition numbers for the broadside and inline cases were identical to machine precision because they both involve scattering from the same rigid structure of cylinders. Remember that the condition numbers are independent of rotations and incident fields. Hence, only one graph of results, Figure 3.4, is necessary for both the broadside and inline cases.

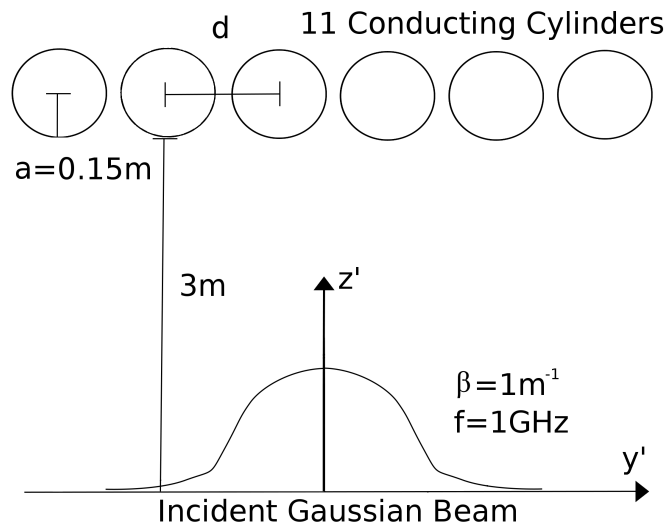


Figure 3.2: Multiple scattering of a Gaussian beam from 11 perfectly conducting cylinders with broadside incidence.

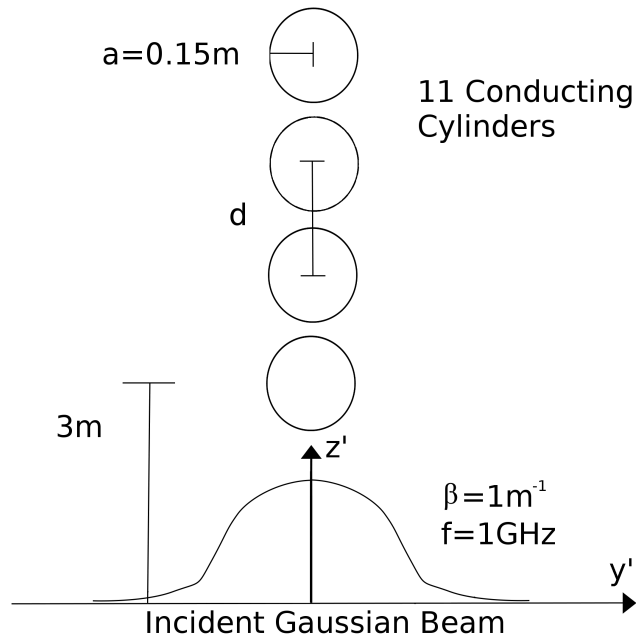


Figure 3.3: Multiple scattering of a Gaussian beam from 11 perfectly conducting cylinders with in-line incidence.

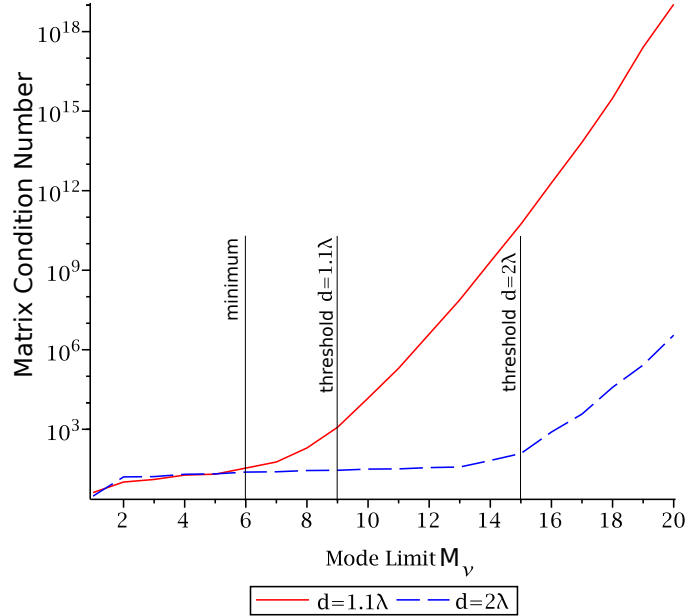


Figure 3.4: Matrix condition number compared to the mode limit. The results are identical for broadside and in-line incidence.

Since $ka_v \approx 3.14$ in both scenarios, we can use (3.4) to calculate our minimum mode limit $M_v = 6$. For the case when $d = 2\lambda$, the condition number threshold is near $M_v = 15$, well above the minimal accuracy requirement. For the case when $d = 1.1\lambda$, the coupling between cylinders is much stronger. The threshold is now $M_v = 9$, which is very close to our minimum mode limit. It will be harder to model the $d = 1.1\lambda$ case because the lower- and upper-bound limits on M_v are closer together, limiting the accuracy of the solution. In general, as cylinders are placed closer together, the threshold will decrease, making it harder to obtain higher accuracy results.

The case of multiple scattering from cylinders of various radii brings a new aspect into our analysis. Each cylinder involved in the scattering should have a mode limit M_v that matches its ka_v factor and the desired level of accuracy. Suppose we have a multiple scattering situation in which there is a large cylinder with $ka_1 = 12$ and a small cylinder with $ka_2 = 3$. Using

(3.4) to calculate the minimal accuracy mode limits, we get $M_1 = 17$ for the large cylinder and $M_2 = 6$ for the small cylinder. Now, if we impose the limit $M = 17$ for both cylinders, the small cylinder may have an excess number of modes and cause the scattering matrix to become ill-conditioned. If instead we impose $M = 6$ on both cylinders, the large cylinder's scattered field will not have enough cylindrical wave modes to be properly represented and erroneous results will ensue. By using separate mode limits, for example $M_1 = 20$ and $M_2 = 8$, we can accurately represent the multiple scattering while maintaining a properly conditioned scattering matrix.

3.5 Conclusion

In conclusion, the cylindrical mode limit M_v should be chosen carefully, considering the minimal accuracy requirements and the conditioning of the multiple scattering matrix. The highest degree of accuracy can be obtained by pushing the mode limits M_v , for each cylinder, above their minimal accuracy requirements until the scattering-matrix condition number reaches its threshold.

Chapter 4

Scattering from Cylinders Using the Two-Dimensional Vector Plane-Wave Spectrum

4.1 Introduction

Two-dimensional multiple scattering from infinite circular cylinders was first considered by Twersky in 1952 [22]. Twersky considered the scattering of a plane-wave by an arbitrary number of cylinders, first using an iterative solution and later developing a matrix inversion solution with Burke and Censor [23]. In 1970, Olaofe broke down the scattering problem into an infinite set of linear equations, which also could be solved iteratively or by matrix inversion [24, 25]. The effectiveness of the matrix inversion method was emphasized by the experimental results of Young and Bertrand [26] and the analysis of Elsherbeni [27]. We will use the matrix inversion solution and apply it to T-matrix formalism which directly relates the incident field coefficients to the multiple scattering coefficients [84].

Aside from plane-wave incidence, Gaussian beam incidence and arbitrary beam incidence have also been considered. The scattering of two-dimensional Gaussian beams by two cylinders was considered by Kojima et al. [31], and Sugiyama and Kozaki [32]. This was extended to include an arbitrary number of cylinders by Yokota et al. [33] and Elsherbeni et al. [34]. Gouesbet [72] considered arbitrary beam incidence under generalized Lorentz-Mie theory (GLMT). He allowed for any arbitrary, three-dimensional, incident field by

using the theory of distributions. We are considering a novel application of the two-dimensional vector plane-wave spectrum (VPWS) to produce an arbitrary incident field in the multiple scattering from cylinders.

The VPWS breaks down an arbitrary aperture distribution into an infinite sum of plane-waves which are the eigenfunctions of the homogeneous, isotropic wave equation in Cartesian coordinates. The VPWS can produce both homogeneous and inhomogeneous plane-waves, which represent the radiative and evanescent regions of the incident field respectively. Because of the convergence properties of evanescent fields in cylindrical coordinates, it is essential that our solution separates the two regions [85]. Our numerical simulations will focus on evanescent field incidence, since most previous authors, using a cylindrical wave approach, only considered radiative incidence [24–27,31–34]. Exceptions to this include Yang et al. [35], who included evanescent components of a Gaussian beam in their multiple scattering solution, and Chapter 2, where the scattering of the evanescent components of a Gaussian beam from a single cylinder was presented. The Gaussian beam’s evanescent field is well defined, whereas our VPWS formulation allows for arbitrary evanescent fields.

Evanescent fields are composed of inhomogeneous plane-waves, in which the equi-amplitude and equi-phase surfaces do not coincide [78]. These evanescent waves are only significant in the near-field because they decay exponentially away from their source. Evanescent fields are present in the near-field of practically every scattering or radiating source because they contain all the sub-wavelength details of the electromagnetic field distribution. This phenomenon is currently exploited in apertureless near-field scanning optical microscopy (ANSOM), where a small metallic probe is used to scatter an object’s evanescent field into radiation in order to obtain super-resolution images [64]. Arrays of probes, gratings and larger near-field diffractive elements have also been proposed for scattering evanescent fields [86]. Sub-wavelength resolution in microwave source localization has been investigated using sin-

gle and multiple scatterers [38]. An investigation by Gulayev et al. [87] demonstrated the scattering of incident evanescent fields from a periodic grating. They defined two methods for recovering evanescent field data from the scattering: distant-spatial and interference-spatial spectroscopy. Numerical examples presented herein focus on the conversion of evanescent fields into radiating waves through near-field scattering from a similar grating to Gulayev et al. [87]. By using sub-wavelength cylinders and half-wavelength spacing in the grating, we are able to convert evanescent fields into beams of radiation with directionality based on the incident evanescent field's spatial frequency.

By writing generalized equations for the incident, scattered and transmitted waves, and solving the boundary conditions on each cylinder simultaneously, we can obtain a T-matrix solution for the multiple scattering from cylinders. We extend our formulation of the solution to include any arbitrary combination of conducting and dielectric cylinders with various radii. The geometry and coordinate systems are displayed in Fig. 4.1.

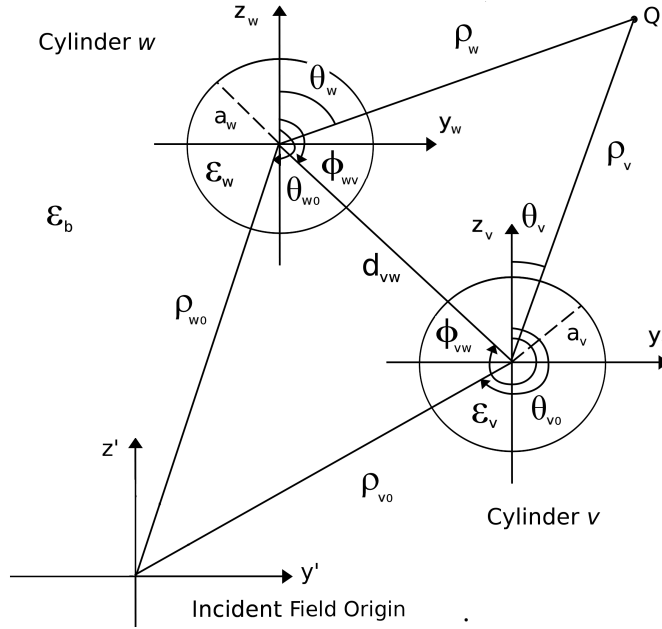


Figure 4.1: Geometry and coordinate systems for the cylinders and the incident field. The x direction is perpendicular to the page.

4.2 Incident Electric Fields

Use of the VPWS technique allows us to create an incident electric field with arbitrary distribution and polarization. Here we have derived the two-dimensional VPWS from the three-dimensional version provided by Guo et al. [88]. The VPWS breaks down the electromagnetic field across an aperture into a sum of homogeneous and inhomogeneous plane-waves, while properly maintaining the polarization of the field. Thus, the VPWS always satisfies Maxwell's equations. For cylindrical scattering, the transverse magnetic (TM) polarization has the magnetic field transverse to the cylinder axes and the transverse electric (TE) polarization has the electric field transverse to the cylinder axes.

For an electromagnetic wave in cylindrical coordinates there are six components to the vector fields E_x , E_ρ , E_θ , H_x , H_ρ , and H_θ . However, since any

polarization state can be described by a combination of TM and TE modes, all the field information can be contained within E_x and H_x . The other components can be computed from E_x and H_x using Maxwell's equations with no charges or currents:

$$\nabla \times \mathbf{E} = -\frac{\partial \mathbf{B}}{\partial t} \quad (4.1)$$

$$\nabla \times \mathbf{H} = \frac{\partial \mathbf{D}}{\partial t} \quad (4.2)$$

To simplify the number of equations, only the E_x and H_x components will be shown.

The two-dimensional VPWS in Cartesian coordinates centred about the coordinate system (z', y', x) can be represented by

$$E_x^i(z', y') = \frac{1}{2\pi} \int_{-\infty}^{\infty} \tilde{E}_{TM}(k_y) \exp[-j(k_y y' + k_z z')] dk_y, \quad (4.3)$$

$$H_x^i(z', y') = \frac{1}{2\pi} \int_{-\infty}^{\infty} \tilde{H}_{TE}(k_y) \exp[-j(k_y y' + k_z z')] dk_y, \quad (4.4)$$

$$\tilde{E}_{TM}(k_y) = \int_{-\infty}^{\infty} E_x^i(0, y') \exp(jk_y y') dy', \quad (4.5)$$

$$\tilde{H}_{TE}(k_y) = \int_{-\infty}^{\infty} H_x^i(0, y') \exp(jk_y y') dy'. \quad (4.6)$$

The fields are defined from the initial aperture distribution along the plane $z' = 0$. Because of uniformity in the x direction, we have $k_x = 0$, so that $k^2 = k_y^2 + k_z^2$. The time dependence $\exp(j\omega t)$ is assumed and suppressed throughout.

The two Fourier transforms, (4.5) and (4.6), represent the spatial frequency content across the aperture for the \hat{x} components of the electric and magnetic fields respectively. When the spatial frequency k_y exceeds the wavenumber k , the \hat{z} component becomes imaginary $k_z = -j\sqrt{k_y^2 - k^2}$ for

$z' \geq 0$. These waves are called evanescent because they decay exponentially in the \hat{z}' direction.

It is expedient to use the fast Fourier transform (FFT) in (4.5) and (4.6) when the distributions $E_x^i(0, y')$ and $H_x^i(0, y')$ are discretized or when the integral cannot be evaluated analytically.

Now we will convert from Cartesian coordinates (z', y', x) to polar coordinates (ρ_v, θ_v, x) centred about each cylinder v :

$$y' = \rho_v \sin(\theta_v) - \rho_{v0} \sin(\theta_{v0}), \quad (4.7)$$

$$z' = \rho_v \cos(\theta_v) - \rho_{v0} \cos(\theta_{v0}). \quad (4.8)$$

The unit vectors $\hat{\rho}_v$ and $\hat{\theta}_v$ are unique for the coordinates of each cylinder v . We will also convert our variable of integration into an angular representation:

$$k_y = k \sin(\phi). \quad (4.9)$$

Applying these transformations to equations (4.3) and (4.4) yields

$$E_x^i(\rho_v, \theta_v) = \frac{k}{2\pi} \int_{-\pi/2-j\infty}^{\pi/2+j\infty} \tilde{E}_{TM}[k \sin(\phi)] \cos(\phi) \exp[-jk\rho_v \cos(\theta_v - \phi) + jk\rho_{v0} \cos(\theta_{v0} - \phi)] d\phi, \quad (4.10)$$

$$H_x^i(\rho_v, \theta_v) = \frac{k}{2\pi} \int_{-\pi/2-j\infty}^{\pi/2+j\infty} \tilde{H}_{TE}[k \sin(\phi)] \cos(\phi) \exp[-jk\rho_v \cos(\theta_v - \phi) + jk\rho_{v0} \cos(\theta_{v0} - \phi)] d\phi. \quad (4.11)$$

Now we manipulate and simplify equations (4.10) and (4.11) using the Bessel

function identity [81]:

$$\exp[-jk\rho_v \cos(\theta_v - \phi)] = \sum_{n=-\infty}^{\infty} j^{-n} \exp[jn(\theta_v - \phi)] J_n(k\rho_v). \quad (4.12)$$

Finally, we can write our incident electromagnetic fields as sums of TM (4.13) and TE (4.14) cylindrical waves with coefficients (4.15) and (4.16) respectively,

$$E_x^i = \sum_{n=-\infty}^{\infty} j^{-n} \exp(jn\theta_v) J_n(k\rho_v) {}_vA_n, \quad (4.13)$$

$$H_x^i = \sum_{n=-\infty}^{\infty} j^{-n} \exp(jn\theta_v) J_n(k\rho_v) {}_vQ_n, \quad (4.14)$$

$${}_vA_n = \frac{k}{2\pi} \int_{-\pi/2-j\infty}^{\pi/2+j\infty} \tilde{E}_{TM}[k \sin(\phi)] \exp[jk\rho_{v0} \cos(\theta_{v0} - \phi) - jn\phi] \cos(\phi) d\phi. \quad (4.15)$$

$${}_vQ_n = \frac{k}{2\pi} \int_{-\pi/2-j\infty}^{\pi/2+j\infty} \tilde{H}_{TE}[k \sin(\phi)] \exp[jk\rho_{v0} \cos(\theta_{v0} - \phi) - jn\phi] \cos(\phi) d\phi. \quad (4.16)$$

The coefficients (4.15) and (4.16) contain both the radiative and evanescent components of the incident field. From these representations, the evanescent components will only be valid in the half-space $z' \geq 0$ because when $z' < 0$, the exponential decay of the evanescent fields will switch to exponential growth. In Chapter 2 it was demonstrated that in representing evanescent fields from a planar source as a sum of cylindrical wave modes [(4.13) or (4.14)], the fields converge spatially outward as more modes n are included. This will make the entire incident field extremely difficult to represent in the far-field. To overcome this, we split the coefficients into separate radiative and evanescent components. The evanescent components only need to be calculated for near-field scattering, and they can be ignored in the far-field.

4.2.1 Incident Radiated Fields

The incident radiated fields can be isolated by limiting the range of integration in the coefficients (4.15) and (4.16) to $-\pi/2 \leq \phi \leq \pi/2$. In this region, the plane-waves are homogeneous and propagate energy outward from the source. In contrast to evanescent fields, the radiative components will be valid for all z' and converge quickly in the far-field. In general, the integration will have no analytical solution so that numerical integration will be necessary. If (4.5) and (4.6) were computed using the FFT, then the integrals in (4.15) and (4.16) should be discretized accordingly.

4.2.2 Incident Evanescent Fields

The incident evanescent fields can be isolated by limiting the range of integration in the coefficients (4.15) and (4.16) to the complex regions where $|\sin(\phi)| > 1$. In order to combine the two halves of this region into one integral, we use the following transformations on the negative and positive halves of the integration range respectively:

$$\phi = -\pi/2 - ju, \quad (4.17)$$

$$\phi = \pi/2 + ju, \quad (4.18)$$

to obtain

$${}_v A_n^{evan} = \frac{k}{2\pi} \int_0^\infty \sinh(u) \{ {}_v S_n^+ \tilde{E}_{TM}[k \cosh(u)] + {}_v S_n^- \tilde{E}_{TM}[-k \cosh(u)] \} du, \quad (4.19)$$

$${}_v Q_n^{evan} = \frac{k}{2\pi} \int_0^\infty \sinh(u) \{ {}_v S_n^+ \tilde{H}_{TE}[k \cosh(u)] + {}_v S_n^- \tilde{H}_{TE}[-k \cosh(u)] \} du, \quad (4.20)$$

$${}_v S_n^\pm = j^{\mp n} \exp[\pm nu \pm jk\rho_{v0} \sin(\theta_{v0} \mp ju)]. \quad (4.21)$$

Again, the integrals in (4.19) and (4.20) need to be numerically integrated, or discretized appropriately if the FFT has been previously used to compute \tilde{E}_{TM} and \tilde{H}_{TE} .

4.3 Scattered Fields

The scattered electric and magnetic field components can all be derived from the E_x and H_x components alone. The scattered fields will be represented as a sum of cylindrical waves with coefficients ${}_v b_n$ and ${}_v g_n$, representing the TM and TE modes respectively. For a time dependence $\exp(j\omega t)$ we use Hankel functions of the second kind $H_n^{(2)}(k\rho_v)$ to represent outgoing waves:

$$E_x^{sv} = \sum_{n=-\infty}^{\infty} j^{-n} \exp(jn\theta_v) H_n^{(2)}(k\rho_v) {}_v b_n, \quad (4.22)$$

$$H_x^{sv} = \sum_{n=-\infty}^{\infty} j^{-n} \exp(jn\theta_v) H_n^{(2)}(k\rho_v) {}_v g_n. \quad (4.23)$$

We also need to represent the scattered field from each cylinder in the coordinate system of all the other cylinders. To do this we will apply the Graf addition theorem [89]:

$$Z_v(z) \exp(jv\psi) = \sum_{m=-\infty}^{\infty} Z_{v+m}(x) J_m(y) \exp(jm\delta), \quad (4.24)$$

the coordinates of which are displayed in Fig. 4.2. When Z is a Bessel function of the second or third kind, we have the restriction

$$|\exp(\pm j\delta)y| < |x|. \quad (4.25)$$

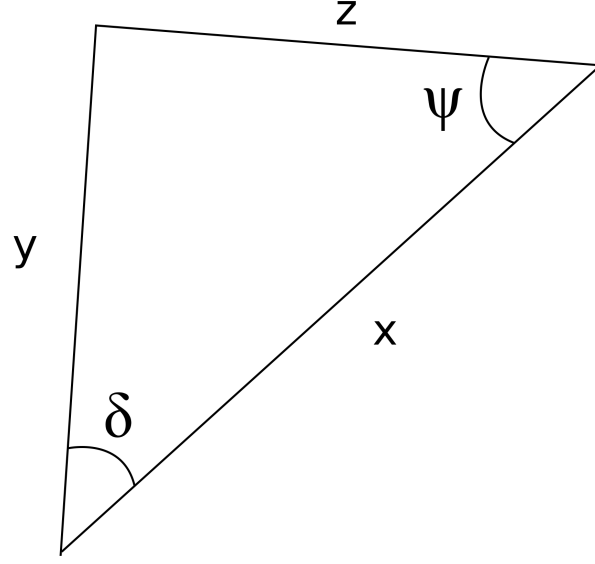


Figure 4.2: Triangle showing the coordinates of transformation in the Graf addition theorem (4.24)

By applying the Graf addition theorem (4.24) to our geometry in Fig. 4.1, we obtain

$$H_n^{(2)}(k\rho_w) \exp(jn\theta_w) = \sum_{m=-\infty}^{\infty} H_{n-m}^{(2)}(kd_{wv}) J_m(k\rho_v) \exp[j(n-m)\phi_{wv} + jm\theta_v]. \quad (4.26)$$

Now we apply the results (4.26) to our scattered fields from (4.22) and (4.23):

$$E_x^{sw} = \sum_{n=-\infty}^{\infty} j^{-n} \exp(jn\theta_v) J_n(k\rho_v)_{wv} B_n, \quad (4.27)$$

$${}_{wv}B_n = \sum_{m=-\infty}^{\infty} j^{n-m} \exp[j(m-n)\phi_{wv}] H_{m-n}^{(2)}(kd_{wv})_w b_m, \quad (4.28)$$

$$H_x^{sw} = \sum_{n=-\infty}^{\infty} j^{-n} \exp(jn\theta_v) J_n(k\rho_v)_{wv} G_n, \quad (4.29)$$

$${}_{wv}G_n = \sum_{m=-\infty}^{\infty} j^{n-m} \exp[j(m-n)\phi_{wv}] H_{m-n}^{(2)}(kd_{wv}) {}_w g_m. \quad (4.30)$$

The coefficients ${}_{wv}B_n$ and ${}_{wv}G_n$ are the coupling coefficients for the TM and TE polarizations respectively. They translate the scattered field from cylinder w to an incident field on cylinder v .

4.4 Transmitted Fields

Since we want to consider the solution for perfect conducting and dielectric cylinders, we will need two definitions for the transmitted fields. The perfect electric conductor (PEC) and perfect magnetic conductor (PMC) will both have electric and magnetic fields equal to zero inside the cylinders. The dielectric case defines the transmitted electric and magnetic fields as

$$E_x^{tv} = \sum_{n=-\infty}^{\infty} j^{-n} \exp(jn\theta_v) J_n(\sqrt{\epsilon_{rv}}k\rho_v) {}_v d_n, \quad (4.31)$$

$$H_x^{tv} = \sum_{n=-\infty}^{\infty} j^{-n} \exp(jn\theta_v) J_n(\sqrt{\epsilon_{rv}}k\rho_v) {}_v h_n. \quad (4.32)$$

The relative permittivity is the ratio of cylinder permittivity to background permittivity $\epsilon_{rv} = \epsilon_v/\epsilon_b$, and $k = \omega\sqrt{\epsilon_b\mu_b}$ is the background wavenumber. The transmission coefficients for TM and TE scattering are ${}_v d_n$ and ${}_v h_n$ respectively, and can be found by applying the boundary conditions.

4.5 Boundary Conditions

For a dielectric cylinder, the tangential electric and magnetic field components must be continuous across the boundary of the cylinders. Therefore, we equate the corresponding \hat{x} and $\hat{\theta}$ components of the electric and magnetic

fields at the cylinder boundaries $\rho_v = a_v$:

$$E_x^{tv}(a_v, \theta_v) = E_x^i(a_v, \theta_v) + E_x^{sv}(a_v, \theta_v) + \sum_{w \neq v} E_x^{sw}(a_v, \theta_v), \quad (4.33)$$

$$H_\theta^{tv}(a_v, \theta_v) = H_\theta^i(a_v, \theta_v) + H_\theta^{sv}(a_v, \theta_v) + \sum_{w \neq v} H_\theta^{sw}(a_v, \theta_v), \quad (4.34)$$

$$E_\theta^{tv}(a_v, \theta_v) = E_\theta^i(a_v, \theta_v) + E_\theta^{sv}(a_v, \theta_v) + \sum_{w \neq v} E_\theta^{sw}(a_v, \theta_v), \quad (4.35)$$

$$H_x^{tv}(a_v, \theta_v) = H_x^i(a_v, \theta_v) + H_x^{sv}(a_v, \theta_v) + \sum_{w \neq v} H_x^{sw}(a_v, \theta_v). \quad (4.36)$$

For a PEC cylinder, the tangential electric fields must vanish at the boundary

$$0 = E_x^i(a_v, \theta_v) + E_x^{sv}(a_v, \theta_v) + \sum_{w \neq v} E_x^{sw}(a_v, \theta_v), \quad (4.37)$$

$$0 = E_\theta^i(a_v, \theta_v) + E_\theta^{sv}(a_v, \theta_v) + \sum_{w \neq v} E_\theta^{sw}(a_v, \theta_v). \quad (4.38)$$

The magnetic fields for a PEC cylinder do not vanish at the boundary but are not necessary to consider when solving for the scattering coefficients. For a PMC cylinder, the tangential magnetic fields must vanish at the boundary

$$0 = H_\theta^i(a_v, \theta_v) + H_\theta^{sv}(a_v, \theta_v) + \sum_{w \neq v} H_\theta^{sw}(a_v, \theta_v), \quad (4.39)$$

$$0 = H_x^i(a_v, \theta_v) + H_x^{sv}(a_v, \theta_v) + \sum_{w \neq v} H_x^{sw}(a_v, \theta_v). \quad (4.40)$$

The electric fields for a PMC cylinder do not vanish at the boundary but are not necessary to consider when solving for the scattering coefficients [90].

The magnetic and electric $\hat{\theta}$ components can be calculated from the electric and magnetic \hat{x} components by using (4.1) and (4.2), respectively. In

the two-dimensional scattering case there is no cross-polarization between the TM and TE polarizations. Therefore, the solution is found by using E_x and H_θ to solve for the TM scattering coefficients, and by using E_θ and H_x to solve for the TE scattering coefficients:

$${}_v b_n = {}_v f_n {}_v A_n + {}_v f_n \sum_{w \neq v} {}_w v B_n, \quad (4.41)$$

$${}_v g_n = {}_v f_n {}_v Q_n + {}_v f_n \sum_{w \neq v} {}_w v G_n. \quad (4.42)$$

The TM solution (4.41) and TE solution (4.42) share the same functional form, the only differences are in the single scattering coefficients ${}_v f_n$. For a dielectric cylinder with TM polarization, we have

$${}_v f_n = \frac{J_n'(ka_v) J_n(\sqrt{\epsilon_{rv}} ka_v) - \sqrt{\epsilon_{rv}} J_n(ka_v) J_n'(\sqrt{\epsilon_{rv}} ka_v)}{\sqrt{\epsilon_{rv}} H_n^{(2)}(ka_v) J_n'(\sqrt{\epsilon_{rv}} ka_v) - H_n^{(2)'}(ka_v) J_n(\sqrt{\epsilon_{rv}} ka_v)}, \quad (4.43)$$

and with TE polarization it becomes

$${}_v f_n = \frac{\sqrt{\epsilon_{rv}} J_n'(ka_v) J_n(\sqrt{\epsilon_{rv}} ka_v) - J_n(ka_v) J_n'(\sqrt{\epsilon_{rv}} ka_v)}{H_n^{(2)}(ka_v) J_n'(\sqrt{\epsilon_{rv}} ka_v) - \sqrt{\epsilon_{rv}} H_n^{(2)'}(ka_v) J_n(\sqrt{\epsilon_{rv}} ka_v)}. \quad (4.44)$$

For a PEC cylinder with TM polarization, we have

$${}_v f_n = -\frac{J_n(ka_v)}{H_n^{(2)}(ka_v)}, \quad (4.45)$$

and with TE polarization it becomes

$${}_v f_n = -\frac{J_n'(ka_v)}{H_n^{(2)'}(ka_v)}. \quad (4.46)$$

For a PMC cylinder with TM polarization, we have

$${}_v f_n = -\frac{J_n'(ka_v)}{H_n^{(2)'}(ka_v)}, \quad (4.47)$$

and with TE polarization it becomes

$${}_v f_n = -\frac{J_n(ka_v)}{H_n^{(2)}(ka_v)}. \quad (4.48)$$

The PMC cylinder single scattering coefficients 4.47 and 4.48 are identical to the PEC case with the opposite polarization. 4.46 and 4.45 respectively. The scattering from a perfect electromagnetic conductor cylinder, as a generalization of the PEC and PMC cylinders, was provided by Ruppin [91].

The prime indicates a derivative of the function with respect to the whole argument. The subscript v indicates that the multiple scattering solution may contain cylinders with different radii and different complex permittivities. In terms of the scattering solution, the properties of each cylinder are completely confined to the single scattering coefficients ${}_v f_n$.

4.6 T-Matrix Formulation

The T-matrix formalism, which is commonly used in spherical scattering [84], represents the multiple scattering coefficients \mathbf{L} [(4.49) and (4.50)] by a matrix \mathbf{T} , which multiplies the incident field coefficients \mathbf{P} [(4.51) and (4.52)]. In this case, because the TM and TE modes do not interact, we compute their scattering separately using (4.53) and (4.54), respectively. The matrix \mathbf{T} depends upon the polarization, the cylinder properties, and the location of the cylinders. The total number of cylinders is M .

The number of cylindrical wave modes needs to be truncated to some maximum magnitude N_v , which can be unique for each cylinder. The choice of an appropriate mode limit N_v depends mostly on the value of the factor

ka_v . It is important to note that setting the mode limit too high may cause the matrix inversion in (4.59) to become ill-conditioned. A complete analysis of choosing mode limits N_v in two-dimensional multiple scattering was provided in Chapter 3.

$$\mathbf{L}_{TM} = [{}_1b_{-N_1}, \dots, {}_1b_{N_1}, {}_2b_{-N_2}, \dots]^T, \quad (4.49)$$

$$\mathbf{L}_{TE} = [{}_1g_{-N_1}, \dots, {}_1g_{N_1}, {}_2g_{-N_2}, \dots]^T, \quad (4.50)$$

$$\mathbf{P}_{TM} = [{}_1A_{-N_1}, \dots, {}_1A_{N_1}, {}_2A_{-N_2}, \dots]^T, \quad (4.51)$$

$$\mathbf{P}_{TE} = [{}_1Q_{-N_1}, \dots, {}_1Q_{N_1}, {}_2Q_{-N_2}, \dots]^T, \quad (4.52)$$

$$\mathbf{L}_{TM} = \mathbf{T}_{TM}\mathbf{P}_{TM}, \quad (4.53)$$

$$\mathbf{L}_{TE} = \mathbf{T}_{TE}\mathbf{P}_{TE}. \quad (4.54)$$

Our \mathbf{T} matrix for the TM and TE polarizations is similar, except for the single scattering coefficients, so we can derive it from (4.41) or (4.42). Both equations define an infinite set of linear equations which can be truncated and solved by matrix inversion. We can rewrite (4.41) or (4.42) in matrix form as

$$\mathbf{L} = \mathbf{F}\mathbf{P} + \mathbf{FCL}, \quad (4.55)$$

using the appropriate form of \mathbf{L} , \mathbf{P} , and \mathbf{F} for the TM and TE modes. The diagonal matrix \mathbf{F} contains the single scattering coefficients:

$$\mathbf{F} = \text{diag}[{}_1f_{-N_1}, \dots, {}_1f_{N_1}, {}_2f_{-N_2}, \dots]. \quad (4.56)$$

The matrix \mathbf{C} is defined by the second term on the right side of (4.41) or (4.42), and the definition of the coupling coefficients (4.28) or (4.30):

$$\mathbf{C} = \begin{bmatrix} \mathbf{0} & \mathbf{C}_{12} & \dots & \mathbf{C}_{1M} \\ \mathbf{C}_{21} & \mathbf{0} & \dots & \mathbf{C}_{2M} \\ \vdots & \vdots & \ddots & \vdots \\ \mathbf{C}_{M1} & \mathbf{C}_{M2} & \dots & \mathbf{0} \end{bmatrix}. \quad (4.57)$$

The sub-matrices \mathbf{C}_{vw} relate the scattered field of cylinder w to the scattering coefficients of cylinder v . The elements $c_{n,m}$ of the sub-matrices \mathbf{C}_{vw} come directly from the coupling coefficients, (4.28) and (4.30), and are given by

$$c_{n,m} = j^{n-m} H_{m-n}^{(2)}(kd_{wv}) \exp[j(m-n)\phi_{wv}]. \quad (4.58)$$

The Bessel modes n index the rows of the sub-matrices, while the Bessel modes m index the columns. The mode limits N_v might not be the same for n and m , so that \mathbf{C}_{vw} may not be square. However, the total matrix \mathbf{C} will still be square.

The solution to (4.55) is found through matrix inversion

$$\mathbf{L} = (\mathbf{F}^{-1} - \mathbf{C})^{-1} \mathbf{P} = \mathbf{T} \mathbf{P}. \quad (4.59)$$

Our \mathbf{T} matrix is given by $(\mathbf{F}^{-1} - \mathbf{C})^{-1}$. A great advantage of this form of solution (4.59) is the separability of the aspects involved in the scattering. The properties of each cylinder are contained as separate elements in the \mathbf{F} matrix, which represents the solution of the single scattering problem $\mathbf{L} = \mathbf{F} \mathbf{P}$. The location of each cylinder relative to the others is accounted for by the matrix \mathbf{C} , which allows for multiple scattering interactions. Therefore, our matrix \mathbf{T} is independent of the form of the incident field except for its polarization. \mathbf{T} acts as a matrix operator that takes, as input, the incident field coefficients and produces, as output, the scattered field coefficients.

4.7 Numerical Simulations

Our simulations will focus on evanescent field scattering which has mostly been considered using other methods [38, 86, 87]. Most previous authors who considered cylindrical scattering using a cylindrical wave method only considered radiative incidence [24–27, 31–34]. We will consider the effects of evanescent fields scattering from a grating of sub-wavelength cylinders, as shown in Fig. 4.3. The incident fields have a frequency of $f = 1GHz$ and are separated from the cylinders by $\lambda/4$ in all cases. The incident fields are TM polarized with the electric fields oriented in the \hat{x} direction. The cylinders are spaced $d = \lambda/2$ apart, inside a vacuum. They are all perfectly conducting cylinders of radii $a = 0.005m$. The distance from the incident field to the cylinders is critical when scattering evanescent fields because the decay rate of an evanescent wave depends upon its spatial frequency. Aside from this, evanescent fields from an infinite planar source do not diverge, so that the shape of the field is preserved in the \hat{z}' direction.

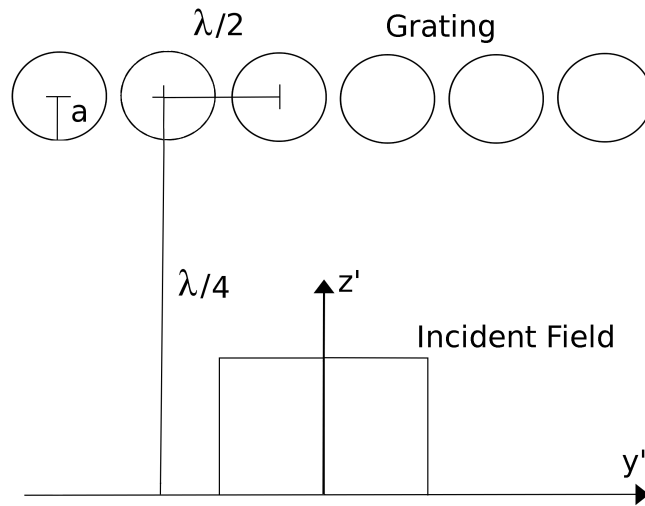


Figure 4.3: Setup for the numerical simulations. The grating is made up of 41 conducting cylinders with $a = 0.005m$. The dimensions are not drawn to scale.

In order to characterize the fundamental effects of the grating on evanescent fields, we scattered four evanescent fields composed of single spatial frequencies ranging from $1.1k$ to $2k$ from the grating. Results are shown for the frequencies which travel in the direction of increasing y' ; equivalent frequencies travelling in the opposite direction are identical except that they scatter into the right-half plane. The resulting far-field radiation intensity polar-plots are displayed in Figures 4.4 to 4.7, with $\theta = 0$ along the \hat{z}' axis. The far-field radiation intensity in two-dimensions was computed as

$$U = \rho \frac{|E_x|^2}{2\eta} + \rho\eta \frac{|H_x|^2}{2} W/m, \quad (4.60)$$

where $\eta = \sqrt{\mu_b/\epsilon_b}$ is the background impedance and ρ is the radial distance from the scattering centre.

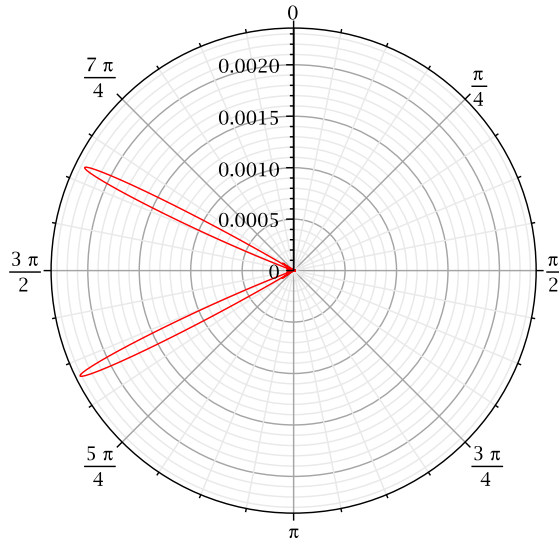


Figure 4.4: Far-field intensity (W/m) plot for scattering of the incident field, with aperture distribution $E_x^i(0, y') = \exp(-j1.1ky')$, from the grating.

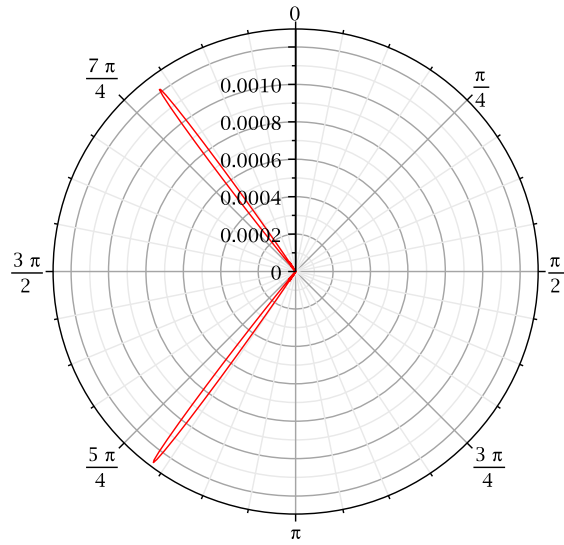


Figure 4.5: Far-field intensity (W/m) plot for scattering of the incident field, with aperture distribution $E_x^i(0, y') = \exp(-j1.4ky')$, from the grating.

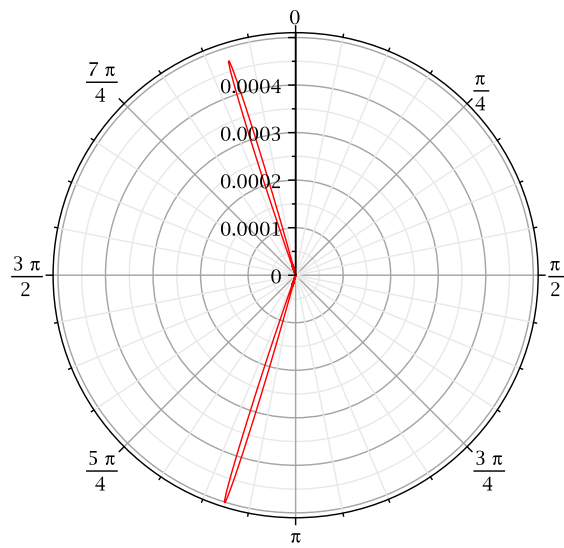


Figure 4.6: Far-field intensity (W/m) plot for scattering of the incident field, with aperture distribution $E_x^i(0, y') = \exp(-j1.7ky')$, from the grating.

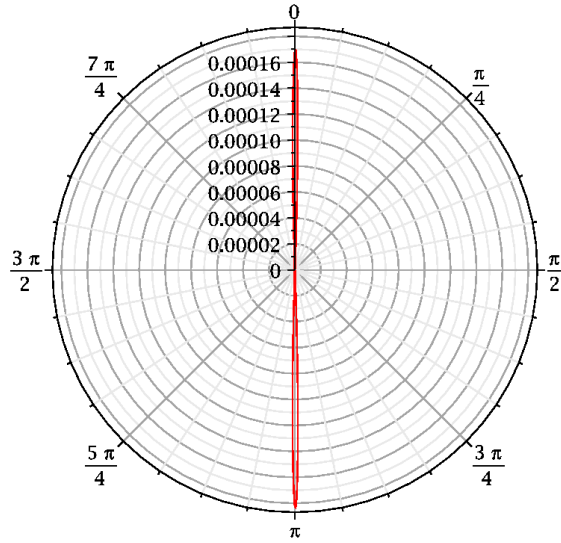


Figure 4.7: Far-field intensity (W/m) plot for scattering of the incident field, with aperture distribution $E_x^i(0, y') = \exp(-j2ky')$, from the grating.

It is clearly seen from Figures 4.4 to 4.7 that the grating scatters the incident evanescent field into two beams of radiation which travel in directions that depend on the spatial frequency of the incident evanescent field. The grating works like a phased array antenna; each cylinder scatters a small portion of the phase along the incident evanescent field. The scattered beam direction is where the scattered fields from each cylinder add constructively, and is determined by the phase variation along the grating.

Because single spatial frequencies form scattered beams with a specific directionality, an incident field with multiple spatial frequencies should form multiple scattered beams in various directions. To test the effects of multiple spatial frequency components scattering simultaneously, we have scattered the evanescent field of a square shaped beam, with an aperture distribution given by (4.61), from the grating of Figure 4.3. The results are shown in Figure 4.8 and Figure 4.9. The radiative components of the square beam are not included in this analysis. We can see several beams travelling in various

directions from the grating, each representing part of the spatial frequency content of the incident field. The spatial frequency content of the incident field from k to $2k$ is shown in Figure 4.10 and can be directly compared to the scattered far-field intensity rectangular plot of Figure 4.9. Each peak in the spatial frequency content corresponds to a scattered beam in the far-field. The scattered beams from higher spatial frequencies are more attenuated because they decay faster from the incident field origin. Incident spatial frequencies near $2k$ and $-2k$ both scatter power near $\theta = 0$, resulting in the slight amplitude increase there. The components beyond $2k$ only have a small scattering effect because they decay extremely fast in the \hat{z}' direction.

$$E_x^i(0, y') = \begin{cases} 1 & |y'| \leq 1 \\ 0 & |y'| > 1 \end{cases} \quad (4.61)$$

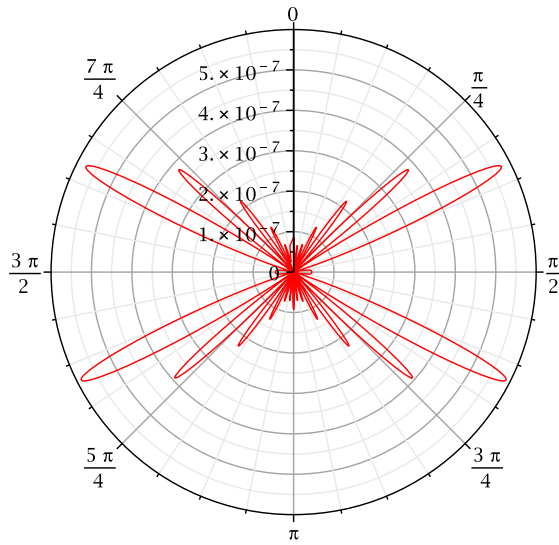


Figure 4.8: Far-field intensity (W/m) polar plot for scattering of the evanescent field of a square shaped beam.

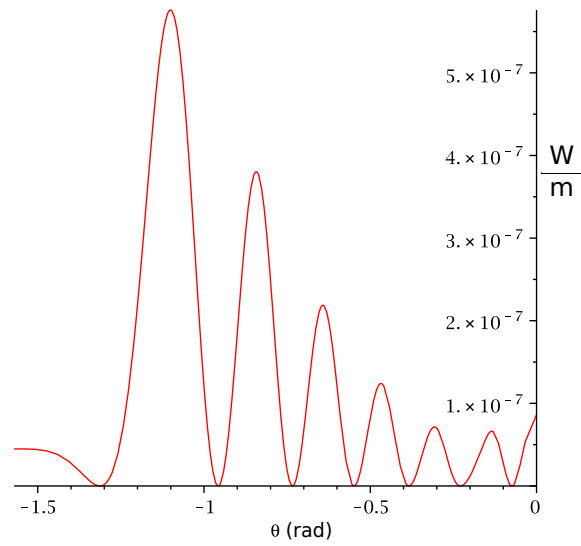


Figure 4.9: Far-field intensity (W/m) plot for scattering of the evanescent field of a square beam for $-\pi/2 \leq \theta \leq 0$.

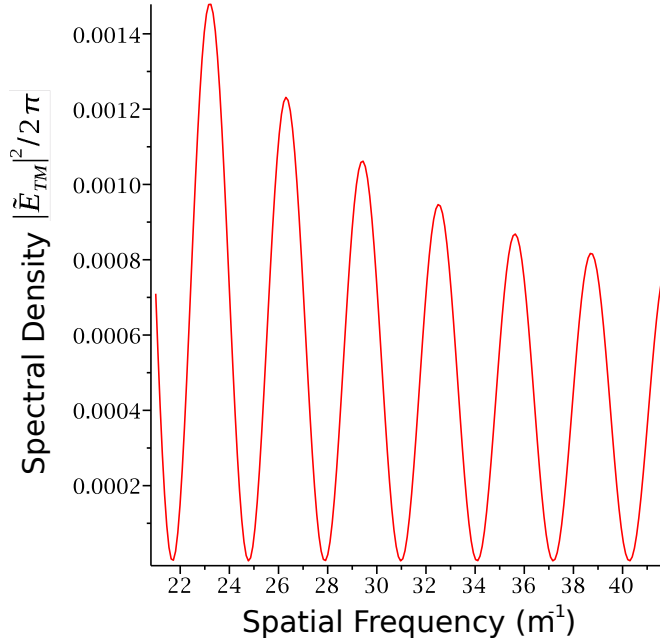


Figure 4.10: Absolute value of the spatial frequency content of the incident evanescent field from k to $2k$

4.8 Conclusion

The VPWS was applied to the multiple scattering from infinite circular cylinders in order to obtain a solution in terms of T-matrix formalism, which represents the multiple scattering coefficients as a matrix operation on the incident field coefficients. The VPWS allowed us to define our incident field with arbitrary radiative and evanescent components.

Numerical simulations were performed by imposing incident evanescent waves upon a grating of cylinders. It was demonstrated that the grating could transform the evanescent field into a set of propagating beams. Each propagating beam had a direction that corresponded to a spatial frequency component of the incident evanescent field. Such a grating could be used to analyze the spatial frequency content of evanescent fields.

Chapter 5

Scattering from Cylinders Near a Dielectric Half-Space Using a General Method of Images

5.1 Introduction

Solutions to the scattering of electromagnetic waves from multiple dielectric and conducting cylinders have been investigated by many authors [8, 24, 25, 28, 29, 34, 35, 92]. Decomposing the electromagnetic fields into cylindrical waves enables the boundary conditions to be solved directly, leading to an analytic solution of the scattering problem. The inclusion of a dielectric half-space in the multiple scattering setup complicates the solution because the boundary conditions on the planar interface cannot be applied directly using cylindrical waves. Many authors have used numerical approaches [93–95], but we will focus on cylindrical wave decomposition methods.

Borghini et al. [53, 54], Frezza et al. [52, 57], and Lee [56, 58] proposed scattering algorithms that apply the boundary conditions on the cylinders directly by equating cylindrical wave modes. The waves scattered from the cylinders are translated, via a plane-wave spectrum, to the planar interface where the plane-wave reflection coefficients are applied. The field is then translated back to the cylinders and converted back into a sum of cylindrical waves. This allows the boundary conditions to be applied around the cylinders while completely accounting for all of the multiple interactions between the cylinders and the interface. However, these methods require a significant

amount of numerical integration which can be computationally intensive.

For a perfectly conducting plane, the method of images can be applied to obtain an exact solution [43–45]. The method of images can also be applied at a vacuum-plasma interface where the reflection coefficients are not angle-dependent [52]. However, for a dielectric half-space the reflection coefficients are angle-dependent, which makes the analysis more complicated. Videen and Ngo [46] and Wang et al. [93] formulated an approximate method of images for dielectric half-spaces by assuming that the scattered fields from the cylinders strike the planar interface at normal incidence, a solution which is only accurate if the cylinders are sufficiently separated from the interface. Coatanhay and Conoir [47, 48] later produced a general method of images (GMI) approach where the reflection coefficients of the interface are converted into a cylindrical form using a Fourier series. Their GMI accounts for the angular dependence of the reflection coefficients, while avoiding the need for numerical integration. The only shortfall of this technique is that the Fourier series can only account for a limited range of evanescent field interactions between the cylinders and the interface.

Our formulation applies a GMI to vector electromagnetic scattering, including multiple cylinders and arbitrary beam incidence. By deriving the Fourier series method from the well-known plane-wave integral method, we are able to draw parallels between the two. To make the two methods equivalent, we add to the Fourier series method two additional terms that correct erroneous evanescent field interactions between the cylinders and the planar interface. The significance of these terms should decay exponentially as the cylinders are separated from the interface.

Using the plane-wave integral method as a reference solution, we investigate the accuracy of the Fourier series method with and without evanescent correction terms. The Fourier series method with evanescent corrections should produce accurate results even when the cylinders are near the planar interface. Without the corrections, the method should converge as the

cylinders are separated from the interface. The convergence will depend on how far the Fourier series can extend into the complex domain to model evanescent field interactions between the cylinders and the interface. The significance of such interactions will also be isolated and examined.

5.2 Algorithm Outline

We approach the scattering problem by representing all the electromagnetic fields in terms of cylindrical wave modes, which will allow us to apply the boundary conditions around each cylinder directly. We will break down the scattering into five electromagnetic fields:

- A. V^i , the incident field, is an arbitrary beam of radiation. Evanescent field incidence is not considered.
- B. V^r is the reflection of the incident field from the planar interface. It can be calculated by numerically evaluating a plane-wave integral or by applying the Fourier series of the planar reflection coefficients.
- C. V^s , the scattered field emanating from a cylinder, is represented by outgoing cylindrical waves with unknown coefficients.
- D. V^d , the diffracted field emanating from an image cylinder, accounts for the reflection of a cylinder's scattered field V^s from the planar interface. From the scattered field V^s there may be both radiative and evanescent waves incident upon the interface.
- E. V^t , the transmitted field inside of a cylinder, accounts for the field that penetrates a dielectric cylinder.

For transverse magnetic (TM) polarization $V = E_z$ and for transverse electric (TE) polarization $V = H_z$. In isotropic two-dimensional scattering

5.3.1 V^i - Incident Field

An arbitrary incident beam is created by using the radiative part of a plane-wave spectrum:

$$V^i(x, y) = \frac{1}{2\pi} \int_{-k}^k F(k_y) \exp[-jk_x x - jk_y y] dk_y. \quad (5.1)$$

The wave vector has components $\vec{k} = (k_x, k_y, 0)$, and its magnitude in medium 1 is $k = \omega\sqrt{\epsilon_1\mu_0}$. The spatial frequency content is given by

$$F(k_y) = \int_{-\infty}^{\infty} V^i(0, y) \exp(jk_y y) dy, \quad (5.2)$$

where $V^i(0, y)$ defines the arbitrary beam shape.

We now convert to cylindrical coordinates (ρ, θ) and change the variable of integration into an angular form $k_y = k \sin(\delta)$:

$$V^i(\rho, \theta) = \frac{k}{2\pi} \int_{-\pi/2}^{\pi/2} F[k \sin(\delta)] \cos(\delta) \exp[-jk\rho \cos(\theta - \delta)] d\delta. \quad (5.3)$$

Using Bessel function identities [81] we can transform (5.3) into a sum of cylindrical wave modes:

$$V^i(\rho, \theta) = \sum_{m=-\infty}^{\infty} j^{-m} J_m(k\rho) \exp(jm\theta) A_m, \quad (5.4)$$

$$A_m = \frac{k}{2\pi} \int_{-\pi/2}^{\pi/2} F[k \sin(\delta)] \cos(\delta) \exp(-jm\delta) d\delta. \quad (5.5)$$

By applying the Graf addition theorem [96], the incident field is translated to the coordinates of each cylinder v :

$$V^i(\rho_v, \theta_v) = \sum_{n=-\infty}^{\infty} j^{-n} J_n(k\rho_v) \exp(jn\theta_v) A_n, \quad (5.6)$$

$${}_v A_n = \sum_{m=-\infty}^{\infty} j^{n-m} J_{m-n}(k\rho_{v0}) \exp[j(m-n)\theta_{v0}] A_m, \quad (5.7)$$

where ${}_v A_n$ are the coefficients A_m translated from the incident field origin to cylinder v .

This translational method only works well for radiative fields. In Chapter 2 it was shown that when evanescent fields are represented as a sum of Bessel functions of the first kind, they converge spatially outward as the modal truncation is extended. If they are translated using the Graf addition theorem, they often end up outside of their region of convergence. Therefore, if evanescent wave incidence is desired, the numerical integration scheme proposed in Chapter 4 must be used to translate the evanescent fields.

5.3.2 V^r - Incident Field Reflection

For plane-waves incident upon a planar interface between two dielectric half-spaces, we have the well-known reflection coefficients (5.8,5.9), which depend on the angle of incidence δ , the permittivities of the two half-spaces ϵ_1 and ϵ_2 , and the polarization. It is important to note that TM and TE polarizations are not the same with reference to cylinders and planar interfaces; we will maintain the convention for cylinders throughout. For our TM polarization the reflection coefficients are

$$R(\delta) = \frac{\cos(\delta) - \sqrt{\frac{\epsilon_2}{\epsilon_1} - \sin^2(\delta)}}{\cos(\delta) + \sqrt{\frac{\epsilon_2}{\epsilon_1} - \sin^2(\delta)}}, \quad (5.8)$$

and for our TE polarization they are

$$R(\delta) = \frac{\frac{\epsilon_2}{\epsilon_1} \cos(\delta) - \sqrt{\frac{\epsilon_2}{\epsilon_1} - \sin^2(\delta)}}{\frac{\epsilon_2}{\epsilon_1} \cos(\delta) + \sqrt{\frac{\epsilon_2}{\epsilon_1} - \sin^2(\delta)}}. \quad (5.9)$$

To form the reflected field from the incident field, we propagate the in-

cident field to the planar interface, apply the reflection coefficients (5.8,5.9), and then propagate it to a cylinder v . Taking (5.3) and representing the propagation to and from the interface using the image coordinates $(\tilde{\rho}, \tilde{\theta})$, we obtain

$$V^r(\tilde{\rho}, \tilde{\theta}) = \frac{k}{2\pi} \int_{-\pi/2}^{\pi/2} R(\delta) F[k \sin(\delta)] \cos(\delta) \exp[jk\tilde{\rho} \cos(\tilde{\theta} + \delta)] d\delta. \quad (5.10)$$

The tildes $\tilde{}$ are used to denote image coordinates and dimensions as shown in Figure 5.1. Converting the exponential to Bessel functions and translating the field to the coordinates of cylinder v using the Graf addition theorem yields

$$V^r(\rho_v, \theta_v) = \sum_{n=-\infty}^{\infty} j^{-n} J_n(k\rho_v) \exp(jn\theta_v) {}_vQ_n, \quad (5.11)$$

$${}_vQ_n = \sum_{m=-\infty}^{\infty} j^{m+n} J_{m-n}(k\tilde{\rho}_{v0}) \exp[j(m-n)\tilde{\theta}_{v0}] Q_m, \quad (5.12)$$

$$Q_m = \frac{k}{2\pi} \int_{-\pi/2}^{\pi/2} R(\delta) F[k \sin(\delta)] \cos(\delta) \exp(jm\delta) d\delta, \quad (5.13)$$

where ${}_vQ_n$ are the coefficients Q_m translated from the image of the incident field to cylinder v . As seen in Figure 5.1, the vector $(\tilde{\rho}_{v0}, \tilde{\theta}_{v0})$ points from the image of the incident field to cylinder v .

For the plane-wave integral method, we evaluate (5.13) numerically. Alternatively, we can express $R(\delta)$ as a Fourier series:

$$R(\delta) = \sum_{m=-\infty}^{\infty} R_m \exp(jm\delta), \quad (5.14)$$

$$R_m = \frac{1}{2\pi} \int_{-\pi}^{\pi} R(\delta) \exp(-jm\delta) d\delta. \quad (5.15)$$

Using this notation is the key to the Fourier series method, as it allows us to avoid numerical integration. Inserting the Fourier series representation

(5.14) into (5.13) yields the convolutional sum:

$$Q_m = \sum_{l=-\infty}^{\infty} R_{-l-m} A_l. \quad (5.16)$$

Reflection from the planar interface occurs at real angles $-\pi/2 \leq \delta \leq \pi/2$ for radiative waves and at complex angles $\pm\pi/2 \pm ju$, $0 < u < \infty$, for evanescent waves. As pointed out by Coatanhay and Conoir [47], the Fourier series (5.14) is equivalent to a Laurent series in complex space:

$$R(\delta) = \sum_{m=-\infty}^{\infty} R_m z^m, \quad (5.17)$$

where $z = \exp(j\delta)$. The Laurent series (5.17) will converge in the annulus $r_1 < |z| < r_2$, extending from the unit circle $r_1 < 1 < r_2$, if $R(\delta)$ is analytic within the annulus [97]. Therefore, the Laurent series can only model the reflection of evanescent waves with complex angles $\delta = \pm\pi/2 \pm ju$ that satisfy $r_1 < \exp(\mp u) < r_2$. The limits of the annulus (r_1, r_2) depend on the function $R(\delta)$, where smoother functions tend to have wider limits [48].

The reflection coefficients for TE polarization (5.9) contain a singularity on $|z| = 1$ that makes it impossible to calculate the Laurent series there. The singularity always occurs within the angles of incidence that point away from the interface $\pi/2 < |\delta| < \pi$ and do not represent a physical situation. Allowing $R(\delta)$ to take on arbitrary values in this region will not affect the real angles of incidence $0 < |\delta| < \pi/2$, but it will affect the Laurent series' convergence. To remove the singularity and maintain smoothness, it is expedient to fit a spline to the region $\pi/2 < |\delta| < \pi$ in (5.9) before integrating (5.15).

5.3.3 V^s - Scattered Fields from Cylinders

The scattered field from each cylinder v can be represented as a sum of cylindrical waves:

$$V^{sv}(\rho_v, \theta_v) = \sum_{n=-\infty}^{\infty} j^{-n} H_n^{(2)}(k\rho_v) \exp(jn\theta_v) {}_v b_n. \quad (5.18)$$

The scattering coefficients ${}_v b_n$ are the unknowns that we are ultimately trying to solve for.

By applying the Graf addition theorem, the scattered field (5.18) from cylinder w can be represented in the coordinate system of cylinder v :

$$V^{sw}(\rho_v, \theta_v) = \sum_{n=-\infty}^{\infty} j^{-n} J_n(k\rho_v) \exp(jn\theta_v) {}_{vw} B_n, \quad (5.19)$$

$${}_{vw} B_n = \sum_{m=-\infty}^{\infty} j^{n-m} H_{m-n}^{(2)}(kd_{vw}) \exp[j(m-n)\phi_{vw}] {}_w b_m. \quad (5.20)$$

5.3.4 V^d - Diffracted Fields from the Planar Interface

The scattered fields from the cylinders (5.18) will propagate to the planar interface and partially reflect from the surface. To completely account for the multiple scattering interactions that occur between the cylinders and the interface, we need to find a representation for this diffracted field in terms of the scattering coefficients ${}_v b_n$. We begin by transforming a cylindrical wave emanating from cylinder w , into plane-waves using the Sommerfeld integral [98]:

$$H_n^{(2)}(k\rho_w) \exp(jn\theta_w) = \frac{j^n}{\pi} \int_{C1} \exp[jn\delta - jx_w k \cos(\delta) - jy_w k \sin(\delta)] d\delta, \quad (5.21)$$

where the contour $C1$ is taken from $-\pi/2 - j\infty$ to $\pi/2 + j\infty$ as shown in Figure 5.2. Cincotti et al. [49] derived a similar plane-wave expansion for

Hankel functions of the first kind.

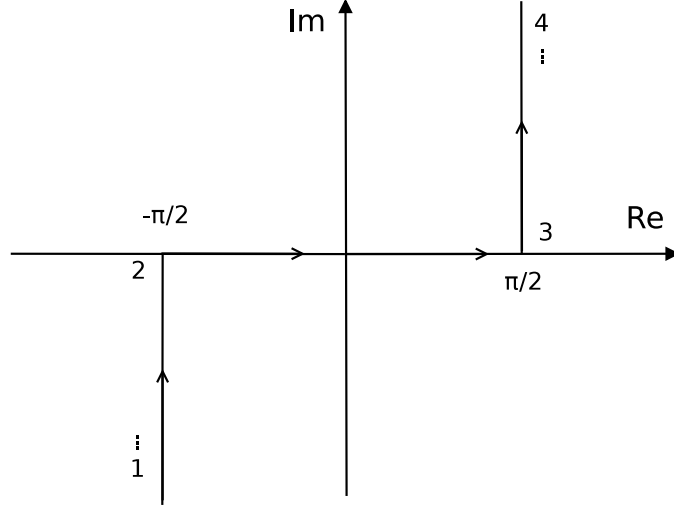


Figure 5.2: The integration contour $C1$ follows the path 1-2-3-4. The contour $C2$ includes the paths 1-2 and 3-4 only. The points 1 and 4 extend infinitely, parallel to the imaginary axis.

To calculate the reflection of this wave (5.21), we propagate it to the planar interface, apply the reflection coefficients (5.8, 5.9), and propagate it to a cylinder v . Again, the propagation to and from the interface is done by taking the image cylinder's coordinates $(\tilde{\rho}_w, \tilde{\theta}_w)$ and translating them to the coordinates of cylinder v :

$$C^w(\rho_v, \theta_v) = \frac{j^n}{\pi} \int_{C1} R(\delta) \exp[jk\rho_v \cos(\theta_v + \delta)] \exp[jn\delta + jk\tilde{d}_{wv} \cos(\tilde{\phi}_{wv} + \delta)] d\delta, \quad (5.22)$$

where C^w is the reflection of the cylindrical wave $H_n^{(2)}(k\rho_w) \exp(jn\theta_w)$ from the interface. The exponential is now converted into a sum of Bessel functions and we substitute the entire expression (5.22) into the scattered field for cylinder w (5.18):

$$V^{dw}(\rho_v, \theta_v) = \sum_{n=-\infty}^{\infty} j^{-n} J_n(k\rho_v) \exp(jn\theta_v)_{wv} D_n, \quad (5.23)$$

$${}_{wv}D_n = \frac{(-1)^n}{\pi} \sum_{m=-\infty}^{\infty} {}_w b_m \int_{C1} R(\delta) \exp[j(n+m)\delta + jk\tilde{d}_{wv} \cos(\tilde{\phi}_{wv} + \delta)] d\delta. \quad (5.24)$$

The diffracted field V^{dw} represents the reflection of the scattered field V^{sw} from the interface, using the coordinates of cylinder v .

If we use numerical integration in (5.24), we obtain the plane-wave integral method [52–54, 56–58], which is well known. Use of the Fourier series method will allow us to avoid numerical integration in (5.24), but it may no longer be an exact solution since the evanescent wave reflections may be partially misrepresented. We will therefore develop two evanescent field correction terms for our Fourier series approach: the first term ${}_{wv}U1_n$ removes the erroneous evanescent wave reflections, and the second ${}_{wv}U2_n$ contains the true evanescent wave reflections. The coefficients ${}_{wv}D_n$ can now be broken down into three components ${}_{wv}D_n = {}_{wv}U0_n - {}_{wv}U1_n + {}_{wv}U2_n$, with ${}_{wv}U0_n$ being the term for the uncorrected Fourier series method. Substituting the Fourier series (5.14) into (5.24) and converting back to Hankel functions using the Sommerfeld integral (5.21) produces

$${}_{wv}U0_n = \sum_{l=-\infty}^{\infty} j^{l+n} \mathbf{H}_{l-n}^{(2)}(k\tilde{d}_{wv}) \exp[j(l-n)\tilde{\phi}_{wv}] {}_wU0_l, \quad (5.25)$$

$${}_wU0_l = \sum_{m=-\infty}^{\infty} R_{-l-m} {}_w b_m. \quad (5.26)$$

where ${}_{wv}U0_n$ are the coefficients ${}_wU0_l$ translated from image cylinder w to cylinder v .

It is important to note that (5.25) is in the form of the Graf addition theorem for Hankel functions, which is a translational operation. If we remain in the coordinates of image cylinder w , the uncorrected Fourier series method produces

$$V^{dw}(\tilde{\rho}_w, \tilde{\theta}_w) = \sum_{n=-\infty}^{\infty} j^n \mathbf{H}_n^{(2)}(k\tilde{\rho}_w) \exp(jn\tilde{\theta}_w) {}_wU0_n, \quad (5.27)$$

which represents the diffracted field from the planar interface as scattered fields emanating from the image cylinders. This notation is useful for modelling the electromagnetic fields in the far-field where the evanescent waves have died away.

The evanescent field correction terms are derived by separating out the evanescent regions of the integral in (5.24), which follow the paths in $C2$ from Figure 5.2. The first term ${}_{wv}U1_n$ represents the erroneous evanescent fields from the Fourier series coefficients (5.14), and the second term ${}_{wv}U2_n$ represents the true evanescent fields using $R(\delta)$. After changing the integration variable and simplifying, we obtain

$${}_{wv}U1_n = (-1)^n \sum_{l=-\infty}^{\infty} {}_wU0_l \int_0^{\infty} {}_{wv}W_{n-l}(u) du, \quad (5.28)$$

$${}_{wv}U2_n = (-1)^n \sum_{m=-\infty}^{\infty} {}_wb_m \int_0^{\infty} R\left(\frac{\pi}{2} + ju\right) {}_{wv}W_{n+m}(u) du, \quad (5.29)$$

where

$$\begin{aligned} {}_{wv}W_p(u) = & \frac{j2}{\pi} \exp[k\tilde{d}_{wv} \cos(\tilde{\phi}_{wv}) \sinh(u)] \cdot \\ & \cos\left[p\left(\frac{\pi}{2} + ju\right) - k\tilde{d}_{wv} \sin(\tilde{\phi}_{wv}) \cosh(u)\right]. \end{aligned} \quad (5.30)$$

The numerical evaluation of the true evanescent fields (5.29) is common between the plane-wave integral method (5.24) and the Fourier series method.

Including the evanescent field correction terms in the solution is not always necessary. The significance of ${}_{wv}U1_n$ and ${}_{wv}U2_n$ depends on the convergence limits of the Laurent series (5.17), and the separation distance between the cylinders and the planar interface. The convergence limits of the Laurent series will be determined by the permittivity contrast ϵ_2/ϵ_1 and the wave polarization. If the cylinders have different separation distances from the planar interface, it may only be necessary to compute ${}_{wv}U1_n$ and ${}_{wv}U2_n$ for specific cylinders w and v . The numerical simulations demonstrate the significance

of the evanescent field correction terms under various conditions.

5.3.5 V^t Transmitted Fields Inside the Cylinders

The fields transmitted inside the dielectric cylinders can be represented by cylindrical waves:

$$V^{tv}(\rho_v, \theta_v) = \sum_{n=-\infty}^{\infty} j^{-n} J_n(k_v \rho_v) \exp(jn\theta_v) {}_v d_n, \quad (5.31)$$

with unknown coefficients ${}_v d_n$. The wavenumber inside cylinder v is denoted $k_v = \omega \sqrt{\epsilon_v \mu_0}$.

5.3.6 Applying the Cylinders' Boundary Conditions

We will consider homogeneous dielectric cylinders where $\epsilon_v \neq \epsilon_0$ and $\mu_v = \mu_0$. The boundary conditions require that the tangential components of the electric and magnetic fields must be continuous across the boundary of each cylinder. For both polarizations, at the surface of the cylinders $\rho_v = a_v$, the first boundary condition is

$$V^i + V^r + \sum_v V^{sv} + \sum_v V^{dv} = V^{tv}. \quad (5.32)$$

For the TM case, the magnetic boundary condition is

$$\frac{\partial}{\partial \rho_v} [V^i + V^r + \sum_v V^{sv} + \sum_v V^{dv}] = \frac{\partial}{\partial \rho_v} V^{tv}, \quad (5.33)$$

and for the TE case, the electric boundary condition is

$$\frac{1}{\epsilon_1} \frac{\partial}{\partial \rho_v} [V^i + V^r + \sum_v V^{sv} + \sum_v V^{dv}] = \frac{1}{\epsilon_v} \frac{\partial}{\partial \rho_v} V^{tv}. \quad (5.34)$$

Solving the set of two equations: (5.32) with (5.33) or (5.32) with (5.34), for the scattering coefficients, yields

$${}_v b_n = {}_v f_n [{}_v A_n + {}_v Q_n + \sum_{w \neq v} {}_{wv} B_n + \sum_w {}_{wv} D_n], \quad (5.35)$$

where ${}_v f_n$ are the single scattering coefficients for dielectric cylinders, similar to Chapter 4. For TM polarization, the single scattering coefficients are

$${}_v f_n = \frac{J_n(k_v a_v) J_n'(k a_v) - \sqrt{\frac{\epsilon_v}{\epsilon_1}} J_n(k a_v) J_n'(k_v a_v)}{\sqrt{\frac{\epsilon_v}{\epsilon_1}} J_n'(k_v a_v) H_n^{(2)}(k a_v) - H_n^{(2)'}(k a_v) J_n(k_v a_v)}, \quad (5.36)$$

and for TE polarization they are

$${}_v f_n = \frac{\sqrt{\frac{\epsilon_v}{\epsilon_1}} J_n(k_v a_v) J_n'(k a_v) - J_n(k a_v) J_n'(k_v a_v)}{J_n'(k_v a_v) H_n^{(2)}(k a_v) - \sqrt{\frac{\epsilon_v}{\epsilon_1}} H_n^{(2)'}(k a_v) J_n(k_v a_v)}, \quad (5.37)$$

where the primes denote a derivative with respect to the function's argument.

Equation (5.35) can be evaluated iteratively or through matrix inversion. If the ${}_{wv} B_n$ and ${}_{wv} D_n$ coefficients are set to zero initially then (5.35) can be solved iteratively by updating the values of the scattering coefficients ${}_v b_n$. We can also define an exact matrix inverse solution. The well-known plane-wave integral solution [52–54, 56–58] is given by the system

$$\vec{L} = (\mathbf{F}^{-1} - \mathbf{G3} - \mathbf{D})^{-1} (\mathbf{G1}\vec{A} + \mathbf{G2}\vec{Q}). \quad (5.38)$$

The equivalent Fourier series solution is given by the system

$$\vec{L} = [\mathbf{F}^{-1} - \mathbf{G3} - (\mathbf{G4} - \mathbf{U1})\mathbf{R2} - \mathbf{U2}]^{-1} (\mathbf{G1} + \mathbf{G2}\mathbf{R1})\vec{A}, \quad (5.39)$$

and the uncorrected Fourier series method [47, 48] is given by the system

$$\vec{L} = (\mathbf{F}^{-1} - \mathbf{G3} - \mathbf{G4}\mathbf{R2})^{-1} (\mathbf{G1} + \mathbf{G2}\mathbf{R1})\vec{A}. \quad (5.40)$$

Table 5.1: The matrices are linked to their corresponding equations.

Matrix	Equation	Matrix	Equation	Matrix	Equation
G1	(5.7)	R1	(5.16)	\vec{A}	(5.5)
G2	(5.12)	R2	(5.26)	\vec{Q}	(5.13)
G3	(5.20)	U1	(5.28)	F	(5.36) or (5.37)
G4 ($U0$)	(5.25)	U2	(5.29)	D	(5.24)

The elements of each matrix are taken directly from the equations referenced by Table 5.1. The vector \vec{L} contains the scattering coefficients ${}_v b_n$, the vector \vec{A} contains the incident field coefficients A_n , and the vector \vec{Q} contains the reflected field coefficients Q_n . The **R** matrices are made up of the Fourier series coefficients and the **G** matrices are Graf addition theorem matrices that translate coefficients from one coordinate system to another. The **U** matrices are for evanescent field corrections. Similar to Chapter 4, the diagonal matrix **F** contains the single scattering coefficients. The matrix **D**, or its equivalent $(\mathbf{G4} - \mathbf{U1})\mathbf{R2} + \mathbf{U2}$, accounts for the multiple scattering between the cylinders and the planar interface.

For comparison, we can also calculate the scattering from multiple cylinders without a planar interface [8, 24, 25, 28, 29, 34, 35, 92]:

$$\vec{L} = (\mathbf{F}^{-1} - \mathbf{G3})^{-1} \mathbf{G1} \vec{A}, \quad (5.41)$$

and the scattering from a single cylinder [20, 85]:

$$\vec{L} = \mathbf{FG1} \vec{A}, \quad (5.42)$$

using the same matrices from Table 5.1.

5.4 Numerical Simulations

Three numerical simulations will be performed to demonstrate the accuracy of the Fourier series method and the strength of the evanescent field interactions. The first simulation compares the well-known plane-wave integral method (5.38) to the Fourier series method with both evanescent field correction terms (5.39). Theoretically, the two methods should produce identical results regardless of the separation distance between the cylinders and the planar interface. The second simulation compares the Fourier series method with both evanescent field correction terms (5.39) to the uncorrected Fourier series method (5.40). As the cylinders are moved closer to the interface, the error produced by the uncorrected Fourier series method (5.40) should increase due to stronger evanescent field interactions. The final simulation compares the solutions of the Fourier series method (5.39) with and without the true evanescent field interaction term $\mathbf{U2}$. This last simulation demonstrates the significance of evanescent field interactions between the cylinders and the interface. For all three simulations the general setup is shown in Figure 5.3.

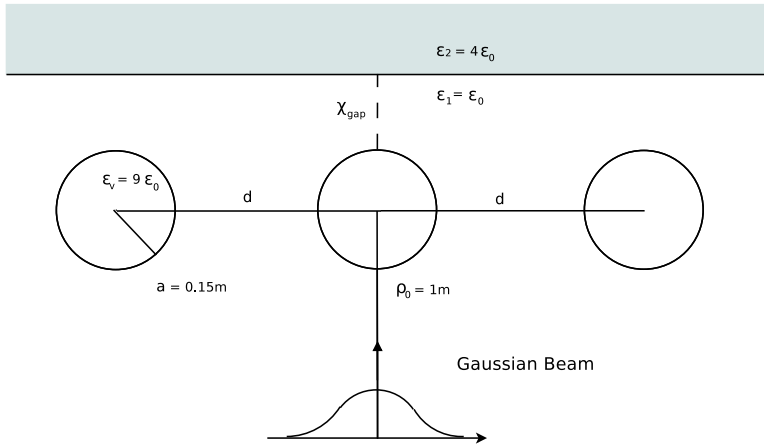


Figure 5.3: A Gaussian beam is scattered from three identical dielectric cylinders near a dielectric half-space. The incident Gaussian beam has a waist size of $w_0 = 1$, an amplitude factor of $E_0 = 1$, and a frequency $f = 1\text{GHz}$ ($\lambda \approx 0.3\text{m}$).

When computing the solution (5.38, 5.39, 5.40) numerically, the infinite sums of cylindrical wave modes need to be truncated to appropriate limits. For the incident field and its reflection from the planar interface, the mode limit will depend on the shape of the incident beam. For the fields scattered from the cylinders and image cylinders, the truncation limits will be proportional to the factor ka_v . Choosing appropriate truncation limits in cylindrical scattering was investigated in Chapter 3.

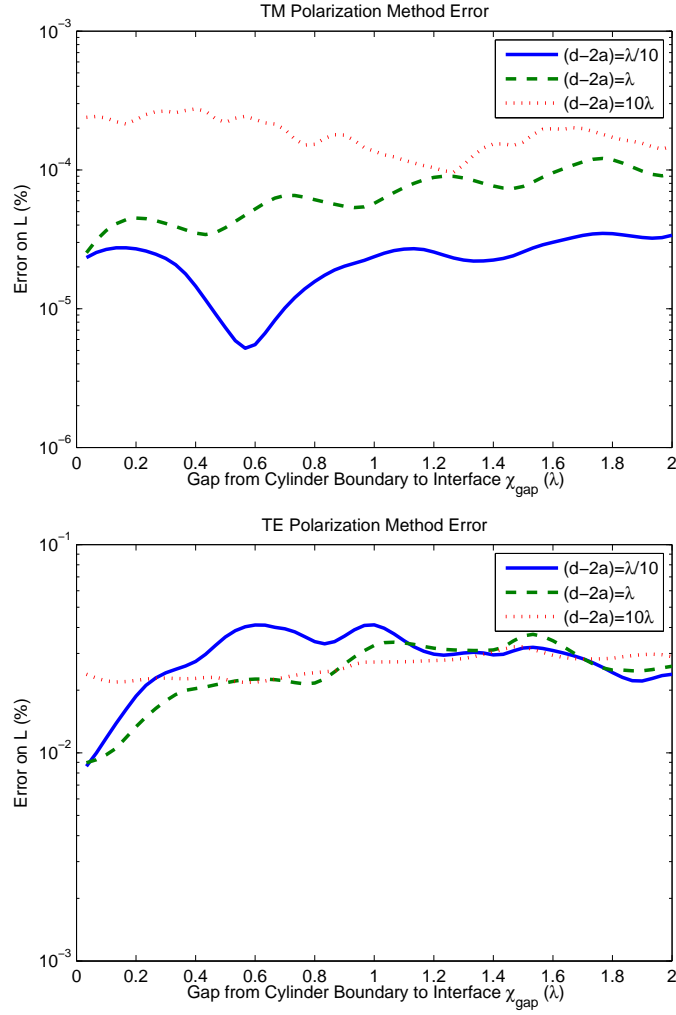


Figure 5.4: The error in \vec{L} between the Fourier series method with evanescent field corrections (5.39) and the plane-wave integral method (5.38) is shown for TM and TE polarizations.

First, we verify that the Fourier series method with both evanescent field correction terms (5.39) produces similar results to the plane-wave integral method (5.38). The three cylinders are illuminated by a Gaussian beam as shown in Figure 5.3, and the solutions are calculated multiple times with various distances between the planar interface and the cylinders χ_{gap} , and

between the cylinders d . The results for TM and TE polarizations are shown in Figure 5.4. The small numerical error between the two methods is due to modal truncation [99] and numerical integration. Therefore, the two methods produce equivalent results regardless of the scattering setup.

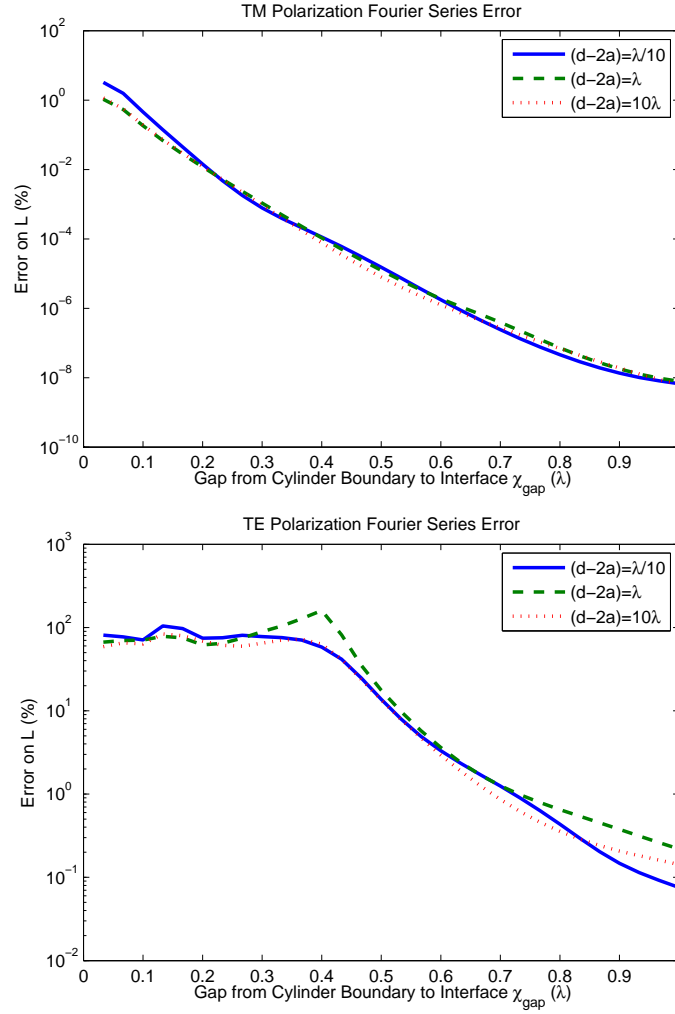


Figure 5.5: The error in \vec{L} between the Fourier series method with (5.39) and without (5.40) evanescent field corrections is shown for TM and TE polarizations.

Now that we have verified the accuracy of the Fourier series method with

evanescent field corrections (5.39), we compare it to the Fourier series method without the two evanescent field correction terms (5.40). The simulations are performed using the same setup shown in Figure 5.3. The TM and TE polarization results are shown in Figure 5.5. In the TM case, the error dies away very quickly as the cylinders are separated from the interface. For a 1% error tolerance, the evanescent field correction terms would only become necessary when $\chi_{gap} < \lambda/10$. In the TE case, the error extends further before decaying, which indicates that the annulus of convergence of the Laurent series (5.17) must be narrower than in the TM case. We would expect a narrow convergence because the Laurent series for the TE coefficients (5.9) was calculated using an 8th order spline to remove a singularity. For a 1% error tolerance, the evanescent field correction terms would become necessary when $\chi_{gap} < 3\lambda/4$.

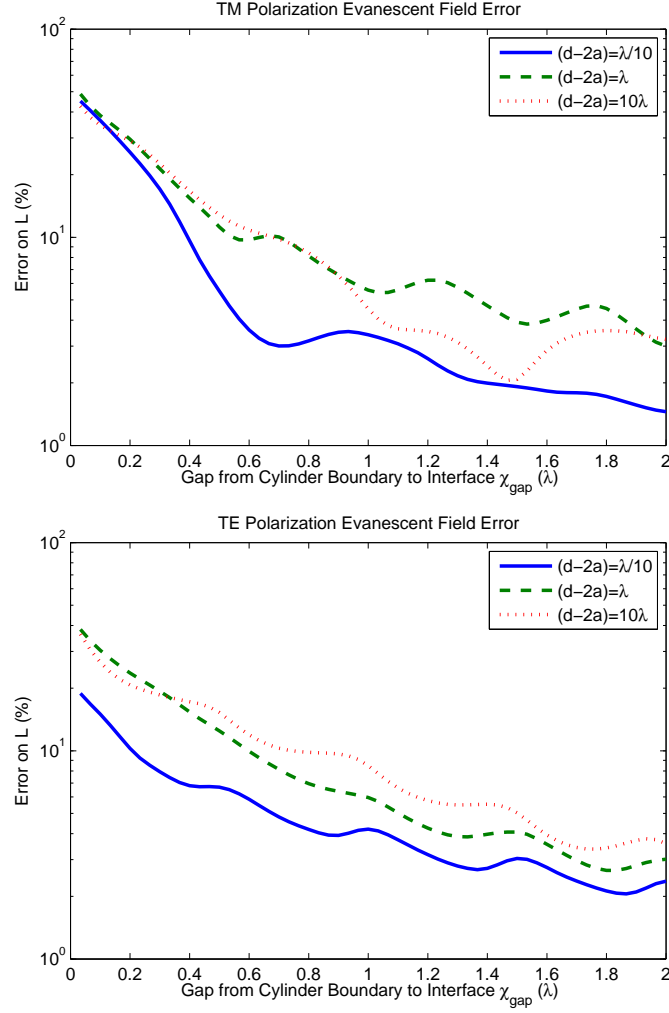


Figure 5.6: The error in \vec{L} between the Fourier series method with and without the true evanescent field interaction term **U2** is shown for TM and TE polarizations.

Finally, we compare the Fourier series method (5.39) with and without the true evanescent field interaction term **U2**. These simulations show the effect of not considering evanescent field interactions between the cylinders and the planar interface. The error plots for TM and TE polarizations are shown in Figure 5.6. The evanescent field interactions between the interface

and the cylinders can remain significant until the separation distance χ_{gap} reaches a few wavelengths. The effect of the true evanescent fields in the scattering between the cylinders and the interface dies away much slower than the error due to the uncorrected Fourier series method. This indicates that the uncorrected Fourier series method accounts for some of the evanescent field interactions between the cylinders and the interface, which is what we would expect if the Laurent series (5.17) converged partially into the complex domain.

Many other configurations of cylinder sizes, separation distances, and permittivity contrasts were simulated to confirm that these conclusions hold in the general case. In the case where $\epsilon_2/\epsilon_1 < 1$, both coefficients (5.8,5.9) become non-smooth and their Laurent series have narrower convergence limits.

5.5 Conclusion

Two approaches to the scattering from cylinders near a dielectric half-space were derived and compared: the plane-wave integral method [52–54, 56–58] and the Fourier series method [47, 48]. The plane-wave integral method provides an accurate solution but requires a significant amount of numerical integration that can be computationally intensive. The Fourier series method avoids numerical integration but it can only accurately represent the reflection of a limited range of evanescent waves. When the cylinders are very close to the dielectric half-space, the evanescent wave interactions may be distorted. To overcome this deficiency, we introduced evanescent field correction terms: **U1** and **U2**. The cylinder-to-interface interaction matrix **D** in the plane-wave integral method is exactly equal to the corrected Fourier series matrix $(\mathbf{G4} - \mathbf{U1})\mathbf{R2} + \mathbf{U2}$. However, numerical simulations demonstrated that the uncorrected Fourier series method (5.40) converges faster with respect to χ_{gap} than the solution (5.39) without the true evanescent field interactions between the cylinders and the planar interface provided by

U2. This implies that the uncorrected Fourier series method is able to accurately model part of the evanescent field interactions. This was attributed to the fact that the Fourier series becomes a Laurent series in complex space and converges within an annulus extending from the real angles.

A summary of the advantages of using the evanescent corrected Fourier series method (5.39) is provided below.

- i. It produces accurate results for cylinders close to the planar interface.
- ii. For cylinders far from the interface, the evanescent field corrections can be left out, yielding a fast computational implementation.
- iii. Numerical integration is not necessary for calculating the reflection of the incident beam (5.16).
- iv. Modelling the diffracted fields V^d in the far-field is made efficient through the use of image cylinders (5.27).

Our GMI solution can also be verified in the limiting case by taking $\frac{\epsilon_2}{\epsilon_1} \rightarrow \infty$, so that the dielectric half-space now acts like a perfect conductor. In this case, the Fourier series has only one coefficient $R_0 = -1$, so it converges inside the entire complex plane. The evanescent interaction terms **U1** and **U2** disappear and the main term **G4R2** becomes the representation of perfect image cylinders. Thus, our solution converts directly into the method of images for a conducting plane.

Our evanescent wave corrected GMI was formed in order to simulate apertureless near-field scanning optical microscopy (ANSOM) imaging, where evanescent fields interact between samples, probes, and substrates [61, 86, 100]. Such an analytical solution is able to give insight into the role of multiple scattering in ANSOM experiments. The evanescent field interactions are particularly important in ANSOM, as evanescent waves from an illuminated sample are converted into radiative waves by a probe. As demonstrated

by our simulations, an evanescent field's multiple scattering interactions can effect the scattering coefficients significantly.

Chapter 6

Multiple Scattering Between Cylinders in Two Dielectric Half-Spaces

6.1 Introduction

The scattering from multiple cylinders near a dielectric half-space has applications in ground penetrating radar (GPR), remote sensing of the earth, metamaterials, photonic crystals, and optical imaging. Several numerical techniques have been proposed for calculating the scattering from cylinders near planar interfaces, including extinction theorem [94, 101], pseudospectral time-domain algorithms [102, 103], and the method of moments [93]. In our approach, we use a cylindrical wave decomposition to find an analytical-numerical solution to the scattering problem that is accurate, computes quickly, and provides insight into the multiple scattering behaviour of the system.

For an analytical approach to the scattering problem, we need to consider both cylindrical waves and plane-waves. To satisfy the boundary conditions for a planar interface separating two dielectric half-spaces, the electromagnetic fields must be broken down into plane-waves. To satisfy the boundary conditions for a cylinder, cylindrical waves must be used. Therefore, the inclusion of both cylinders and a planar interface will require the transformation of cylindrical waves into plane-waves and vice-versa. Cincotti et al. [49] explicitly derived the plane-wave expansion for a cylindrical wave

with a Hankel function of the first kind. A major difficulty here is that the transformation from cylindrical waves to plane-waves leaves a numerical integral that can be complicated and time consuming to compute [50, 51].

For cylinders on one side of a dielectric half-space, Borghi et al. [53, 54], and Lee and Grzesik [56] proposed scattering algorithms that use a transformation of cylindrical waves into plane-waves. Since they make no approximations, their scattering algorithms apply to all cases, but the numerical integrals involved can be difficult to compute.

The method of images can be applied for conducting planes [43–45] and other planar interfaces where the reflection from the interface is not angle-dependent [52]. The reflection of a cylinder’s scattered field from the planar interface can be modelled by an image cylinder on the opposite side of the conducting plane. The method of images provides an exact analytical solution to the multiple scattering without requiring numerical integration.

Coatanhay and Conoir [47, 48] introduced a method for modelling the reflection of cylindrical waves from a penetrable, angle-dependent interface without having to convert to plane-waves. Their method involves taking the Fourier series of the planar reflection coefficients of the interface. Once in this form, the reflection from the interface can be modelled by an image cylinder with scattering coefficients equal to the convolutional sum of the Fourier series coefficients and the cylinder’s scattering coefficients. Their method does not require numerical integration but may fail when the cylinders are very close to the interface due to erroneous evanescent field reflections. This method was adapted for electromagnetic scattering in Chapter 5, where evanescent wave correction terms were also derived.

Transmission of cylindrical waves across a planar interface has been considered by Ciambra et al. [40], Ahmed and Naqvi [39] and Di Vico et al. [55]. The scattered fields emanating from buried conducting cylinders are translated back into the initial medium using a cylindrical wave to plane-wave transformation. The resulting numerical integrals are investigated in detail.

Transmission of cylindrical waves through a planar interface was also considered for cylinders embedded in a dielectric slab [41, 57, 58]. The dielectric slabs have two planar interfaces, which cause the cylindrical waves to reflect multiple times between them. Each time a wave reflects inside the dielectric slab, part of the wave is transmitted to the outer medium.

Our scattering model incorporates cylinders in two dielectric half-spaces, which means that the scattered fields from cylinders in one half-space interact with the cylinders in the other half-space. To do this, we use a decomposition of cylindrical waves into plane-waves. This decomposition introduces integrals that must be solved numerically. When the cylinders are significantly separated from the interface, we can approximate the integrals using the method of stationary phase [104, 105]. Numerical simulations are used to compare the accuracy, efficiency, and limitations of the solution computed using the stationary phase approximation with the solution computed using direct numerical integration.

6.2 Scattering Theory

We consider the two-dimensional scattering of a plane-wave from multiple dielectric cylinders in two dielectric half-spaces. In our approach, we compute the boundary conditions in each dielectric half-space, then link the two formulations to define the full multiple scattering solution. The coordinate system shown in Figure 6.1 was created to have inversion symmetry in order to facilitate computation from the perspective of either half-space. The analysis that we do from the perspective of the first medium applies directly to the perspective of the second medium because of the inversion symmetry. The indices w and i refer to arbitrary cylinders in the first medium and the indices v and u refer to arbitrary cylinders in the second medium. The time dependence $\exp(j\omega t)$ is assumed and suppressed throughout.

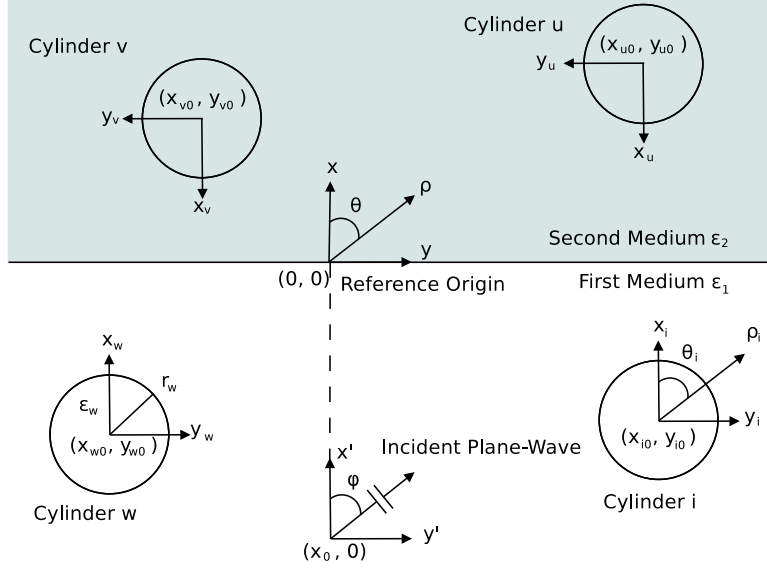


Figure 6.1: The coordinate systems and geometry for the scattering are shown. The z direction is normal to the page. The indices w and i refer to cylinders in the first medium and the indices v and u refer to cylinders in the second medium.

Our main objective is to satisfy the boundary conditions on the surface of the cylinders and the planar interface separating the two dielectric half-spaces. The tangential electric and magnetic fields must be continuous across all boundaries. For the planar interface, the boundary conditions can be satisfied by breaking down the incident fields into plane-waves and applying the well-known planar reflection and transmission coefficients. For the cylinders, the electromagnetic fields must be broken down into cylindrical waves centred about each cylinder. As shown in Figure 6.2, we break down the \hat{z} directed fields into five categories:

- A) V_p , the principal field, depends on which side of the dielectric half-space is being considered. For the first medium, it incorporates the incident plane-wave V_{inc} and its reflection from the planar interface V_{ref} . For the second medium, it is the transmission of the incident plane-wave through the interface V_{tr} .

- B) V_s , the total scattered field emanating from a cylinder, is represented by outgoing cylindrical waves with unknown coefficients.
- C) V_c , the total field inside of a cylinder, is represented by traversing cylindrical waves with unknown coefficients.
- D) V_r accounts for the reflection of a cylinder's scattered field V_s from the planar interface.
- E) V_t accounts for the transmission of a cylinder's scattered field V_s through the planar interface.

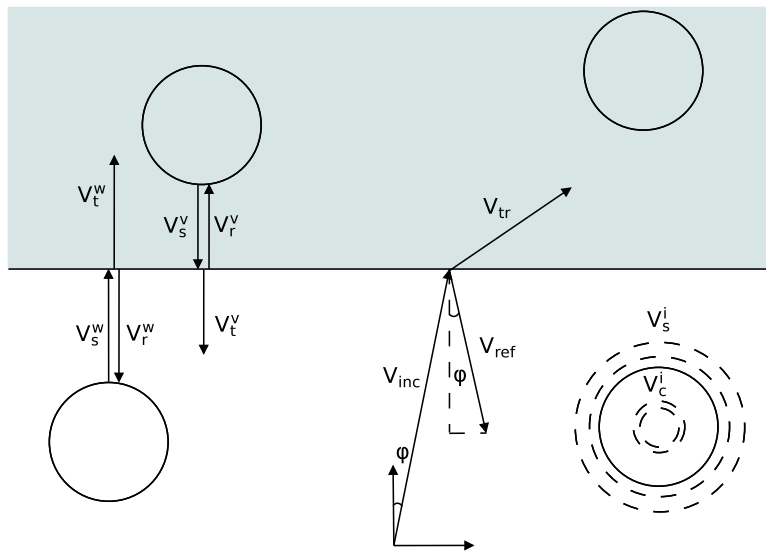


Figure 6.2: The break down of electromagnetic fields is depicted.

There is a problem defining the polarization states because the transverse magnetic (TM) convention for cylinders is the transverse electric (TE) convention for planar interfaces and vice-versa. We will use the convention for cylinders throughout. For the TM case $V = E_z$, and for the TE case $V = H_z$.

6.2.1 V_p Principal Field

For simplicity, we have chosen to use a single plane-wave as the incident field. Techniques for incorporating Gaussian beam incidence or arbitrary beam incidence have been presented for similar scattering problems [85, 92].

In the first medium, the principal field V_p incorporates the incident plane-wave V_{inc} and its reflection from the planar interface V_{ref} . In the second medium, the principal field V_p is the transmission of the incident plane-wave through the interface V_{tr} . If the incident plane-wave is

$$V_{inc} = \exp[-j\alpha y - j\beta(x - x_0)], \quad (6.1)$$

then its reflection from the interface is

$$V_{ref} = R(\alpha) \exp[-j\alpha y + j\beta(x + x_0)], \quad (6.2)$$

and its transmission through the interface is

$$V_{tr} = T(\alpha) \exp[-j\alpha y - j\gamma x + j\beta x_0], \quad (6.3)$$

where $\alpha = k_1 \sin(\phi)$ and $\beta = k_1 \cos(\phi)$. The incident plane-wave angle ϕ is shown in Figure 6.1. The wavenumber is defined in the first medium by $k_1 = \omega \sqrt{\epsilon_1 \mu_0}$ and in the second medium by $k_2 = \omega \sqrt{\epsilon_2 \mu_0}$. The perpendicular wave-vector component in the second medium can be calculated $\gamma = \sqrt{k_2^2 - \alpha^2}$.

The plane-wave reflection and transmission coefficients for the planar interface can be found by applying the boundary conditions across the interface. For TM polarization the reflection coefficients are

$$R(k_y) = \frac{k_{x1} - k_{x2}}{k_{x1} + k_{x2}}, \quad (6.4)$$

and for TE polarization they are

$$R(k_y) = \frac{(\epsilon_2/\epsilon_1)k_{x1} - k_{x2}}{(\epsilon_2/\epsilon_1)k_{x1} + k_{x2}}. \quad (6.5)$$

For TM polarization the transmission coefficients are

$$T(k_y) = \frac{2k_{x1}}{k_{x1} + k_{x2}}, \quad (6.6)$$

and for TE polarization they are

$$T(k_y) = \frac{(\epsilon_2/\epsilon_1)2k_{x1}}{(\epsilon_2/\epsilon_1)k_{x1} + k_{x2}}. \quad (6.7)$$

Since the parallel wave-vector component k_y is conserved across the planar interface, the perpendicular components can be calculated as $k_{x1} = \sqrt{k_1^2 - k_y^2}$ and $k_{x2} = \sqrt{k_2^2 - k_y^2}$.

The fields (6.1), (6.2), and (6.3) are translated to the coordinates of a cylinder i or u on their respective sides, and transformed into a sum of cylindrical waves. The transformation from plane-waves to cylindrical waves can be achieved by applying the Jacobi-Anger expansion [106]. Now the principal field in the first medium $V_p = V_{inc} + V_{ref}$, from the coordinates of a cylinder i , is

$$V_p(\rho_i, \theta_i) = \sum_{n=-\infty}^{\infty} j^{-n} J_n(k_1 \rho_i) \exp(jn\theta_i) (A_n^i + Q_n^i), \quad (6.8)$$

$$A_n^i = \exp[-j\alpha y_{i0} - j\beta(x_{i0} - x_0) - jn \sin^{-1}(\frac{\alpha}{k_1})], \quad (6.9)$$

$$Q_n^i = (-1)^n R(\alpha) \exp[-j\alpha y_{i0} + j\beta(x_{i0} + x_0) + jn \sin^{-1}(\frac{\alpha}{k_1})]. \quad (6.10)$$

and the principal field in the second medium $V_p = V_{tr}$, from the coordinates

of a cylinder u , is

$$V_p(\rho_u, \theta_u) = \sum_{n=-\infty}^{\infty} j^{-n} J_n(k_2 \rho_u) \exp(jn\theta_u) P_n^u, \quad (6.11)$$

$$P_n^u = (-1)^n T(\alpha) \exp[-j\alpha y_{u0} - j\gamma x_{u0} + j\beta x_0 - jn \sin^{-1}(\frac{\alpha}{k_2})]. \quad (6.12)$$

6.2.2 V_s Scattered Field from a Cylinder

The scattered field from a cylinder i in the first medium can be represented as a sum of outgoing cylindrical waves:

$$V_s^i(\rho_i, \theta_i) = \sum_{n=-\infty}^{\infty} j^{-n} H_n^{(2)}(k_1 \rho_i) \exp(jn\theta_i) b_n^i. \quad (6.13)$$

The scattering coefficients b_n^i , along with b_n^u from the cylinders on the opposite side of the half-space, are the unknowns that we are ultimately trying to solve for.

In the first medium, the scattered field (6.13) from a cylinder w can be represented in the coordinate system of a cylinder i by applying the Graf addition theorem [96]:

$$V_s^w(\rho_i, \theta_i) = \sum_{n=-\infty}^{\infty} j^{-n} J_n(k_1 \rho_i) \exp(jn\theta_i) B_n^{wi}, \quad (6.14)$$

$$B_n^{wi} = \sum_{m=-\infty}^{\infty} j^{n-m} H_{m-n}^{(2)}(k_1 d_{wi}) \exp[j(m-n)\phi_{wi}] b_m^w, \quad (6.15)$$

$$d_{wi} = \sqrt{(x_{i0} - x_{w0})^2 + (y_{i0} - y_{w0})^2}, \quad (6.16)$$

$$\phi_{wi} = \tan^{-1}\left(\frac{y_{i0} - y_{w0}}{x_{i0} - x_{w0}}\right), \quad (6.17)$$

where the \tan^{-1} function should be defined for $(-\pi, \pi]$.

6.2.3 V_c Field Inside a Cylinder

The fields transmitted inside a dielectric cylinder i in the first medium can be represented by cylindrical waves:

$$V_c^i(\rho_i, \theta_i) = \sum_{n=-\infty}^{\infty} j^{-n} J_n(k_i \rho_i) \exp(jn\theta_i) d_n^i, \quad (6.18)$$

where d_n^i are the unknown coefficients. The wavenumber inside a cylinder i is $k_i = \omega \sqrt{\epsilon_i \mu_0}$.

6.2.4 V_r Reflection from Planar Interface

The scattered field from each cylinder (6.13) will travel to the planar interface where it will partially reflect and partially transmit. The reflection is considered first. Transforming the cylindrical waves into plane-waves using the Sommerfeld integral [49, 98] yields

$$H_n^{(2)}(k_1 \rho_w) \exp(jn\theta_w) = \frac{j^n}{\pi} \int_{-\infty}^{\infty} \frac{\exp[jn \sin^{-1}(\frac{k_y}{k_1}) - jx_w k_{x1} - jy_w k_y]}{k_{x1}} dk_y. \quad (6.19)$$

If this wave (6.19) is propagated to the planar interface, reflected, and then propagated to another cylinder i in the first medium, it becomes

$$RW_n^w = \frac{j^n}{\pi} \cdot \int_{-\infty}^{\infty} \frac{R(k_y)}{k_{x1}} \exp[jn \sin^{-1}(\frac{k_y}{k_1})] \cdot \exp[jk_{x1}(x_i + x_{i0} + x_{w0}) - jk_y(y_i + y_{i0} - y_{w0})] dk_y. \quad (6.20)$$

We now substitute the reflected wave representation (6.20) into the scattered field representation (6.13), and apply the Jacobi-Anger expansion to convert

it into a new sum of cylindrical waves. This produces the reflection of the scattered field from a cylinder w in the coordinates of a cylinder i :

$$V_r^w(\rho_i, \theta_i) = \sum_{n=-\infty}^{\infty} j^{-n} J_n(k_1 \rho_i) \exp(jn\theta_i) D_n^{wi}, \quad (6.21)$$

$$D_n^{wi} = \frac{(-1)^n}{\pi} \sum_{m=-\infty}^{\infty} b_m^w \int_{-\infty}^{\infty} \frac{R(k_y)}{k_{x1}} \exp[j(m+n) \sin^{-1}(\frac{k_y}{k_1})] \exp[jk_{x1}(x_{i0} + x_{w0}) - jk_y(y_{i0} - y_{w0})] dk_y. \quad (6.22)$$

The plane-wave reflection coefficients $R(k_y)$ were given in Section 6.2.1 (6.4, 6.5). The $1/k_{x1}$ term causes a singularity in the integral in (6.22) at $k_y = k_1$. By substituting a new integration variable $k_y = k_1 \sin(\delta)$, the singularity can be removed and the integral can be evaluated numerically. Much work has been done in developing methods for evaluating similar integrals [50, 51].

6.2.5 V_t Transmission through Planar Interface

Our approach to calculating the transmission of scattered fields through the interface is analogous to Section 6.2.4. The scattered field that emanates from a cylinder u in the second medium will partially transmit through the planar interface and interact with a cylinder i in the first medium. To calculate this interaction, we need to first consider the scattered fields of a cylinder u in the second medium:

$$V_s^u(\rho_u, \theta_u) = \sum_{n=-\infty}^{\infty} j^{-n} H_n^{(2)}(k_2 \rho_u) \exp(jn\theta_u) b_n^u. \quad (6.23)$$

Transforming the cylindrical waves into plane-waves using the Sommerfeld integral yields

$$H_n^{(2)}(k_2 \rho_u) \exp(jn\theta_u) = \frac{j^n}{\pi} \int_{-\infty}^{\infty} \frac{\exp[jn \sin^{-1}(\frac{k_y}{k_2}) - jx_u k_{x2} - jy_u k_y]}{k_{x2}} dk_y, \quad (6.24)$$

which is similar to (6.19). If this wave (6.24) is propagated to the planar interface, transmitted through, and then propagated to a cylinder i in the first medium, it becomes

$$TW_n^u = \frac{j^n}{\pi} \int_{-\infty}^{\infty} \frac{T(k_y)}{k_{x2}} \exp[jn \sin^{-1}(\frac{k_y}{k_2}) - jk_{x2}x_{u0}] \cdot \exp[jk_{x1}(x_i + x_{i0}) + jk_y(y_i + y_{i0} - y_{u0})] dk_y. \quad (6.25)$$

We now substitute the transmitted wave representation (6.25) into the scattered field representation (6.23), and apply the Jacobi Anger expansion to convert it into a new sum of cylindrical waves. This produces the transmission of the scattered field from a cylinder u in the coordinates of a cylinder i :

$$V_i^u(\rho_i, \theta_i) = \sum_{n=-\infty}^{\infty} j^{-n} J_n(k_1 \rho_i) \exp(jn\theta_i) S_n^{ui}, \quad (6.26)$$

$$S_n^{ui} = \frac{(-1)^n}{\pi} \sum_{m=-\infty}^{\infty} b_m^u \int_{-\infty}^{\infty} \frac{T(k_y)}{k_{x2}} \exp[jm \sin^{-1}(\frac{k_y}{k_2}) - jn \sin^{-1}(\frac{k_y}{k_1})] \cdot \exp[-jk_{x2}x_{u0} + jk_{x1}x_{i0} + jk_y(y_{i0} - y_{u0})] dk_y. \quad (6.27)$$

The plane-wave transmission coefficients $T(k_y)$, for a wave transmitting from the second medium to the first, can be found by switching the 1 and 2 indices of (6.6) and (6.7). Although it appears that the $1/k_{x2}$ term would cause a singularity in the integral in (6.27), the coefficients $T(k_y)$ always contain a k_{x2} term in the numerator to cancel it out. When numerically evaluating (6.27), we can exploit the inversion symmetry property: $s_{m,n}^{ui} = s_{-n,-m}^{iu}$ for TM

polarization and $s_{m,n}^{ui} = \frac{\epsilon_1}{\epsilon_2} s_{-n,-m}^{iu}$ for TE polarization, where the s coefficients are defined by

$$S_n^{ui} = \sum_{m=-\infty}^{\infty} b_m^u \cdot s_{m,n}^{ui}. \quad (6.28)$$

6.2.6 Applying the Cylinders' Boundary Conditions

The electromagnetic boundary conditions require that the tangential components of the electric and magnetic fields must be continuous across the boundaries of the cylinders and of the planar interface separating the two half-spaces. The boundary conditions for the planar interface have already been satisfied by applying the appropriate reflection (6.4, 6.5) and transmission (6.6, 6.7) coefficients.

We will first consider the boundary conditions for cylinders on one side of the planar interface, and later consider the other side. For both polarizations, at the surface of a cylinder i ($\rho_i = r_i$), the first boundary condition is

$$V_p + \sum_w V_s^w + \sum_w V_r^w + \sum_u V_t^u = V_c^i. \quad (6.29)$$

For the TM case, the magnetic boundary condition is

$$\frac{\partial}{\partial \rho_i} [V_p + \sum_w V_s^w + \sum_w V_r^w + \sum_u V_t^u] = \frac{\partial}{\partial \rho_i} V_c^i, \quad (6.30)$$

and for the TE case, the electric boundary condition is

$$\frac{1}{\epsilon_1} \frac{\partial}{\partial \rho_i} [V_p + \sum_w V_s^w + \sum_w V_r^w + \sum_u V_t^u] = \frac{1}{\epsilon_i} \frac{\partial}{\partial \rho_i} V_c^i. \quad (6.31)$$

The sums \sum_w are over all cylinders in the first medium including cylinder i . The sums \sum_u are over all cylinders in the second medium.

Solving the set of two equations: (6.29) with (6.30) or (6.29) with (6.31),

for the scattering coefficients yields

$$b_n^i = f_n^i [A_n^i + Q_n^i + \sum_{w \neq i} B_n^{wi} + \sum_w D_n^{wi} + \sum_u S_n^{ui}], \quad (6.32)$$

where f_n^i are the single scattering coefficients for dielectric cylinders, similar to Chapter 4. For TM polarization the single scattering coefficients are

$$f_n^i = \frac{J_n(k_i r_i) J_n'(k_1 r_i) - \sqrt{\frac{\epsilon_i}{\epsilon_1}} J_n(k_1 r_i) J_n'(k_i r_i)}{\sqrt{\frac{\epsilon_i}{\epsilon_1}} J_n'(k_i r_i) H_n^{(2)}(k_1 r_i) - H_n^{(2)'}(k_1 r_i) J_n(k_i r_i)}, \quad (6.33)$$

and for TE polarization they are

$$f_n^i = \frac{\sqrt{\frac{\epsilon_i}{\epsilon_1}} J_n(k_i r_i) J_n'(k_1 r_i) - J_n(k_1 r_i) J_n'(k_i r_i)}{J_n'(k_i r_i) H_n^{(2)}(k_1 r_i) - \sqrt{\frac{\epsilon_i}{\epsilon_1}} H_n^{(2)'}(k_1 r_i) J_n(k_i r_i)}, \quad (6.34)$$

where the primes denote a derivative with respect to the function's argument.

If we perform the same analysis from the perspective of the second medium, we obtain

$$b_n^u = f_n^u [P_n^u + \sum_{v \neq u} B_n^{vu} + \sum_v D_n^{vu} + \sum_i S_n^{iu}]. \quad (6.35)$$

The principal waves switch from the incident wave A_n^i and its reflection from the planar interface Q_n^i , to its transmission through the interface P_n^u . The single scattering coefficients f_n^u are for cylinders in the second medium, so we need to switch the background wavenumber $k_1 \rightarrow k_2$ and permittivity $\epsilon_1 \rightarrow \epsilon_2$ in (6.33) and (6.34).

The scattering equations on each side of the dielectric half-space (6.32, 6.35) are linked through the transmission coefficients S_n , which depend on the scattering coefficients b_n from the opposite side. We can re-write (6.32) and (6.35) in matrix form respectively:

$$\vec{L1} = \mathbf{F1}[\vec{A1} + \mathbf{G1}\vec{L1} + \mathbf{D1}\vec{L1} + \mathbf{S1}\vec{L2}], \quad (6.36)$$

$$\vec{L}2 = \mathbf{F}2[\vec{A}2 + \mathbf{G}2\vec{L}2 + \mathbf{D}2\vec{L}2 + \mathbf{S}2\vec{L}1]. \quad (6.37)$$

The vectors \vec{L} contain the cylinders' scattering coefficients b_n . The vectors \vec{A} contain the appropriate principal waves: $A_n^i + Q_n^i$ for the first medium and P_n^u for the second medium. The matrices \mathbf{G} represent the direct interaction between cylinders in the same half-space, and the elements come from (6.15). The matrices \mathbf{D} represent the reflection of the cylinders' scattered fields from the planar interface, and the elements come from (6.22). The matrices \mathbf{S} represent the transmission of the cylinders' scattered fields from one half-space to the other, and the elements come from (6.27).

To combine the two matrix systems (6.36, 6.37), we define

$$\vec{L} = \begin{bmatrix} \vec{L}1 \\ \vec{L}2 \end{bmatrix}, \quad (6.38)$$

$$\vec{A} = \begin{bmatrix} \vec{A}1 \\ \vec{A}2 \end{bmatrix}, \quad (6.39)$$

$$\mathbf{F} = \begin{bmatrix} \mathbf{F}1 & \mathbf{0} \\ \mathbf{0} & \mathbf{F}2 \end{bmatrix}, \quad (6.40)$$

$$\mathbf{G} = \begin{bmatrix} \mathbf{G}1 & \mathbf{0} \\ \mathbf{0} & \mathbf{G}2 \end{bmatrix}, \quad (6.41)$$

$$\mathbf{D} = \begin{bmatrix} \mathbf{D}1 & \mathbf{0} \\ \mathbf{0} & \mathbf{D}2 \end{bmatrix}, \quad (6.42)$$

$$\mathbf{S} = \begin{bmatrix} \mathbf{0} & \mathbf{S}1 \\ \mathbf{S}2 & \mathbf{0} \end{bmatrix}. \quad (6.43)$$

The full multiple scattering solution can now be described by

$$\vec{L} = \mathbf{F}[\vec{A} + \mathbf{G}\vec{L} + \mathbf{D}\vec{L} + \mathbf{S}\vec{L}], \quad (6.44)$$

which can be solved by truncating the cylindrical wave modes m and n to finite limits and inverting

$$\vec{L} = [\mathbf{F}^{-1} - \mathbf{G} - \mathbf{D} - \mathbf{S}]^{-1}\vec{A}. \quad (6.45)$$

Criteria for selecting appropriate limits when truncating the cylindrical wave modes was provided in Chapter 3. These limits depend on the radius of the cylinders compared to the appropriate half-space wavelength.

6.2.7 Stationary Phase Approximation

In order to obtain the D_n and S_n coefficients, it is necessary to apply numerical integration to (6.22) and (6.27) respectively. The numerical integration can become difficult when the separation distances become large or the mode numbers m and n become large, causing the integrand to oscillate rapidly. However, for these cases we can apply the method of stationary phase to evaluate the integrals [104, 105]. The rapidly oscillating integrands in (6.22) or (6.27) will cause most of the integration path along k_y to yield negligible results. The only significant integrand contribution to the integrals comes from the neighbourhood of the stationary point, determined by setting the derivative of the argument of the exponential to zero. For the reflection integral (6.22), the argument is

$$f(k_y) = (m + n) \sin^{-1}\left(\frac{k_y}{k_1}\right) + k_{x1}(x_{i0} + x_{w0}) - k_y(y_{i0} - y_{w0}), \quad (6.46)$$

and for the transmission integral (6.27), the argument is

$$g(k_y) = -n \sin^{-1}\left(\frac{k_y}{k_1}\right) + m \sin^{-1}\left(\frac{k_y}{k_2}\right) + k_{x1}x_{i0} - k_{x2}x_{u0} - k_y(y_{u0} - y_{i0}). \quad (6.47)$$

The derivatives are

$$\frac{df(k_y)}{dk_y} = \frac{(m+n)}{k_{x1}} - (x_{i0} + x_{u0})\frac{k_y}{k_{x1}} - y_{i0} + y_{u0}, \quad (6.48)$$

and

$$\frac{dg(k_y)}{dk_y} = \frac{-n}{k_{x1}} + \frac{m}{k_{x2}} - x_{i0}\frac{k_y}{k_{x1}} + x_{u0}\frac{k_y}{k_{x2}} - y_{u0} + y_{i0}, \quad (6.49)$$

respectively. When the derivatives are set to zero it is only possible to find implicit solutions for k_y . From (6.48) we obtain

$$k_y = \frac{m+n + (y_{u0} - y_{i0})k_{x1}}{x_{i0} + x_{u0}}, \quad (6.50)$$

and from (6.49) we obtain

$$k_y = \frac{\frac{-m}{k_{x2}} + \frac{n}{k_{x1}} - y_{i0} + y_{u0}}{\frac{x_{u0}}{k_{x2}} - \frac{x_{i0}}{k_{x1}}}. \quad (6.51)$$

where k_{x1} and k_{x2} are dependent on k_y . For the implicit equations (6.50) and (6.51), we apply Newton's Method to solve for the stationary phase point $k_y = k_{ys}$. At the stationary point k_{ys} , the x components of the wave-vector in the first and second mediums are k_{x1s} and k_{x2s} respectively. In both the reflection and transmission cases, there will be a unique stationary point k_{ys} for each cylinder pair, and each of the mode numbers m and n .

Now we Taylor-expand the square root and arc-sin functions from (6.22)

and (6.27) about the stationary phase point k_{ys} :

$$k_{x1} = \sqrt{k_1^2 - k_y^2} \approx k_y^2 \left(\frac{-1}{2} \right) \left(\frac{1}{k_{x1s}} + \frac{k_{ys}^2}{k_{x1s}^3} \right) + k_y \left(\frac{k_{ys}^3}{k_{x1s}^3} \right) + k_{x1s} + \frac{k_{ys}^2}{2k_{x1s}} - \frac{k_{ys}^4}{2k_{x1s}^3}, \quad (6.52)$$

$$\sin^{-1}(k_y/k_1) \approx k_y^2 \left(\frac{k_{ys}}{2k_{x1s}^3} \right) + k_y \left(\frac{1}{k_{x1s}} - \frac{k_{ys}^2}{k_{x1s}^3} \right) + \sin^{-1} \left(\frac{k_{ys}}{k_1} \right) - \frac{k_{ys}}{k_{x1s}} + \frac{k_{ys}^3}{2k_{x1s}^3}, \quad (6.53)$$

The Taylor expansions for k_{x2} and $\sin^{-1}(k_y/k_2)$ are similar to (6.52) and (6.53) respectively. The functions $R(k_y)/k_{x1}$ and $T(k_y)/k_{x2}$ are approximated by the constants $R(k_{ys})/k_{x1s}$ and $T(k_{ys})/k_{x2s}$ respectively. With these approximations, the reflection integral in (6.22) can be evaluated to yield

$$D_n^{wi} \approx \frac{(-1)^n}{\sqrt{\pi}} \sum_{m=-\infty}^{\infty} b_m^w \frac{R(k_{ys})}{k_{x1s} \sqrt{a}} \exp\left(\frac{b^2}{4a} - c\right), \quad (6.54)$$

$$a = -j(m+n) \frac{k_{ys}}{2k_{x1s}^3} + j \frac{(x_{w0} + x_{i0})}{2} \left(\frac{1}{k_{x1s}} + \frac{k_{ys}^2}{k_{x1s}^3} \right), \quad (6.55)$$

$$b = j(m+n) \left(\frac{k_{ys}^2}{k_{x1s}^3} - \frac{1}{k_{x1s}} \right) - j(x_{w0} + x_{i0}) \frac{k_{ys}^3}{k_{x1s}^3} + j(y_{i0} - y_{w0}), \quad (6.56)$$

$$c = -j(m+n) \left[\sin^{-1} \left(\frac{k_{ys}}{k_1} \right) - \frac{k_{ys}}{k_{x1s}} + \frac{k_{ys}^3}{2k_{x1s}^3} \right] - j(x_{w0} + x_{i0}) \left(k_{x1s} + \frac{k_{ys}^2}{2k_{x1s}} - \frac{k_{ys}^4}{2k_{x1s}^3} \right), \quad (6.57)$$

and the transmission integral in (6.27) can be evaluated to yield

$$S_n^{ui} \approx \frac{(-1)^n}{\sqrt{\pi}} \sum_{m=-\infty}^{\infty} b_m^u \frac{T(k_{ys})}{k_{x2s} \sqrt{a}} \exp\left(\frac{b^2}{4a} - c\right), \quad (6.58)$$

$$a = -jm \frac{k_{ys}}{2k_{x2s}^3} + jn \frac{k_{ys}}{2k_{x1s}^3} - j \frac{x_{u0}}{2} \left(\frac{1}{k_{x2s}} + \frac{k_{ys}^2}{k_{x2s}^3} \right) + j \frac{x_{i0}}{2} \left(\frac{1}{k_{x1s}} + \frac{k_{ys}^2}{k_{x1s}^3} \right), \quad (6.59)$$

$$b = -jm\left(\frac{1}{k_{x2s}} - \frac{k_{ys}^2}{k_{x2s}^3}\right) + jn\left(\frac{1}{k_{x1s}} - \frac{k_{ys}^2}{k_{x1s}^3}\right) + jx_{u0}\frac{k_{ys}^3}{k_{x2s}^3} - jx_{i0}\frac{k_{ys}^3}{k_{x1s}^3} + j(y_{u0} - y_{i0}), \quad (6.60)$$

$$c = -jm\left[\sin^{-1}\left(\frac{k_{ys}}{k_2}\right) - \frac{k_{ys}}{k_{x2s}} + \frac{k_{ys}^3}{2k_{x2s}^3}\right] + jn\left[\sin^{-1}\left(\frac{k_{ys}}{k_1}\right) - \frac{k_{ys}}{k_{x1s}} + \frac{k_{ys}^3}{2k_{x1s}^3}\right] \\ + jx_{u0}\left(k_{x2s} + \frac{k_{ys}^2}{2k_{x2s}} - \frac{k_{ys}^4}{2k_{x2s}^3}\right) - jx_{i0}\left(k_{x1s} + \frac{k_{ys}^2}{2k_{x1s}} - \frac{k_{ys}^4}{2k_{x1s}^3}\right).$$

In the numerical simulations we investigate the accuracy of these approximations for various cylinder sizes and separation distances.

6.3 Numerical Simulations

To verify the accuracy of the presented method, the first simulation is compared to the finite element method. For this simulation, the stationary phase approximations will not be used. The finite element method is implemented using the commercial software Comsol Multiphysics [®]. The setup for the simulations is shown in Figure 6.3. For the finite element method, the domain was truncated to a 60m×60m square with a 2m embedded perfectly matched layer (PML). Due to the infinite extent of both the plane-wave and the planar interface, it is very hard to obtain accurate results inside a truncated domain. The absorption of the extent of the plane-wave by the PML causes significant distortions in both the incident and scattered fields. Therefore, it is necessary to use a spatially limited incident field, such as a Gaussian beam, to properly compare the two methods. How to incorporate a Gaussian beam or an arbitrary beam into cylindrical scattering was provided in Chapters 2 and 4 respectively. The Gaussian beam used in the simulation is TM polarized with a wavelength of 4*m*. The absolute value of the electric field across the planar interface, shown in Figure 6.4, demonstrates that the two methods produce visually identical results. The L^1 norm error between

the two methods was only 1.57%.

Thesis Addendum to Section 6.3: The convergence of the finite element method is described in Appendix C.

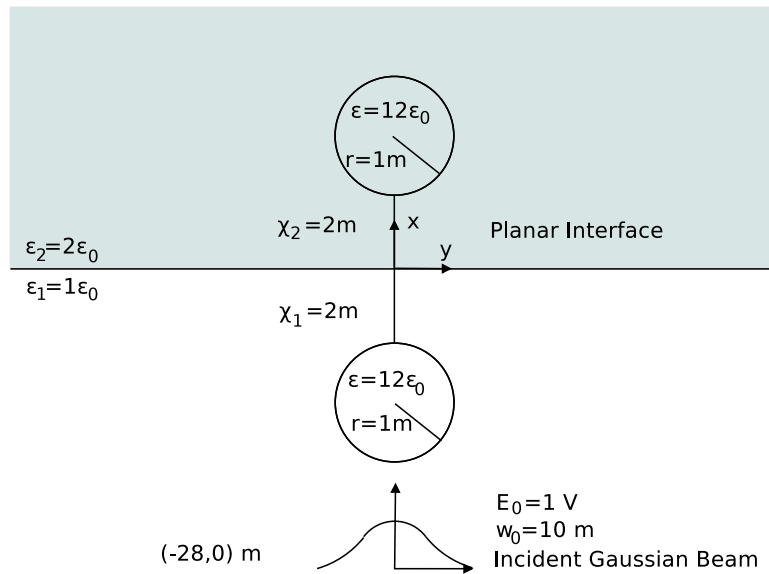


Figure 6.3: The scattering setup for comparing the presented method with the finite element method is shown.

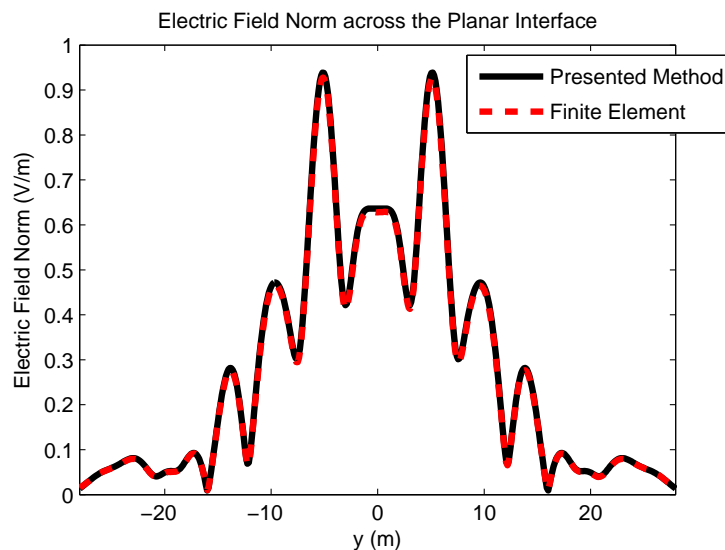


Figure 6.4: The electric field norm across the planar interface is shown for both the presented method and the finite element method. The two methods produce similar results.

The advantages of our analytical-numerical approach over purely numerical methods include:

- Unlimited domain of computation
- Unlimited spatial frequency compatibility for evanescent waves
- Efficient calculation of scattering from small cylinders
- Compact representation in terms of scattering coefficients
- Multiple scattering interactions are addressed in separate matrices

Now the approximations for the reflection (6.54) and transmission (6.58) of cylindrical waves will be compared to their numerical integral counterparts: (6.22) and (6.27) respectively. Our aim is to gauge the accuracy of the approximations for various positions of the cylinders with respect to the planar interface. In our simulations we consider the error in the matrices

$\mathbf{D1}$, $\mathbf{D2}$, $\mathbf{S1}$, and $\mathbf{S2}$, and in the resulting scattering coefficients \vec{L} . Because of the symmetry between $\mathbf{S1}$ and $\mathbf{S2}$, they always share the same error. The percentage errors are given by the L^1 norm of the difference between the matrix computed using the stationary phase approximation and the matrix computed using numerical integration, divided by the L^1 norm of the matrix computed using numerical integration. For example, for the $\mathbf{D1}$ matrix, the percentage error would be calculated

$$Error = 100 * \frac{|\mathbf{D1}_{int} - \mathbf{D1}_{app}|_1}{|\mathbf{D1}_{int}|_1} \% \quad (6.61)$$

All the simulations shown are for TM polarization, where the electric field is in the z direction. The TE polarization case has also been simulated and found to produce similar conclusions.

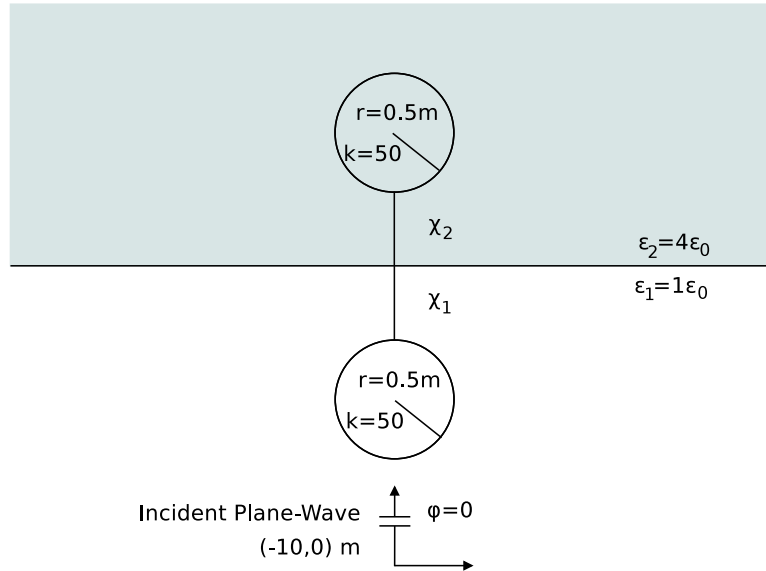


Figure 6.5: The scattering setup for two cylinders being moved away from the interface is shown.

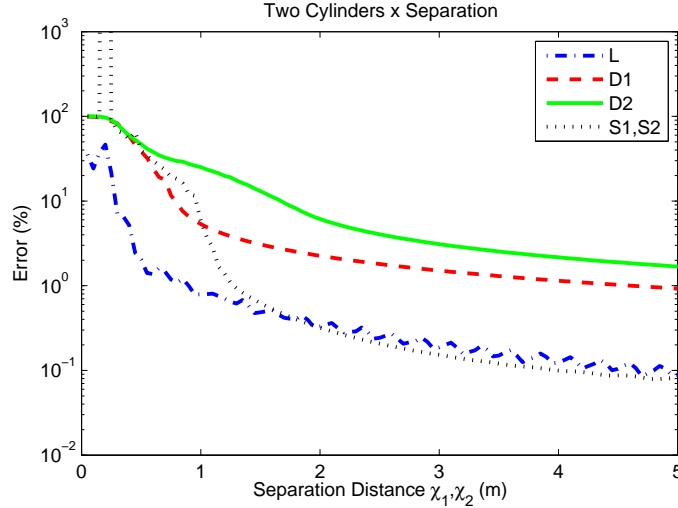


Figure 6.6: The error for the approximate matrices and the scattering coefficients is given for the case when both cylinders are moved away from the interface.

Two simulations will be performed using the setup of Figure 6.5. The incident plane-wave approaches normal to the planar interface $\phi = 0$. The background wavelength in medium one has been normalized to $\lambda = 1m$, and in medium two the wavelength is half $\lambda = 0.5m$. The dielectric cylinders have a radius of $a = 0.5m$ and a wavenumber $k = 50$.

In the first case both cylinders are moved away from the interface. The error is shown in Figure 6.6. As the cylinders are moved away from the interface, all the approximations to the \mathbf{D} and \mathbf{S} matrices converge rapidly. The approximated $\mathbf{D2}$ matrix is less accurate than the $\mathbf{D1}$ matrix because the cylinder in the second medium appears twice as large when compared to the surrounding wavelength. This indicates that the size of the cylinder relative to the wavelength affects the convergence significantly. The large spike in the error for the \mathbf{S} matrices is caused by the stationary points in the approximation becoming complex. However, the stationary points only become complex when the cylinders are very close to each other and the stationary phase approximation is poor regardless. The scattering coefficients

in \vec{L} become accurate to within 1% after the cylinders are moved away by only $\chi_1 = \chi_2 = 1m$.

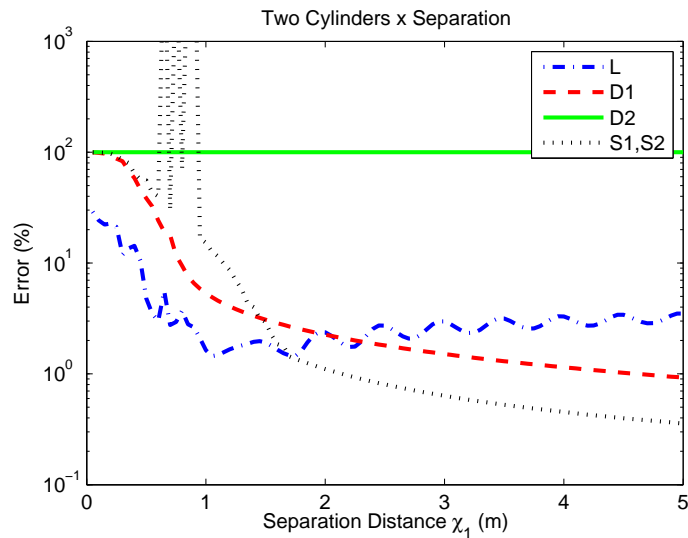


Figure 6.7: The error for the approximate matrices and the scattering coefficients is given for the case when only one cylinder is moved away from the interface.

In the second case one cylinder is left near the interface $\chi_2 = 0.1m$ and the other cylinder is moved away from the interface. The error is shown in Figure 6.7. The **D2** matrix approximation does not converge because the cylinder in the second medium remains at a fixed distance from the planar interface. It is important to note that the approximations to the **S** matrices both converge, even when one cylinder remains close to the interface. However, the scattering coefficients \vec{L} do not converge to accurate results because of the large error produced by the **D2** matrix.

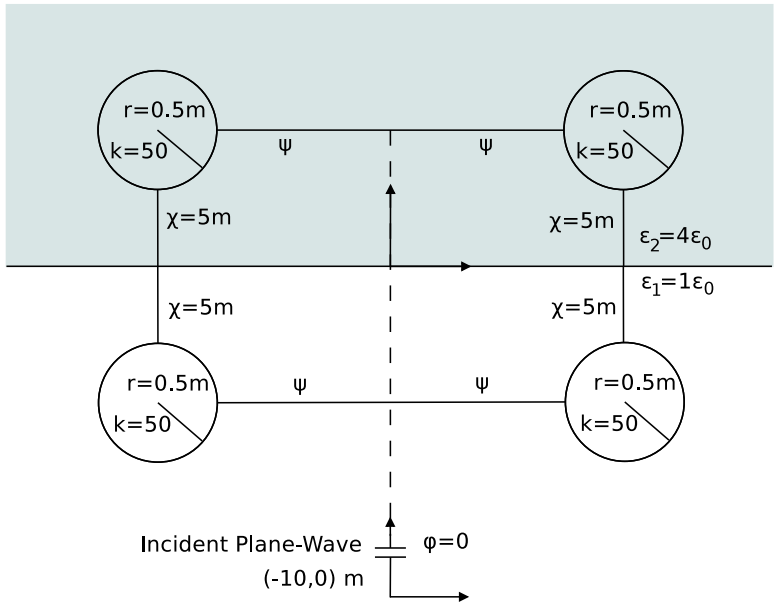


Figure 6.8: The scattering setup for simulations involving four cylinders is shown.

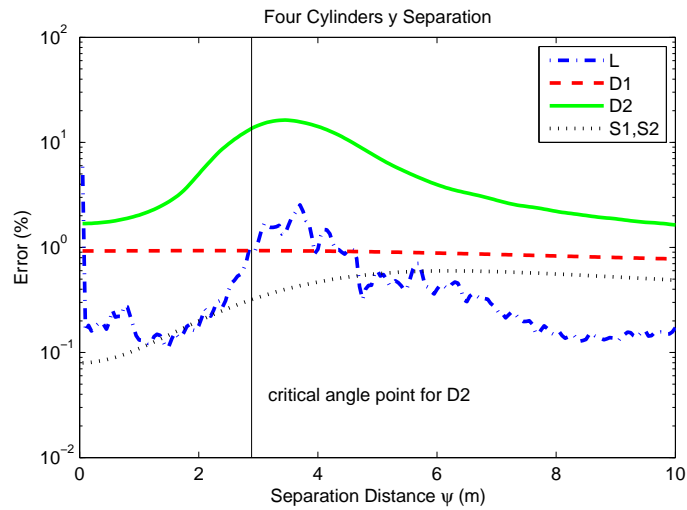


Figure 6.9: The error for the approximate matrices and the scattering coefficients is given for the case when four cylinders are separated from each other in the y direction.

Now we consider the case of four cylinders that are separated from each other in the y direction, as shown in Figure 6.8. The cylinders, background mediums, and incident wave are identical to the previous two simulations. The error plot is shown in Figure 6.9. The matrix **D2** embodies the effect of a wave from a cylinder in the second medium reflecting from the planar interface. When the ray path from one cylinder to another is close to the critical angle of 30° , the error in the approximate **D2** matrix peaks. This may be caused by the sudden changes in the magnitude and phase of the reflections near the critical angle. The matrix **D1** embodies the effect of a wave from a cylinder in the first medium reflecting from the interface. In this case there cannot be critical angle reflections, so the error is not affected strongly by separating the cylinders in the y direction. The **S** matrices embody the effect of cylinders interacting through the interface from opposite sides. The ray path between cylinders on opposite sides of the half-space asymptotically approaches the critical angle but never reaches it. This accounts for the asymptotic increase in the error of the **S** matrices.

As a final example, to demonstrate the advantages of our approximations, we consider the computational speed and accuracy of scattering from cylinders far from the planar interface. The setup in Figure 6.8 is altered to have $\chi = 30m$ and $\psi = 10m$ for the simulation. The incident plane-wave is also moved back to $x_0 = -50m$. Comparing the two methods, the total L^1 norm error (6.61) for the scattering coefficient vector \vec{L} is only 0.017%. However, the computational time for the approximate method is 500 times faster than that of the numerical integration method. The integrals were evaluated with a trapezoidal scheme, and with integration limits truncated inside the evanescent region at $k_y \leq |6\pi|$. The **D** matrices required 7000 integration points and the **S** matrices required 50000 integration points. Numerical integration is clearly not a practical solution for this scattering problem because of the highly oscillatory integrand. In this case our approximation is necessary to produce fast and accurate results.

6.4 Conclusion

An analytical-numerical technique was presented for the scattering from cylinders in two dielectric half-spaces. The accuracy of the presented method was verified by comparing its results to the finite element method. An approximation based on the method of stationary phase was introduced to eliminate the need for numerical integration when the cylinders are sufficiently separated from the planar interface. The stationary point was found to be dependent on the position of the cylinders and the cylindrical wave mode numbers m and n . The numerical simulations demonstrated the convergence of the stationary phase approximation. For the reflection of cylindrical waves (6.22), the approximation converged as the cylinders were separated from the interface. For the transmission of cylindrical waves (6.27), the approximation converged if at least one of the two interacting cylinders was separated from the interface. In both cases, the approximation improved for smaller cylinders and angles of interaction that were close to the normal of the interface. In the case where the cylinders were far from the interface, computing the numerical integrals became difficult due to their oscillating integrand, so the stationary phase approximation became essential. The stationary phase approximation was not valid when the cylinders were near the planar interface. However, computing the numerical integrals was much easier in that case.

Chapter 7

Apertureless Near-Field Scanning Optical Microscopy Simulations

7.1 Introduction

There are many aspects of ANSOM that differentiate it from traditional lens based imaging methods [61]. Traditional images are a refocusing of the scattered fields emanating from the object under consideration, whereas ANSOM images sample the near-field of the object, which contains both the incident and scattered fields. The incident field can be removed by using evanescent wave illumination from underneath, but this method puts restrictions on the thickness and properties of the object [64].

Traditional images are composed of the refocused radiation intensity from the surface of the source or scatterer. In ANSOM images, the field that is sampled contains evanescent waves as well as radiation. The intensity of electromagnetic fields containing evanescent components differs from that of radiative fields alone and needs to be considered carefully. In addition, how the probe samples the near-field will depend strongly on the size and material properties of the probe-tip.

The image resolution is determined primarily by the distance from the probe-tip to the object and by the size of the probe-tip. Evanescent fields of a higher spatial frequency decay faster than those of a lower spatial frequency. Thus, the electromagnetic fields are better defined closer to the surface of the

object. The size of the probe-tip determines the spatial size of the sampling, the signal power, and the multiple scattering effects. A larger tip will sample a larger portion of the near-field at every probe position, leading to a possible reduction in resolution. The scattered power from a smaller probe-tip is reduced, leading to a weaker signal to noise ratio. When the probe-tip is a strong enough scattering body, there is the possibility that its scattered field will interact with the object and distort the image.

ANSOM imaging procedures are often modelled by replacing the vibrating tip with a scattering sphere [63,100]. The size of the sphere is determined by the radius of curvature of the probe-tip. The full shaft of the probe is simulated when shaft effects such as wave coupling or surface plasmons are being investigated [67,100]. Adapting this for two-dimensional scattering, the probe sphere will be modelled by a small cylinder. Using the previously derived scattering models, the objects under consideration can be modelled by other dielectric or metallic cylinders in a homogeneous medium, in front of a half-space, or buried in a dielectric half-space.

To separate the scattered power of the probe-tip from the background scattering, the probe is vibrated normal to the surface of the object. This creates a non-linear modulation of the scattered field from the probe-tip. In our models, this modulation will be simulated by taking several measurements while varying the size of the probe-tip.

7.2 The Reference Images

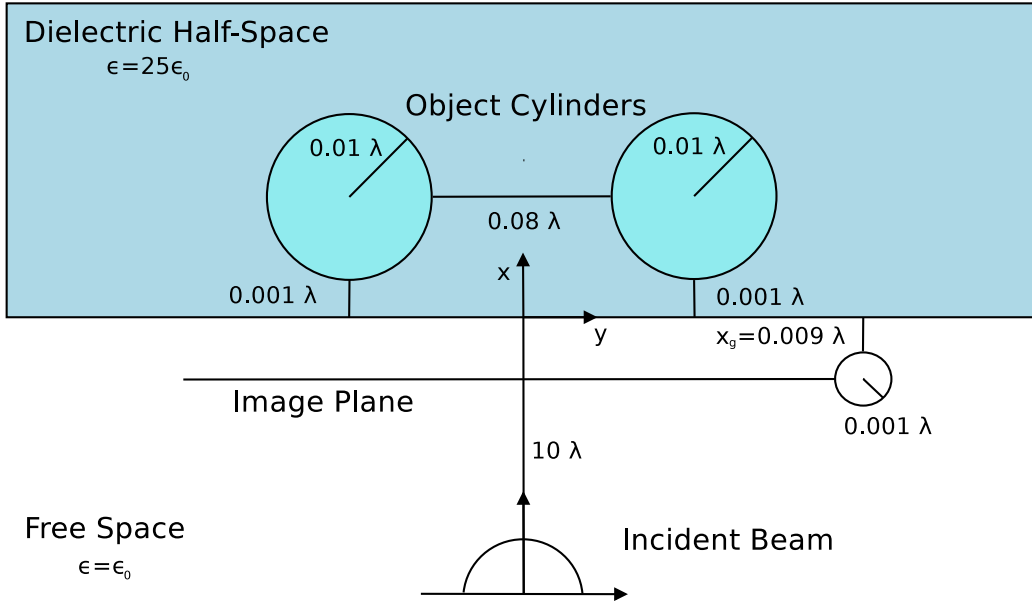


Figure 7.1: The scattering setup for the ANSOM simulations is shown but the dimensions are not to scale. The z direction is normal to the page. The wavelength in free space is λ .

In order to analyze the image collection procedure in ANSOM, we need to first produce reference images for comparison. The setup for the simulations is shown in Figure 7.1. The dimensions are all with respect to the wavelength in free space λ . The incident field is a Gaussian beam with an amplitude of $E_0 = 1 \text{ V/m}$ and a beam waist of $w_0 = 200\lambda$. All of the cylinders are perfect electric conductors (PEC). The probe-tip is modelled by the small cylinder in free space and the object to be analyzed is composed of the two larger cylinders buried in the dielectric half-space.

The probe-tip is scanned across the image plane at a distance of 0.01λ from the planar interface, and the scattered power from the probe-tip is measured. Since ANSOM uses far-field power measurements, the scattered

field from the probe-tip

$$V_s(\rho, \theta) = \sum_{n=-\infty}^{\infty} j^{-n} H_n^{(2)}(k_1 \rho) \exp(jn\theta) b_n, \quad (7.1)$$

needs to be converted into a measure of time averaged intensity S_{av} , in W/m². The time averaged intensity in the far-field is

$$S_{av}(\rho, \theta) = \frac{C|V_s(\rho, \theta)|^2}{2}, \quad (7.2)$$

where $C = 1/\eta$ for TM polarization and $C = \eta$ for TE polarization. The intrinsic impedance of the background medium is $\eta = \sqrt{\frac{\mu}{\epsilon}}$. TM polarization is defined as $V = E_z$ and TE polarization is defined as $V = H_z$. In the far-field, the Hankel function in (7.1) can be approximated by [96]

$$H_n^{(2)}(k_1 \rho) \approx \sqrt{\frac{2}{\pi k_1 \rho}} \exp(-jk_1 \rho + jn\pi/2 + j\pi/4). \quad (7.3)$$

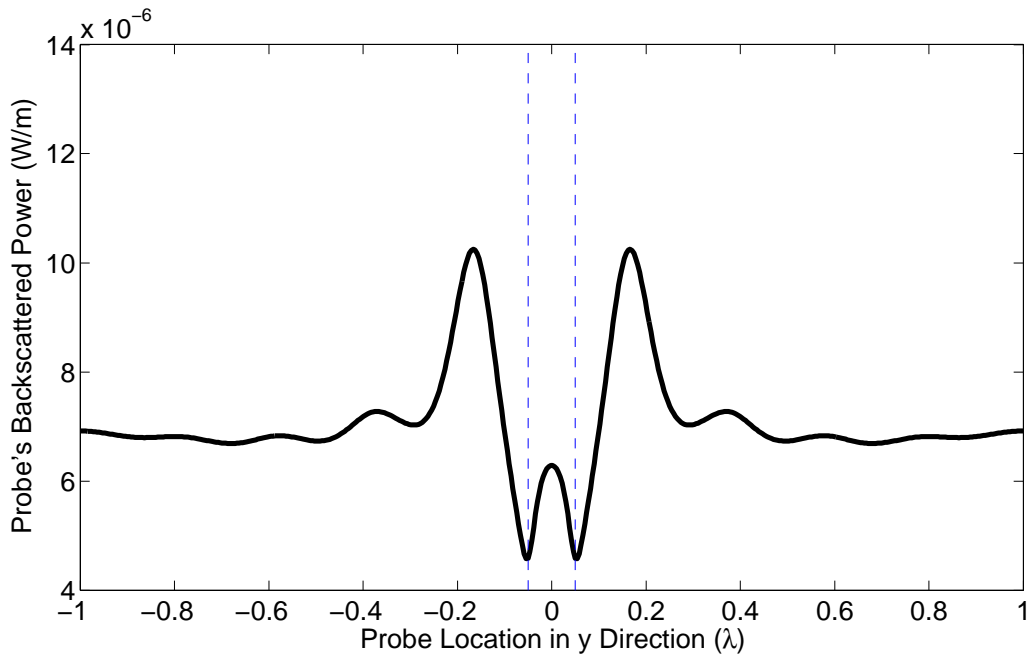
Inserting our far-field approximation (7.3) into the scattered field (7.1) and taking the square magnitude yields

$$|V_s|^2 \approx \frac{2}{\pi k_1 \rho} \left| \sum_{n=-\infty}^{\infty} \exp(jn\theta) b_n \right|^2. \quad (7.4)$$

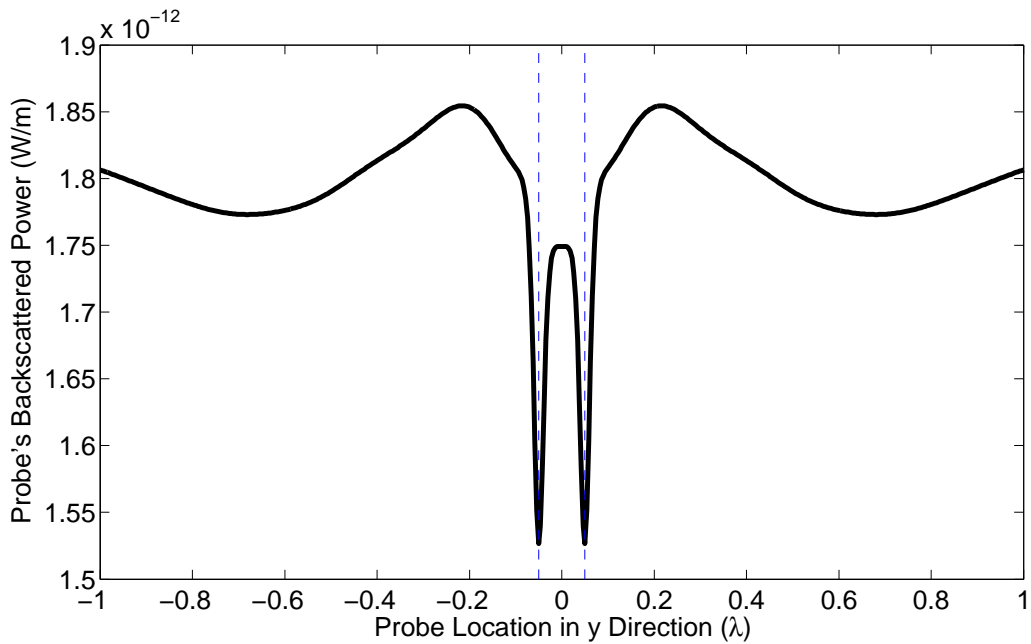
To calculate the total backscattered power, we integrate the time averaged intensity over a semi-circular region

$$\int_{\pi/2}^{3\pi/2} S_{av}(\rho, \theta) \rho d\theta = \frac{C}{\pi k_1} \int_{\pi/2}^{3\pi/2} \left| \sum_{n=-\infty}^{\infty} \exp(jn\theta) b_n \right|^2 d\theta. \quad (7.5)$$

The total backscattered power is measured in W/m, where the per-meter refers to the z dimension.



(a) A simulated ANSOM image is shown for TM illumination.



(b) A simulated ANSOM image is shown for TE illumination.

Figure 7.2: The probe-tip is scanned across the image plane and its scattered power is recorded to create simulated ANSOM images.

The image results for TM polarization are shown in Figure 7.2a and the results for TE polarization are shown in Figure 7.2b. The centres of the object cylinders are indicated with dashed lines. Even though the two object cylinders are spaced $\lambda/10$ apart, their effects are clearly distinguished with subwavelength resolution in each case. However, it is not obvious how to interpret the data contained in either image.

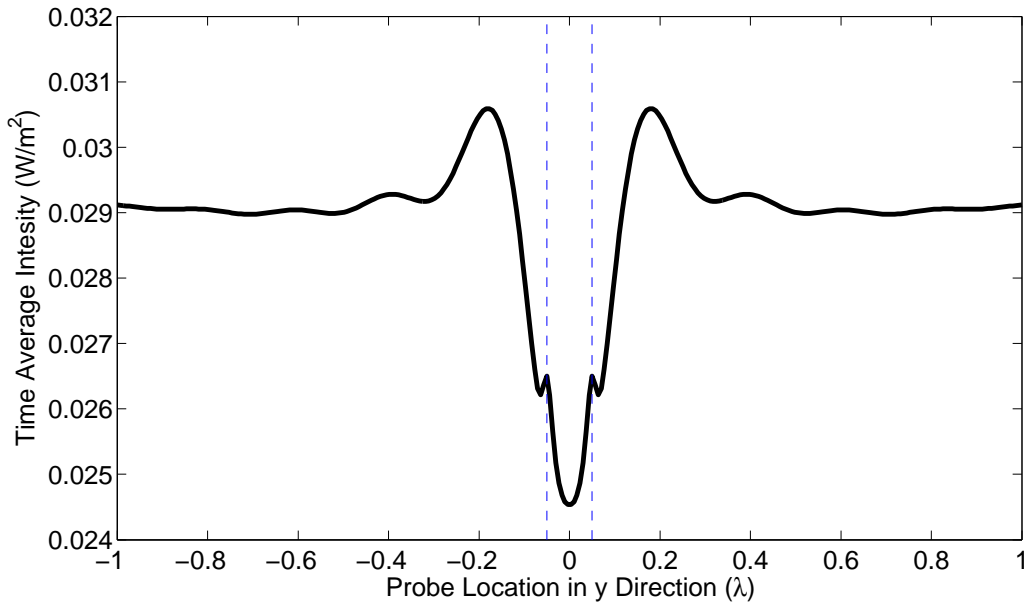
7.3 Interpreting Collected Data

One of the main tasks in ANSOM is to correctly interpret the collected data contained in the images. As shown by Kim and Song [64], the images are not equivalent to a topographical profile of the object, but also contain the effects of the optical properties of the object. Since our object is made up of two cylinders buried in a dielectric half-space, the topological profile would be flat. To find where the ANSOM image data originates, the near-field of the object should be investigated.

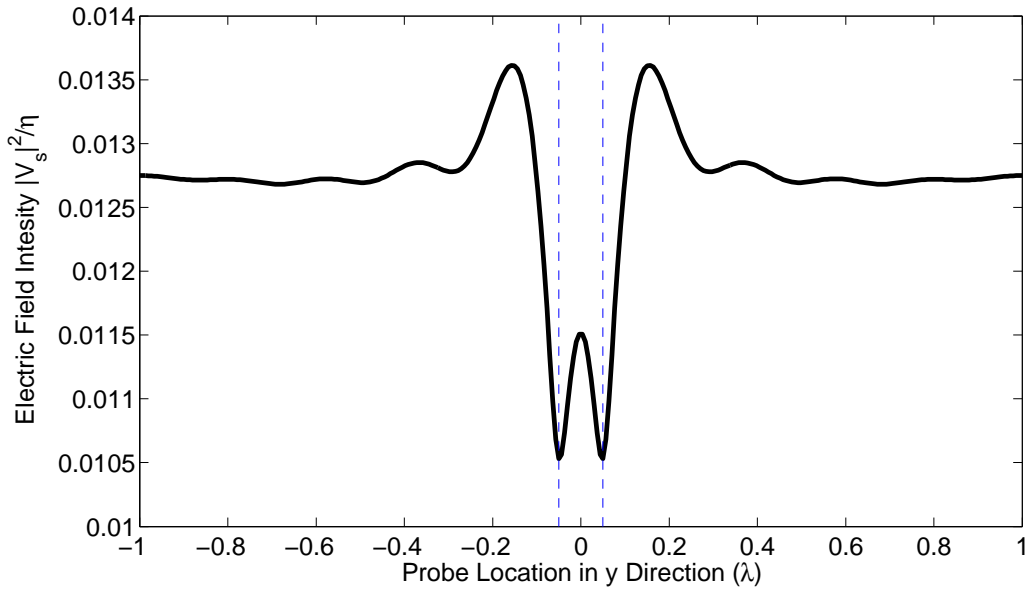
The time averaged electromagnetic field intensity in the near-field of the object is

$$S_{av} = \frac{1}{2} \Re\{\mathbf{E} \times \mathbf{H}^*\}. \quad (7.6)$$

In the presence of evanescent waves, the electromagnetic intensity is no longer proportional to the square magnitude of the electric or magnetic fields $S_{av} = C/2|V_s|^2$. However, we will use $C|V_s|^2$ as a measure of the individual electric/magnetic field intensity to compare the images to, even though it does not represent the electromagnetic field intensity in the near-field.



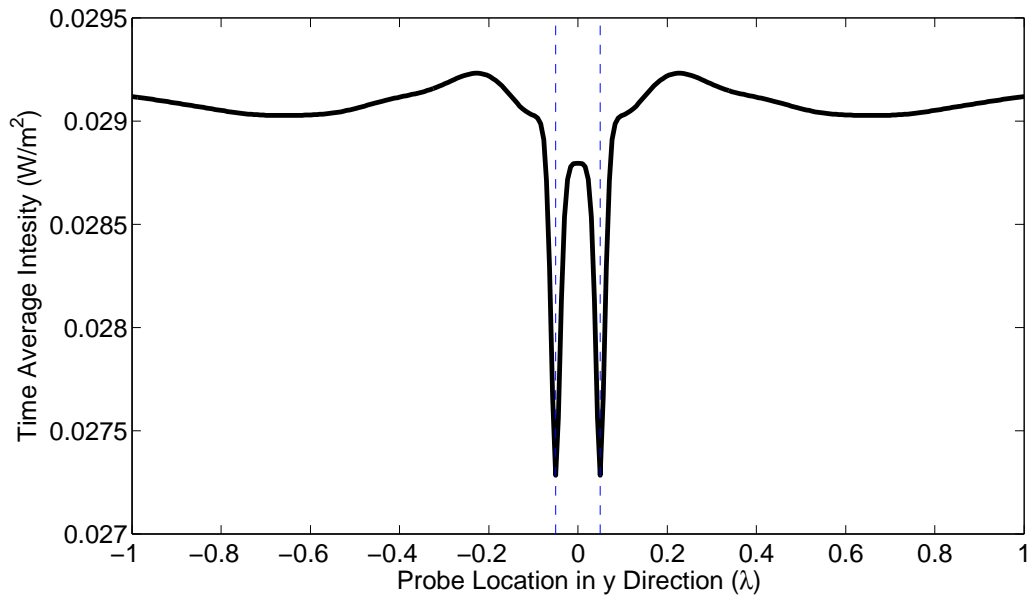
(a) The electromagnetic field intensity is plotted across the image plane.



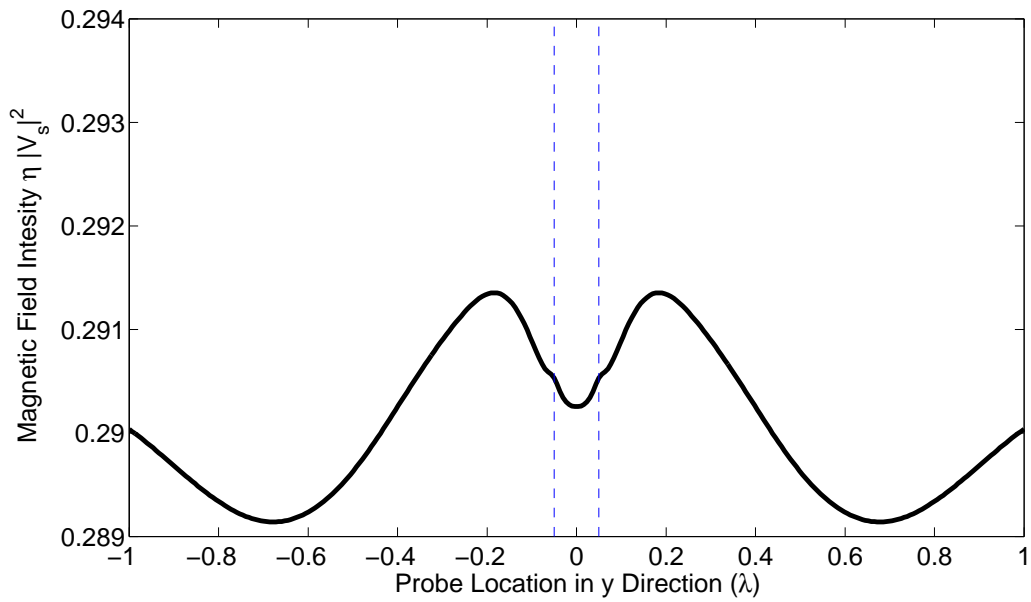
(b) The tangential electric field intensity is plotted across the image plane.

Figure 7.3: The electromagnetic intensity is compared to the electric field intensity across the image plane. TM polarization is used.

First, we will consider the TM polarization case. Figure 7.3a shows the electromagnetic field intensity along the image plane. For comparison, we also provide the intensity of the electric field across the same plane in Figure 7.3b. It is clear from Figure 7.2a that the power scattered by the probe is directly proportional to the electric field intensity but not to the electromagnetic field intensity. This phenomenon can be attributed to the scattering properties of the probe cylinder. Since the cylinder is a perfect electric conductor, the tangential electric field must be zero at the boundary of the cylinder. For TM polarization, the electric field is always completely tangential to the cylinder, causing the scattering coefficients to be proportional to the electric field.



(a) The electromagnetic field intensity is plotted across the image plane.



(b) The tangential magnetic field intensity is plotted across the image plane.

Figure 7.4: The electromagnetic intensity is compared to the magnetic field intensity across the image plane. TE polarization is used.

Now we will consider the TE polarization case. Figure 7.4a shows the electromagnetic field intensity along the image plane. For TE polarization, we also provide the intensity of the magnetic field across the same plane in Figure 7.4b. Unlike the TM polarization case, the image from Figure 7.2b is closely related to the electromagnetic field intensity. We expect that the PEC probe would scatter power proportional to the tangential electric field. However, in the TE polarization case, the tangential electric field is in the $\hat{\theta}$ direction which is dependant upon the position of the cylinder.

7.4 Demodulation

In an actual ANSOM procedure, to recover the scattered power from the probe-tip alone, the probe shaft is modulated in the \hat{x} direction at a frequency Ω . The distance from the probe-tip to the object is given by $x(t) = x_0 + A \cos(\Omega t)$, where x_0 is the midpoint offset and A is the amplitude of oscillation. The total scattered field at a point (x', y') in the far-field is composed of the background scattering $E_b \exp(j\phi_1)$ and the probe-tip scattering $E_p \exp(j\phi_2)$. Both the phase ϕ_2 and amplitude E_p of the scattered field from the probe-tip depend on the phase of the spatial modulation (Ωt). The time dependence of the radiation $\exp(j\omega t)$ has been suppressed. The time-averaged (over the period of the radiation $2\pi/\omega$) scattering intensity at the point (x', y') in the far-field is given by

$$S_{av} = \frac{|E|^2}{2\eta} = \frac{|E_b|^2 + |E_p|^2 + 2E_b E_p \cos(\phi_1 - \phi_2)}{2\eta}. \quad (7.7)$$

The first term $|E_b|^2$ can easily be removed through demodulation because it has no time dependence. The second term $|E_p|^2$ is the power scattered by the probe-tip, which we would like to recover. The third term is the interference between the background scattering and the probe-tip scattering. Homodyne detection can be used to remove this interference signal [69]. A

large reference signal E_r , with a well defined phase ϕ_3 , can be used to override the interference between E_b and E_p with a much larger interference between E_r and E_p . With the addition of the reference signal, the scattered intensity becomes

$$S_{av} = \frac{|E_b|^2 + |E_p|^2 + |E_r|^2 + 2E_bE_p \cos(\phi_1 - \phi_2)}{2\eta} + \frac{2E_bE_r \cos(\phi_1 - \phi_3) + 2E_rE_p \cos(\phi_3 - \phi_2)}{2\eta}. \quad (7.8)$$

After demodulation, all of the constant terms are removed leaving

$$S_{av} = \frac{|E_p|^2 + 2E_bE_p \cos(\phi_1 - \phi_2) + 2E_rE_p \cos(\phi_3 - \phi_2)}{2\eta} \approx \frac{E_rE_p \cos(\phi_3 - \phi_2)}{\eta}. \quad (7.9)$$

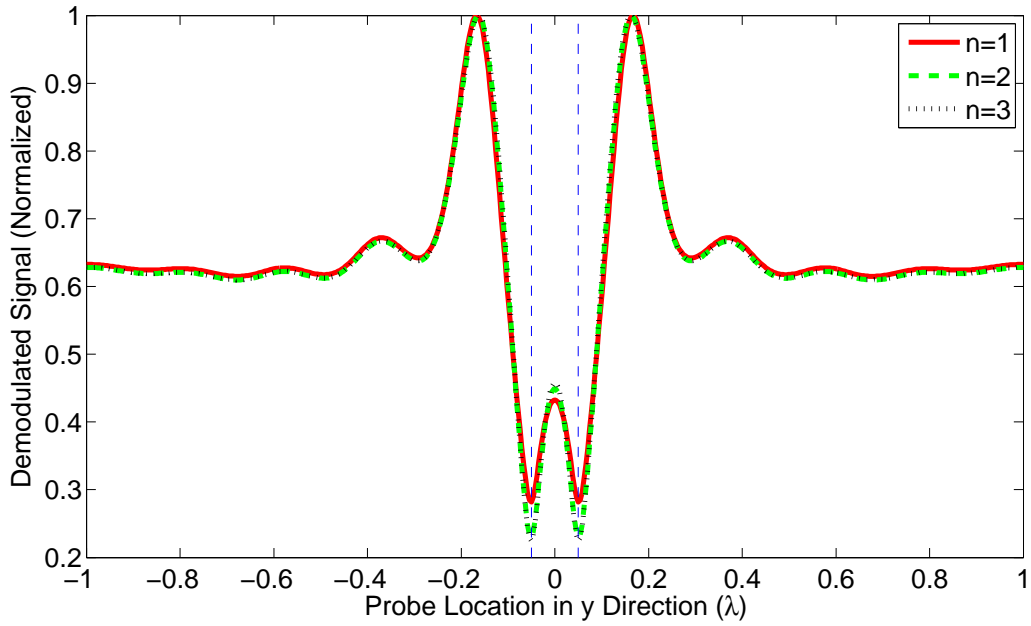
If the amplitude of the reference signal is large compared to the background signal and the probe-tip signal $E_r \gg E_b \gg E_p$, then the last term in (7.9) will dominate. By taking two measurements, one with $\phi_3 = 0$ and one with $\phi_3 = \pi/2$, the magnitude E_p and phase ϕ_2 of the scattered field from the probe-tip can be recovered.

The only difficulty that still remains is how to perform the demodulation. Due to the spatial modulation, the scattered field from the probe-tip will vary in a non-linear way, creating an infinite set of harmonics. Kim and Leone [71] state that the harmonics $n\Omega$ of the scattered field from the probe-tip are approximately equal to the x -coordinate partial derivative of the local field

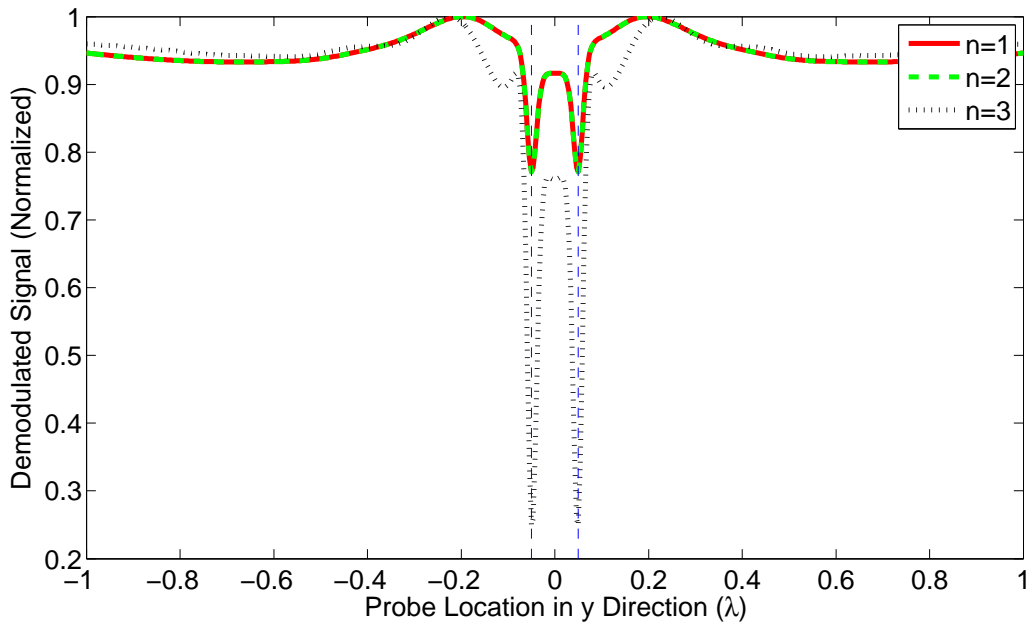
$$E_n(x_0, y) = \frac{1}{2\pi} \int_0^{2\pi} E[f(\phi), y] \exp(jn\phi) d\phi \approx \frac{\partial^n E(x, y)}{\partial x^n} \Big|_{x=x_0}. \quad (7.10)$$

This approximation converges in the limit as the amplitude of modulation A becomes negligibly smaller than the wavelength λ [69]. To reconstruct a two-dimensional map of the near-field, all of the harmonic components of the field would be necessary. It is common for only one harmonic component to be demodulated, and this component is assumed to be proportional to the near-

field $E(x_0, y) \propto E_n(x_0, y)$. This assumption relies on the x coordinate of the near-field being locally separable $E(x, y) = Y(y)X(x)$, so that the derivative of the field (7.10) will be directly proportional to the field profile in the y direction. Knoll and Keilmann [68] demonstrated that higher harmonic demodulation is able to reject the background scattering better, resulting in better image resolution and contrast. However, the scattering signal for higher harmonics decreases in amplitude significantly.



(a) Demodulated ANSOM images are shown for TM polarization.



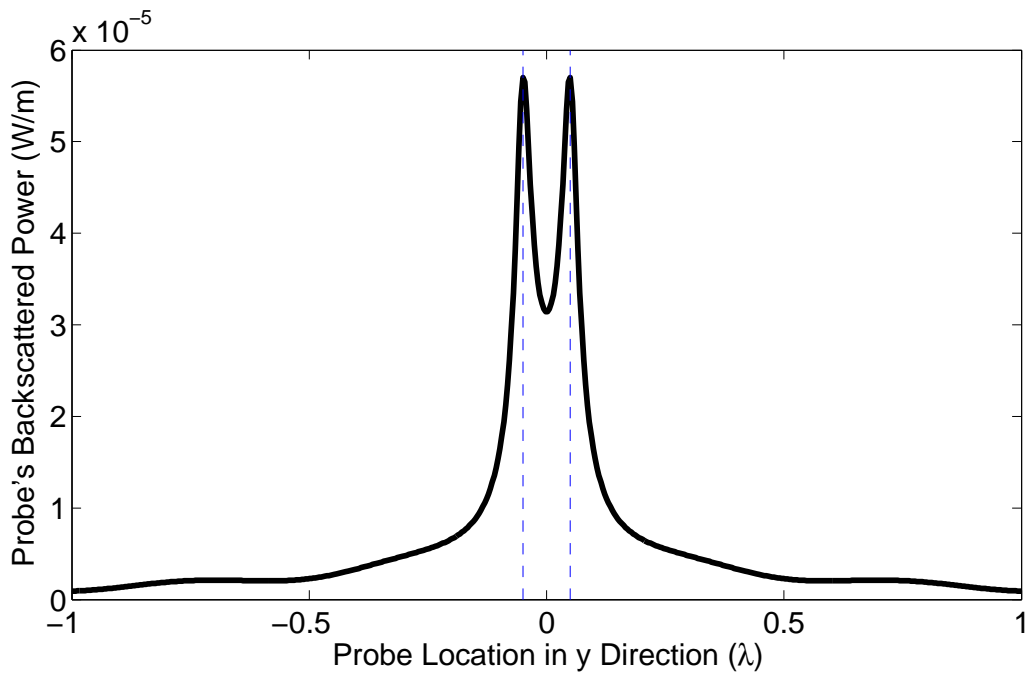
(b) Demodulated ANSOM images are shown for TE polarization.

Figure 7.5: The first, second, and third harmonic signals are demodulated using homodyne detection.

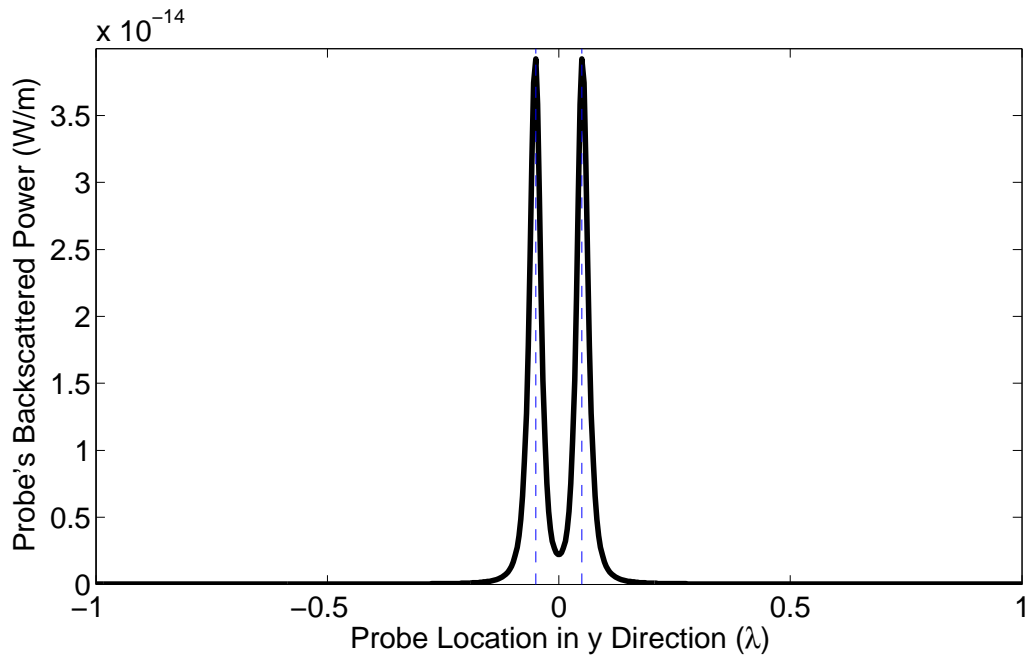
Since our ANSOM model does not include the probe-shaft, we will simulate the modulation by changing the size of the probe-tip. Our probe-tip will modulate from no cylinder at all $a = 0$, to the full sized cylinder $a = 0.001\lambda$. A set of new simulations were created using this modulation scheme with TM and TE polarizations and the setup shown in Figure 7.1. Plots of the first three demodulated harmonics are displayed in Figure 7.5. The demodulated power was measured by taking a discrete spatial derivative of the far-field scattering intensity measurements for different probe-cylinder sizes. The demodulated signal amplitude is proportional to the scattering intensity of the probe-tip but the magnitude is irrelevant. Hence, the magnitudes have all been scaled to a maximum amplitude of one. Comparing the TM harmonic signals from Figure 7.5a with the same image produced directly from the scattered power of the probe-tip in Figure 7.2a, we can see that all three harmonics recover the image well. For TE polarization, the third harmonic from Figure 7.5b provides a better recovery of the scattered power profile from Figure 7.2b. The difference in performance of the two polarizations is due to the difference in the non-linear response of the modulation of the probe cylinder in each case. The rejection of the background signal in the third harmonic demodulation is not observed here, which may be due to not modelling the probe shaft.

7.5 Interference of Waves

One of the major differences between a traditional image and an image formed from a scanning probe method is the interference between the incident field and the scattered field. In a traditional image, a lens is used to refocus the scattered waves back into their original form at the surface of the object. In a scanning probe image, the probe samples the near-field distribution which contains both the incident and scattered fields. The addition of the incident and scattered fields creates an interference pattern.



(a) An altered ANSOM image is shown for TM polarization.



(b) An altered ANSOM image is shown for TE polarization.

Figure 7.6: Altered ANSOM images are shown where the probe-tip samples only the scattered field from the object.

If we do not allow the incident field to scatter from the probe-tip, then the ANSOM images for TM and TE polarizations are shown in Figure 7.6a and Figure 7.6b respectively. Comparing these plots to our original ANSOM images in Figure 7.2a and Figure 7.2b, it is clear that the interference patterns from the addition of the incident field into the image, completely alter the interpretation of the image. In a real ANSOM image, the presence of the object cylinders creates localized dips in the field strength because the scattered field from a PEC cylinder is out of phase with the incident field. In a traditional image, the scattering from a PEC cylinder would appear as a spike in localized field strength because the incident field has been removed.

Comparing the results for the TM (Figure 7.6a) and TE (Figure 7.6b) polarizations, we notice that the resolution of the TE case far surpasses that of the TM case. This may be due to enhanced evanescent field recovery in the TE case. This can be seen by analyzing the electric and magnetic fields of an evanescent wave

$$\mathbf{V} = \exp(-jk_y y - \alpha x) \hat{z}, \quad (7.11)$$

where $V = E_z$ for TM polarization and $V = H_z$ for TE polarization. For an evanescent wave, one component of the wave-vector $\mathbf{k} = (k_x, k_y, 0)$ is imaginary $k_x = -j\sqrt{k_y^2 - k^2} = -j\alpha$, and the other is super-oscillatory $k_y > \omega/c$. The corresponding field in the $x - y$ plane can be calculated from Maxwell's equations. The magnetic field for TM polarization is

$$\mathbf{H} = \frac{V}{\omega\mu} (k_y \hat{x} + j\alpha \hat{y}), \quad (7.12)$$

and the electric field for TE polarization is

$$\mathbf{E} = \frac{V}{\omega\epsilon} (-k_y \hat{x} - j\alpha \hat{y}). \quad (7.13)$$

As the spatial frequency increases above the wavenumber $k_y > \omega/c$, the

fields in the $x - y$ plane grow in magnitude compared to the corresponding \hat{z} directed field \mathbf{V} . In the TM case, the evanescent wave skews towards stronger magnetic fields; in the TE case, the evanescent wave skews towards stronger electric fields. However, when the evanescent wave is converted into radiation through scattering by the probe-tip, the wave impedance of the radiation must return to the intrinsic material impedance. For a PEC probe-tip, the scattering will be proportional to the local electric field. If the polarization is TE, the electric component of the evanescent waves will be stronger, leading to an enhanced conversion of evanescent waves into radiation.

7.6 Tip-Object Interaction

In ANSOM, one of the assumptions is that the probe-tip does not distort the near-field distribution through multiple scattering. If the probe-tip is very small then the scattered fields emanating from it will also be very small. If these small fields are negligible compared to the scattered field from the object, then this approximation will be good.

One benefit of our model in simulating these effects is that the multiple scattering between any cylinders can be removed easily. To determine if tip-object coupling is distorting our image, we need to remove the ability of the probe-tip's scattered field to affect the object cylinders. This can be done easily by removing one of the \mathbf{S} matrices in the simulation.

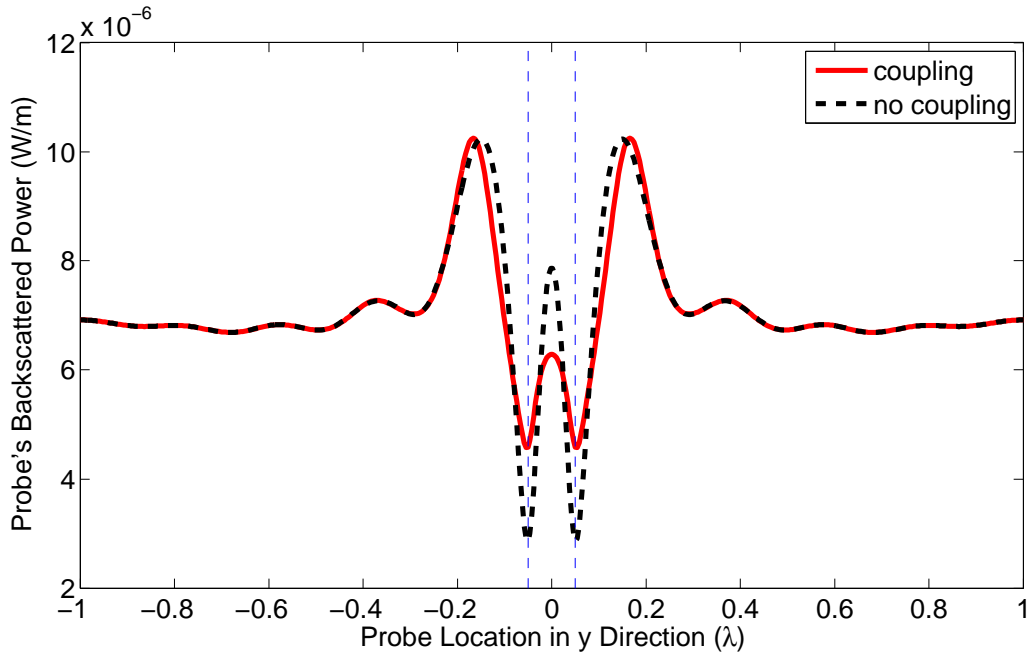


Figure 7.7: The ANSOM images for TM polarization with and without tip-object coupling are shown.

For the TM case, a distortion of the fields due to tip-object interactions can already be observed at a tip radius of $a = 0.001\lambda$. The effects of tip-object coupling are displayed in Figure 7.7. It is clear that the tip-object interactions distort the image from its original field representation. The resolution of the distorted image has been reduced. Ideally, the ANSOM image should follow the distribution of the tangential electric field shown in Figure 7.3b. Reducing the size of the probe-tip will help to reduce the distortion. The drawback is that a smaller probe-tip also reduces the amount of scattered power and consequently, the signal to noise ratio.

7.7 Probe to Object Distance

Evanescent waves with higher spatial frequencies decay faster with distance from their surface of origin. This means that the distance from the probe to the surface of the object will limit the resolution of the image. The closer the probe gets to the surface, the stronger and more clear the evanescent components will be. Ideally, the probe should be brought as close to the surface of the object as possible without touching it.

The setup in Figure 7.1 was simulated using TE polarization with several distances between the half-space and the probe x_g : 0.02λ , 0.05λ , 0.1λ , and 0.5λ . The images produce at each distance are displayed together in Figure 7.8. It is clear that the resolving power of the scanning probe method deteriorates quickly as the probe is separated from the object by only half a wavelength. The change in power level between the different distances is due to the partial standing wave produced by the reflection of the incident beam from the dielectric half-space.

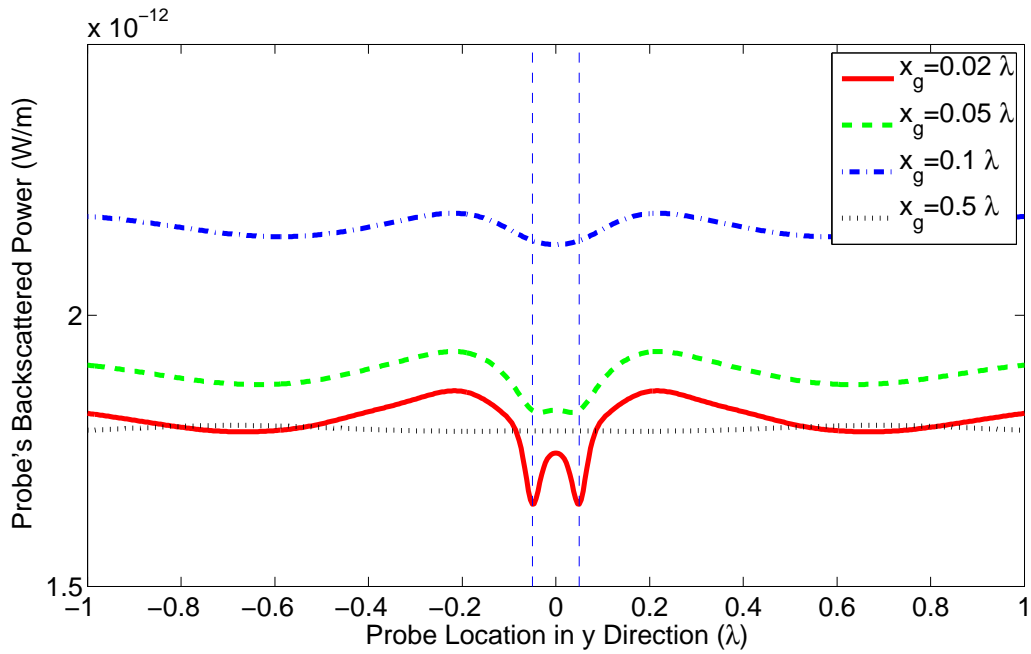


Figure 7.8: ANSOM images are shown for various distances separating the half-space and the probe. TE polarization was used.

7.8 Wavelength and Object Parameters

Finally, we observe how the images are affected by changes in the incident wavelength and in the object parameters. The changes in the images will indicate how the collected super-resolution data relates to the object's properties.

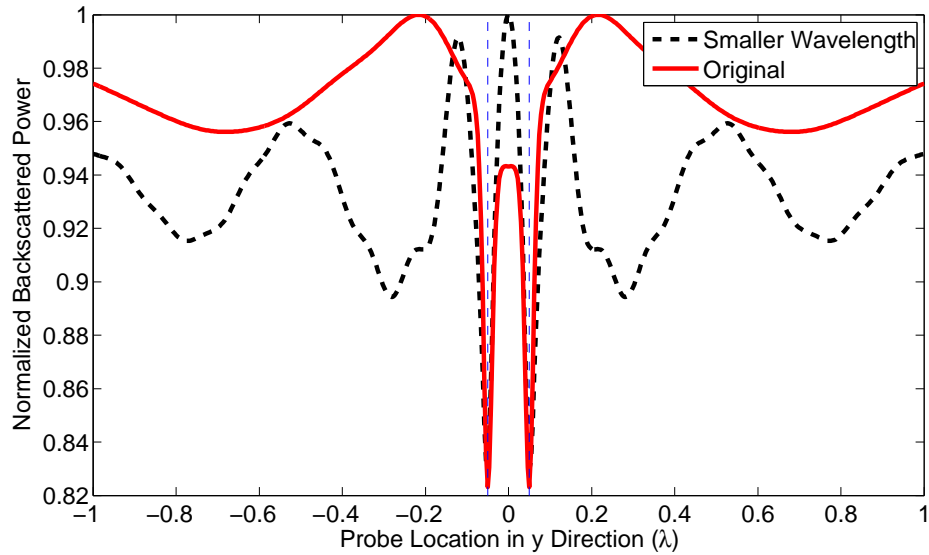


Figure 7.9: The ANSOM images for TE polarization with different incident wavelengths are shown.

The main advantage of ANSOM is that we can obtain higher resolution images without decreasing the incident wavelength. In Figure 7.9, the normalized incident wavelength is compared to an incident wavelength of half the size. The two sets of image data have had their maximum amplitude's normalized in order to compare their contours rather than their overall power levels. The resolution of the smaller incident wavelength may be slightly better because we can observe the higher peak between the two object cylinders. However, the super-resolution achievement at this new wavelength is only $\lambda/5$.

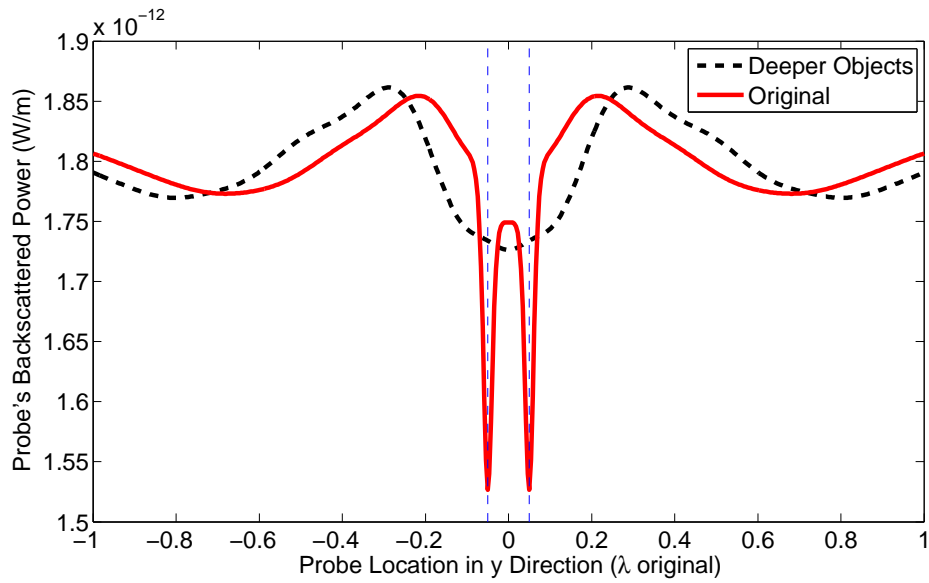


Figure 7.10: The ANSOM images for TE polarization with different object cylinder depths are shown.

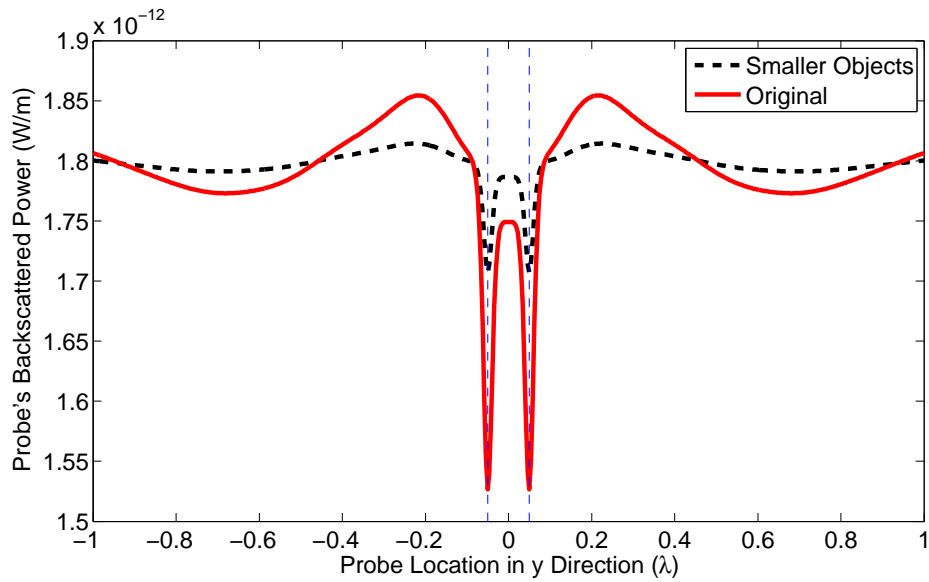


Figure 7.11: The ANSOM images for TE polarization with different object cylinder radii are shown.

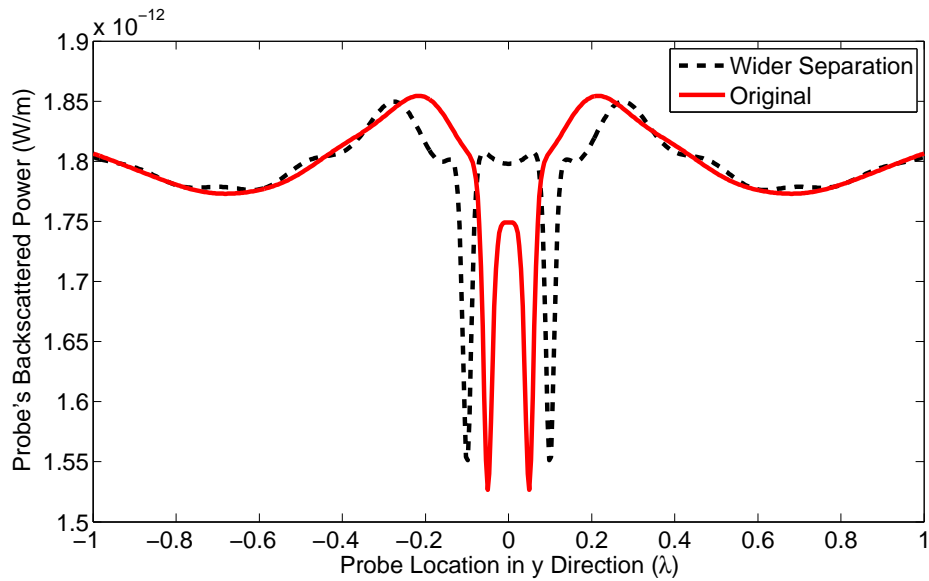


Figure 7.12: The ANSOM images for TE polarization with different object cylinder separation distances are shown.

In the last three simulations we compare the images produced by varying the object's properties. In Figure 7.10, the effect of burying the object cylinders ten times deeper within the dielectric half-space is observed. After burying the object cylinders deeper, we can no longer recover their evanescent fields at the image plane because evanescent fields are only local to the surface of a scattering body. Therefore, ANSOM is only useful at recovering super-resolution data for features within a very limited surface depth of the object. However, ANSOM still detects the effects of buried features even if it cannot resolve them. In Figure 7.11, the effect of decreasing the object cylinders' radii by one half is observed. The effect of changing the radii is clearly distinguishable from the effect of burying the cylinders deeper. The primary outcome from modifying the cylinder radii is the change in amplitude of the object cylinders' scattering and consequently of the recovered image contrast. In Figure 7.12, the effect of separating the cylinders with twice as much distance is observed. The shape of the recovered image follows

the location of the cylinders which may indicate that geometrical information about the object cylinders could be recovered using this technique.

7.9 Conclusion

The electromagnetic scattering models developed in the previous chapters were applied to simulations of ANSOM. The power scattered by the probe-tip was shown to be proportional to the square magnitude of the tangential electric field for a PEC cylinder. For evanescent waves, the electromagnetic field intensity is not directly proportional to the square magnitude of the electric field. This implies that the information collected through ANSOM will depend on the material properties of the probe-tip and the polarization of the incident electromagnetic field.

The effects of vibrating the probe-shaft and demodulating the received field through homodyne detection were analyzed. The vibration of the probe-shaft modulates its scattered field in a non-linear way, leading to a wide range of harmonics. The results of our simulations demonstrated that the third harmonic demodulation may contain higher resolution than the first two harmonics, but this effect was polarization dependent.

The probe-tip scatters both the incident field and the scattered field from the object. These two fields add together to create interference patterns that are not present in traditional images that only contain the scattered fields. These interference patterns must be taken into account when interpreting the ANSOM images.

One of the most important assumptions in ANSOM is that the probe-tip does not distort the near-field through multiple scattering. This assumption was tested by removing the tip-object coupling matrix \mathbf{S} in the scattering calculation. This new image displayed noticeable changes in field shape compared to the original ANSOM image, proving that tip-object coupling can have significant effects.

One of the most important aspects of ANSOM imaging was also characterized: the distance from the probe-tip to the object. Due to the exponential decay of the evanescent fields, the simulated ANSOM images lost resolution drastically as the probe-tip was separated from the object.

Varying the object properties and observing the changes in the images allowed us to better understand the capabilities of ANSOM. The super-resolution data was produced by evanescent fields that were local to the surface of scattering bodies. Buried bodies needed to be within a fraction of a wavelength from the surface for their evanescent fields to be recovered from the other side of the surface. Our observations from moving the object cylinders laterally across the surface indicate that it may be possible to recover the geometrical and optical properties of surface features using these techniques.

Chapter 8

Summary and Conclusions

Super-resolution imaging is possible if evanescent field data can be collected. When an evanescent field scatters from a subwavelength object it partially converts into radiation that is able to transfer energy into the far-field where it can be detected. To characterize this phenomenon and to simulate the super-resolution imaging process, four electromagnetic scattering models were developed. A cylindrical wave decomposition was used to satisfy the boundary conditions for the cylinders directly. These analytical solutions have several advantages over numerical methods including:

- A) No spatial discretization
- B) No limits to far-field modelling
- C) More efficient modelling of high spatial resolutions
- D) Efficient modelling of small scattering bodies
- E) A solution in terms of compact scattering coefficients
- F) A specific breakdown of scattering interactions is accessible

Hence, for looking at specific evanescent wave scattering phenomena the analytical solutions are ideal.

In Chapter 2, the analytical solution for the scattering from a cylinder was extended to include evanescent field incidence. The near-field of a Gaussian beam was scattered from a dielectric cylinder and the conversion of evanescent waves into radiation was observed. The conversion was attributed to

the spatial redistribution of the electromagnetic fields during the scattering. In order to compute the scattering, the incident evanescent field had to be represented by cylindrical waves composed of Bessel functions of the first kind. When the sum of cylindrical waves was truncated, the evanescent field only converged within a specific radial distance from the origin. This convergence is important because it limits the use of the Graf addition theorem in translating evanescent fields represented in this way. Using a sum of Gaussian beams to represent an arbitrary field with evanescent components was found to be inefficient because the evanescent components make numerical integration necessary.

The proper truncation of cylindrical wave modes in the two-dimensional scattering from cylinders was investigated in Chapter 3. Previous authors gave linear estimates for proper modal truncation [26–28], but one linear approximation cannot suffice for cylinders of all sizes. Therefore, estimates for minimum mode limits were formed for cylinders with small, medium, and large radii with respect to the wavelength. The ratio of the cylinder radius to the wavelength was the primary factor in determining the appropriate mode limit. If too few modes were used in the scattering calculation, the fields were misrepresented. If too many modes were used in multiple scattering calculations, the matrix inversion became ill-conditioned, leading to numerical errors. To maximize the accuracy of the scattering calculation, the mode limit was chosen above a minimum limit for accuracy and below a maximum limit for matrix conditioning.

In Chapter 4, the vector plane-wave-spectrum (VPWS) was used to introduce arbitrary radiative and evanescent field incidence into the multiple scattering from dielectric and conducting cylinders. The solution was formed into a T-matrix, which multiplies the incident field coefficients to produce the scattering coefficients. A method of evanescent field analysis was proposed using a grating of cylinders. The grating of cylinders converted an incident evanescent wave into a radiative beam that propagated at an angle

that depended on the spatial frequency of the incident field. The total angular distribution of converted beams could then be used to determine the spatial frequency content of the incident evanescent field.

In many imaging scenarios the objects under consideration are placed on top of a planar surface or buried inside of a dielectric. To accommodate these cases, the scattering from cylinders was adapted to include a dielectric half-space. Two methods for calculating the multiple scattering from cylinders near a dielectric half-space are the Fourier series method and the plane-wave integral method. In Chapter 5 the application of a Fourier series to transform the planar reflection coefficients into an angular form was introduced into vector electromagnetic scattering for the first time. The Fourier series method and the plane-wave integral method were derived alongside each other in order to draw parallels between the two methods. The methods would have been exactly equivalent except for the fact that the Fourier series only converged a limited distance into the complex domain. This convergence depended on the form of the reflection coefficients for the planar interface separating the two dielectric half-spaces. This limited convergence into the complex domain meant that some of the evanescent field interactions between the cylinders and the planar interface were misrepresented. To account for these errors, evanescent field correction terms were derived. The plane-wave integral method was always accurate for evanescent fields, but it required a significant amount of numerical integration.

The scattering from cylinders on both sides of a dielectric half-space was considered for the first time in Chapter 6. This model allowed us to simulate a scanning probe cylinder on one side of the half-space and object cylinders on the opposite side. The scanning probe cylinder could be used to scatter evanescent fields emanating from the object cylinders buried in the half-space, converting them into radiation. This radiation could then be collected and used to form a super-resolution image of the buried cylinders as demonstrated in Chapter 7. The multiple scattering between cylinders on

opposite sides of a dielectric half-space was analyzed using the Sommerfeld integral to transform cylindrical waves into plane-waves. To eliminate the need for numerical integration when applying the transformation, an approximation based on the method of stationary phase was introduced. For the multiple scattering between cylinders in opposite half-spaces, the cylinders needed to be sufficiently separated from each other for the approximation to be accurate. For the multiple scattering between the cylinders and the planar interface, the cylinders need to be sufficiently separated from the interface for the approximation to be accurate. The approximation was necessary because direct numerical integration became extremely difficult when the separation distances were large.

Finally, in Chapter 7 the previously derived scattering models were used to simulate ANSOM images. The collected image data was demonstrated to be dependant on the scattering properties of the probe-tip and the polarization. Because of the skewed proportion of electric to magnetic fields that occurs in evanescent waves, TE polarization recovered better resolution than TM polarization, using a PEC cylinder. The modulation and demodulation of the probe-tip was characterized using homodyne detection with a large reference signal. The difference in the results obtained using the first three harmonics was attributed to the non-linear response of the scattered power to the modulation. The effects of tip-object interactions were demonstrated explicitly by removing the matrix that couples the tip to the object when computing the scattering. A smaller tip prevented tip-object distortion but also reduced the signal to noise ratio. A major consideration when interpreting ANSOM images was that the probe-tip scatters both the incident field and the scattered field from the object. Traditional imaging methods only recover the scattered field from the object. The addition of both the incident field and the scattered field caused interference patterns to arise in the image. To demonstrate the underlying super-resolution principles, the relationship between resolution and tip-object distance was observed for distances from

$\lambda/100$ to $\lambda/2$. Finally, simulations varying the object's properties and the incident wavelength were produced to uncover the limitations of the image data. The super-resolution data was shown to contain information primarily about the near-surface of the object.

8.1 Future Work

The electromagnetic scattering models derived in chapters 2, 4, 5, and 6 are useful for many applications that have not been considered in this thesis, including the design and analysis of metamaterials and photonic crystals, and ground penetrating radar (GPR) simulations.

Metamaterials are man-made structures that are able to mimic unique material properties such as negative permittivities, negative permeabilities and low/zero refractive index [3]. The metamaterial must be made out of structures with a subwavelength periodicity so that it appears homogeneous to the wavelength under consideration. The electromagnetic scattering models produced in the preceding chapters can be used to model a metamaterial as an array of cylinders arranged in a repeatable pattern. The analytical solutions are particularly helpful in the design process as they provide a lot of information about the coupling between cylinders, which ultimately provides the effective material properties. These models are particularly well-suited for simulating wire media metamaterials as proposed by Pendry et al. [107]. These metamaterials are composed of thin conducting wires positioned in a grid.

Metamaterials are often used to create double negative materials in which the permittivity and the permeability of the material are negative. In this case the refractive index becomes negative but the impedance remains positive. These double negative materials (DNG) can be used as a super-lens, capable of providing super-resolution images. The double negative material enhances evanescent fields that are incident upon its surface by switching the

exponential decay into exponential growth. Other applications for metamaterials include artificial magnetism for magnetic resonance imaging (MRI) [108] and phase compensation in transmission lines.

The models that have been presented are also excellent for simulating two dimensional photonic crystals composed of cylindrical structures. Photonic crystals are periodic structures that contain elements of higher and lower permittivities. Unlike metamaterials, the photonic crystal's size and periodicity is on the order of the wavelength. The material effects due to diffraction between elements cannot be described by an effective permittivity and permeability. However, photonic crystals can produce photonic band gaps, which allow for the control and manipulation of light. Photonic crystals have even been demonstrated to produce effects similar to negative index materials [108].

GPR simulations can be run using the models derived in chapters 5 and 6, where cylinders are buried in a lossy half-space [103]. Ground penetrating radar is useful in for remote sensing of the Earth's subsurface, and imaging underground landmines, pipes, conduits and tunnels [39–41]. To model an electromagnetic wave penetrating the surface of the earth, the dielectric half-space can be made lossy by incorporating a complex permittivity. The buried objects can be approximated with arrangements of cylinders. In addition, the model with cylinders in both half-spaces, presented in Chapter 6, could be used to model objects both above and below the surface of the earth to account for all the multiple scattering effects.

Bibliography

- [1] H. Volkmann, “Ernst Abbe and his work,” *Applied Optics*, vol. 5, no. 11, pp. 1720–1731, 1966.
- [2] F. de Fornel, *Evanescent waves: from Newtonian optics to atomic optics*. Springer Verlag, 2001.
- [3] N. Engheta and R. W. Ziolkowski, *Metamaterials: physics and engineering explorations*. USA: John Wiley & Sons, Inc., 2006.
- [4] G. Mie, “Considerations on the optics of turbid media, especially colloidal metal sols,” *Annalen der Physik*, vol. 25, pp. 377–442, 1908.
- [5] L. V. Lorenz, “Upon the light reflected and refracted by a transparent sphere,” *Vidensk. Sel’sk. Shrifter*, vol. 6, pp. 1–62, 1890.
- [6] G. Gouesbet, “Generalized lorenz-mie theories, the third decade: A perspective,” *Journal of Quantitative Spectroscopy and Radiative Transfer*, vol. 110, no. 14-16, pp. 1223–1238, 2009.
- [7] L. Rayleigh, “The dispersal of light by a dielectric cylinder,” *Philosophical Magazine Series 6*, vol. 36, no. 215, pp. 365–376, 1918.
- [8] M. Polewski and J. Mazur, “Scattering by an array of conducting, lossy dielectric, ferrite and pseudochiral cylinders,” *Progress In Electromagnetics Research*, vol. 38, pp. 283–310, 2002.

- [9] T. Rao, "Scattering by a radially inhomogeneous cylindrical dielectric shell due to an incident Gaussian beam," *Canadian Journal of Physics*, vol. 67, no. 5, pp. 471–475, 1989.
- [10] Z. Wu and L. Guo, "Electromagnetic scattering from a multilayered cylinder arbitrarily located in a Gaussian beam, a new recursive algorithms," *Journal of Electromagnetic Waves and Applications*, vol. 12, no. 6, pp. 725–726, 1998.
- [11] J. R. Wait, "Scattering of a plane wave from a circular dielectric cylinder at oblique incidence," *Canadian Journal of Physics*, vol. 33, no. 5, pp. 189–195, 1955.
- [12] T. Kojima and Y. Yanagiuchi, "Scattering of an offset two-dimensional Gaussian beam wave by a cylinder," *Journal of Applied Physics*, vol. 50, no. 1, pp. 41–46, 1979.
- [13] E. Zimmermann, R. Dandliker, N. Souli, and B. Krattiger, "Scattering of an off-axis Gaussian beam by a dielectric cylinder compared with a rigorous electromagnetic approach," *Journal of the Optical Society of America A*, vol. 12, no. 2, pp. 398–403, 1995.
- [14] C. Yeh, "The diffraction of waves by a penetrable ribbon," *Journal of Mathematical Physics*, vol. 4, no. 1, pp. 65–71, 1963.
- [15] L. W. Davis, "Theory of electromagnetic beams," *Physical Review A*, vol. 19, no. 3, pp. 1177–1179, 1979.
- [16] H. Kogelnik and T. Li, "Laser beams and resonators," *Applied Optics*, vol. 5, no. 10, pp. 1550–1567, 1966.
- [17] P. C. Clemmow, *The plane wave spectrum representation of electromagnetic fields*. Oxford, England: Pergamon Press, 1966.

- [18] N. Alexopoulos and P. Park, "Scattering of waves with normal amplitude distribution from cylinders," *IEEE Transactions on Antennas and Propagation*, vol. 20, no. 2, pp. 216–217, 1972.
- [19] S. Kozaki, "A new expression for the scattering of a Gaussian beam by a conducting cylinder," *IEEE Transactions on Antennas and Propagation*, vol. 30, no. 5, pp. 881–887, 1982.
- [20] —, "Scattering of a Gaussian beam by a homogeneous dielectric cylinder," *Journal of Applied Physics*, vol. 53, no. 11, pp. 7195–7200, 1982.
- [21] J. J. Wen and M. A. Breazeale, "A diffraction beam field expressed as the superposition of Gaussian beams," *The Journal of the Acoustical Society of America*, vol. 83, no. 5, pp. 1752–1756, 1988.
- [22] V. Twersky, "Multiple scattering of radiation by an arbitrary configuration of parallel cylinders," *The Journal of the Acoustical Society of America*, vol. 24, no. 1, pp. 42–46, 1952.
- [23] J. E. Burke, D. Censor, and V. Twersky, "Exact inverse separation series for multiple scattering in two dimensions," *The Journal of Acoustical Society of America*, vol. 37, no. 1, pp. 5–13, 1965.
- [24] G. Olaofe, "Scattering by an arbitrary configuration of parallel circular cylinders," *Journal of the Optical Society of America*, vol. 60, no. 9, pp. 1233–1236, 1970.
- [25] —, "Scattering by two cylinders," *Radio Science*, vol. 5, no. 11, pp. 1351–1360, 1970.
- [26] J. W. Young and J. C. Bertrand, "Multiple scattering by two cylinders," *The Journal of the Acoustical Society of America*, vol. 58, no. 6, pp. 1190–1195, 1975.

- [27] A. Z. Elsherbeni, "A comparative study of two-dimensional multiple scattering techniques," *Radio Science*, vol. 29, no. 4, pp. 1023–1033, 1994.
- [28] H. A. Ragheb and M. Hamid, "Scattering by N parallel conducting circular cylinders," *International Journal of Electronics*, vol. 59, no. 4, pp. 407–421, 1985.
- [29] S. J. Bever and J. P. Allebach, "Multiple scattering by a planar array of parallel dielectric cylinders," *Applied Optics*, vol. 31, no. 18, pp. 3524–3532, 1992.
- [30] B. H. Henin, A. Z. Elsherbeni, and M. H. A. Sharkawy, "Oblique incidence plane wave scattering from an array of circular dielectric cylinders," *Progress In Electromagnetics Research*, vol. 68, pp. 261–279, 2007.
- [31] T. Kojima, A. Ishikura, and M. Ieguchi, "Scattering of Hermite-Gaussian beams by two parallel conducting cylinders," *Report of the Technical Group on Antennas and Propagation TGAP-83-36 (Institute of Electronics and Communications Engineers of Japan)*, 1983.
- [32] H. Sugiyama and S. Kozaki, "Multiple scattering of a gaussian beam by two cylinders having different radii," *Institute of Electronics, Information, and Communications Engineers Transactions*, vol. 65, no. 3, pp. 173–174, 1982.
- [33] M. Yokota, T. Takenaka, and O. Fukumitsu, "Scattering of a Hermite-Gaussian beam mode by parallel dielectric circular cylinders," *Journal of the Optical Society of America A*, vol. 3, no. 4, pp. 580–586, 1986.
- [34] A. Z. Elsherbeni, M. Hamid, and G. Tian, "Iterative scattering of a Gaussian beam by an array of circular conducting and dielectric

- cylinders,” *Journal of Electromagnetic Waves and Applications*, vol. 7, no. 10, pp. 1323–1342, 1993.
- [35] J. Yang, L. W. Li, K. Yasumoto, and C. H. Liang, “Two-dimensional scattering of a Gaussian beam by a periodic array of circular cylinders,” *IEEE Transactions on Geoscience and Remote Sensing*, vol. 43, no. 2, pp. 280–285, 2005.
- [36] M. Fink, “Time-reversal waves and super resolution,” in *Journal of Physics: Conference Series*, vol. 124. Institute of Physics Publishing, 2008.
- [37] G. Lerosey, J. de Rosny, A. Tourin, and M. Fink, “Focusing beyond the diffraction limit with far-field time reversal,” *Science*, vol. 315, no. 5815, pp. 1120–1122, 2007.
- [38] O. Malyuskin and V. Fusco, “Far field subwavelength source resolution using phase conjugating lens assisted with evanescent-to-propagating spectrum conversion,” *IEEE Transactions on Antennas and Propagation*, vol. 58, no. 2, pp. 459–468, 2010.
- [39] S. Ahmed and Q. A. Naqvi, “Electromagnetic scattering from a perfect electromagnetic conductor cylinder buried in a dielectric half-space,” *Progress In Electromagnetics Research*, vol. 78, pp. 25–38, 2008.
- [40] F. Ciambra, F. Frezza, L. Pajewski, and G. Schettini, “A spectral-domain solution for the scattering problem of a circular cylinder buried in a dielectric half space,” *Progress In Electromagnetics Research*, vol. 38, pp. 223–252, 2002.
- [41] F. Frezza, L. Pajewski, C. Ponti, and G. Schettini, “Scattering by dielectric circular cylinders in a dielectric slab,” *Journal of the Optical Society of America A*, vol. 27, no. 4, pp. 687–695, 2010.

- [42] V. Twersky, “Multiple scattering of radiation by an arbitrary planar configuration of parallel cylinders and by two parallel cylinders,” *Journal of Applied Physics*, vol. 23, no. 4, pp. 407–414, 1952.
- [43] J. Bertrand and J. Young, “Multiple scattering between a cylinder and a plane,” *Journal of the Acoustical Society of America*, vol. 60, no. 6, pp. 1265–1269, 1976.
- [44] T. C. Rao and R. Barakat, “Plane-wave scattering by a conducting cylinder partially buried in a ground plane. 1. TM case,” *Journal of the Optical Society of America A*, vol. 6, no. 9, pp. 1270–1280, 1989.
- [45] —, “Plane-wave scattering by a conducting cylinder partially buried in a ground plane II: TE case,” *Journal of the Optical Society of America A*, vol. 8, no. 12, pp. 1986–1990, 1991.
- [46] G. Videen and D. Ngo, “Light scattering from a cylinder near a plane interface: theory and comparison with experimental data,” *Journal of the Optical Society of America A*, vol. 14, no. 1, pp. 70–78, 1997.
- [47] A. Coatanhay and J. M. Conoir, “Scattering near a plane interface using a generalized method of images approach,” *Journal of Computational Acoustics*, vol. 12, no. 2, pp. 233–256, 2004.
- [48] —, “Scattering by an elastic cylinder embedded in a fluid sediment. generalized method of images (GMI) approach,” *Wave Motion*, vol. 44, no. 2, pp. 77–91, 2006.
- [49] G. Cincotti, F. Gori, M. Santarsiero, F. Frezza, F. Furno, and G. Schettini, “Plane wave expansion of cylindrical functions,” *Optics Communications*, vol. 95, no. 4-6, pp. 192–198, 1993.
- [50] R. Borghi, F. Frezza, C. Santini, G. Schettini, and M. Santarsiero, “Numerical study of the reflection of cylindrical waves of arbitrary

- order by a generic planar interface,” *Journal of Electromagnetic Waves and Applications*, vol. 13, no. 1, pp. 27–50, 1999.
- [51] R. Borghi, F. Frezza, M. Santarsiero, C. Santini, and G. Schettini, “A quadrature algorithm for the evaluation of a 2D radiation integral with a highly oscillating kernel,” *Journal of Electromagnetic Waves and Applications*, vol. 14, no. 10, pp. 1353–1370, 2000.
- [52] F. Frezza, G. Schettini, F. Gori, M. Santarsiero, and F. Santini, “Quasi-optical launchers for lower hybrid waves: a full wave approach,” *Nuclear Fusion*, vol. 34, no. 9, pp. 1239–1246, 1994.
- [53] R. Borghi, F. Gori, M. Santarsiero, F. Frezza, and G. Schettini, “Plane-wave scattering by a perfectly conducting circular cylinder near a plane surface: cylindrical-wave approach,” *Journal of the Optical Society of America A*, vol. 13, no. 3, pp. 483–493, 1996.
- [54] —, “Plane-wave scattering by a set of perfectly conducting circular cylinders in the presence of a plane surface,” *Journal of the Optical Society of America A*, vol. 13, no. 12, pp. 2441–2452, 1996.
- [55] M. D. Vico, F. Frezza, L. Pajewski, and G. Schettini, “Scattering by a finite set of perfectly conducting cylinders buried in a dielectric half-space: A spectral-domain solution,” *IEEE Transactions on Antennas and Propagation*, vol. 53, no. 2, pp. 719–727, 2005.
- [56] S. C. Lee and J. A. Grzesik, “Light scattering by closely spaced parallel cylinders embedded in a semi-infinite dielectric medium,” *Journal of the Optical Society of America A*, vol. 15, no. 1, pp. 163–173, 1998.
- [57] F. Frezza, L. Pajewski, C. Ponti, and G. Schettini, “Scattering by perfectly conducting circular cylinders buried in a dielectric slab through the cylindrical wave approach,” *IEEE Transactions on Antennas and Propagation*, vol. 57, no. 4, pp. 1208–1217, 2009.

- [58] S. C. Lee, “Light scattering by closely spaced parallel cylinders embedded in a finite dielectric slab,” *Journal of the Optical Society of America A*, vol. 16, no. 6, pp. 1350–1361, 1999.
- [59] E. H. Synge, “A suggested method for extending the microscopic resolution into the ultramicroscopic region,” *The London, Edinburgh, and Dublin Philosophical Magazine and Journal of Science*, vol. 6, no. 35, pp. 356–362, 1928.
- [60] E. Ash and G. Nicholls, “Super-resolution aperture scanning microscope,” *Nature*, vol. 237, pp. 510–512, 1972.
- [61] H. Furukawa and S. Kawata, “Analysis of image formation in a near-field scanning optical microscope: effects of multiple scattering,” *Optics Communications*, vol. 132, no. 1-2, pp. 170–178, 1996.
- [62] R. Carminati, A. Madrazo, M. Nieto-Vesperinas, and J. J. Greffet, “Optical content and resolution of near-field optical images: Influence of the operating mode,” *Journal of Applied Physics*, vol. 82, no. 2, pp. 501–509, 1997.
- [63] F. Zenhausern, M. Oboyle, and H. Wickramasinghe, “Apertureless near-field optical microscope,” *Applied Physics Letters*, vol. 65, no. 13, pp. 1623–1625, 1994.
- [64] J. H. Kim and K. B. Song, “Recent progress of nano-technology with NSOM,” *Micron*, vol. 38, no. 4, pp. 409–426, 2007.
- [65] V. Sandoghdar and J. Mlynek, “Prospects of apertureless SNOM with active probes,” *Journal of Optics A: Pure and Applied Optics*, vol. 1, no. 4, pp. 523–530, 1999.
- [66] P. M. Adam, P. Royer, R. Laddada, and J. L. Bijeon, “Apertureless near-field optical microscopy: influence of the illumination conditions

- on the image contrast,” *Applied Optics*, vol. 37, no. 10, pp. 1814–1819, 1998.
- [67] W. Chen and Q. Zhan, “Numerical study of an apertureless near field scanning optical microscope probe under radial polarization illumination,” *Optics Express*, vol. 15, no. 7, pp. 4106–4111, 2007.
- [68] B. Knoll and F. Keilmann, “Enhanced dielectric contrast in scattering-type scanning near-field optical microscopy,” *Optics Communications*, vol. 182, no. 4, pp. 321–328, 2000.
- [69] Z. H. Kim, B. Liu, and S. R. Leone, “Nanometer-scale optical imaging of epitaxially grown GaN and InN islands using apertureless near-field microscopy,” *The Journal of Physical Chemistry B*, vol. 109, no. 17, pp. 8503–8508, 2005.
- [70] Z. H. Kim, S. H. Ahn, B. Liu, and S. R. Leone, “Nanometer-scale dielectric imaging of semiconductor nanoparticles: Size-dependent dipolar coupling and contrast reversal,” *Nano letters*, vol. 7, no. 8, pp. 2258–2262, 2007.
- [71] Z. H. Kim and S. R. Leone, “Polarization-selective mapping of near-field intensity and phase around gold nanoparticles using apertureless near-field microscopy,” *Optics Express*, vol. 16, no. 3, pp. 1733–1741, 2008.
- [72] G. Gouesbet, “Interaction between an infinite cylinder and an arbitrary-shaped beam,” *Applied Optics*, vol. 36, no. 18, pp. 4292–4304, 1997.
- [73] K. F. Ren, G. Grehan, and G. Gouesbet, “Scattering of a Gaussian beam by an infinite cylinder in the framework of generalized Lorenz-Mie theory: formulation and numerical results,” *Journal of the Optical Society of America A*, vol. 14, no. 11, pp. 3014–3025, 1997.

- [74] L. Mees, K. F. Ren, G. Grehan, and G. Gouesbet, "Scattering of a Gaussian beam by an infinite cylinder with arbitrary location and arbitrary orientation: numerical results," *Applied Optics*, vol. 38, no. 9, pp. 1867–1876, 1999.
- [75] H. J. Eom, *Electromagnetic wave theory for boundary-value problems: an advanced course on analytical methods*. Germany: Springer-Verlag, 2004.
- [76] G. Agrawal and D. Pattanayak, "Gaussian beam propagation beyond the paraxial approximation," *Journal of the Optical Society of America*, vol. 69, no. 4, pp. 575–578, 1979.
- [77] P. Varga and P. Torok, "The Gaussian wave solution of maxwell's equations and the validity of scalar wave approximation," *Optics Communications*, vol. 152, no. 1-3, pp. 108–118, 1998.
- [78] E. V. Jull, *Aperture Antennas and Diffraction Theory*. Stevenage, UK: Peter Peregrinus Ltd., 1981.
- [79] J. E. Harvey, "Fourier treatment of near-field scalar diffraction theory," *American Journal of Physics*, vol. 47, no. 11, pp. 974–980, 1979.
- [80] S. Kozaki and H. Sakurai, "Characteristics of a Gaussian beam at a dielectric interface," *Journal of the Optical Society of America*, vol. 68, no. 4, pp. 508–514, 1978.
- [81] N. W. McLachlan, *Bessel functions for engineers*. London, UK: Oxford University Press, 1934.
- [82] J. Mathews and R. L. Walker, *Mathematical Methods of Physics*. New York: W. A. Benjamin Inc., 1964.

- [83] T. G. Tsuei and P. W. Barber, “Multiple scattering by two parallel dielectric cylinders,” *Applied Optics*, vol. 27, no. 16, pp. 3375–3381, 1988.
- [84] B. Peterson and S. Strom, “T matrix for electromagnetic scattering from an arbitrary number of scatterers and representations of E (3),” *Physical Review D*, vol. 8, no. 10, pp. 3661–3678, 1973.
- [85] P. Pawliuk and M. Yedlin, “Gaussian beam scattering from a dielectric cylinder, including the evanescent region,” *Journal of the Optical Society of America A*, vol. 26, no. 12, pp. 2558–2566, 2009.
- [86] D. Marks and P. S. Carney, “Near-field diffractive elements,” *Optics Letters*, vol. 30, no. 14, pp. 1870–1872, 2005.
- [87] Y. V. Gulyaev, Y. N. Barabanenkov, M. Y. Barabanenkov, and S. Nikitov, “Optical theorem for electromagnetic field scattering by dielectric structures and energy emission from the evanescent wave,” *Physical Review E*, vol. 72, no. 2, 2005.
- [88] H. Guo, J. Chen, and S. Zhuang, “Vector plane wave spectrum of an arbitrary polarized electromagnetic wave,” *Optics Express*, vol. 14, no. 6, pp. 2095–2100, 2006.
- [89] B. G. Korenev, *Bessel functions and their applications*. USA: CRC Press, 2002.
- [90] C. A. Balanis, *Advanced Engineering Electromagnetics*. USA: John Wiley and Sons, Inc., 1989.
- [91] R. Ruppin, “Scattering of electromagnetic radiation by a perfect electromagnetic conductor cylinder,” *Journal of Electromagnetic Waves and Applications*, vol. 20, no. 13, pp. 1853–1860, 2006.

- [92] P. Pawliuk and M. Yedlin, “Scattering from cylinders using the two-dimensional vector plane wave spectrum,” *Journal of the Optical Society of America A*, vol. 28, no. 6, pp. 1177–1184, 2011.
- [93] Y. Wang, Y. Zhang, M. He, and L. Guo, “Calculation of electromagnetic scattering from a two-dimensional target in the vicinity of a plane surface by a hybrid method,” *Journal of the Optical Society of America A*, vol. 25, no. 6, pp. 1232–1239, 2008.
- [94] A. Madrazo and M. Nieto-Vesperinas, “Scattering of electromagnetic waves from a cylinder in front of a conducting plane,” *Journal of the Optical Society of America A*, vol. 12, no. 6, pp. 1298–1309, 1995.
- [95] P. B. Wong, G. L. Tyler, J. E. Baron, E. M. Gurrola, and R. A. Simpson, “A three-wave FDTD approach to surface scattering with applications to remote sensing of geophysical surfaces,” *IEEE Transactions on Antennas and Propagation*, vol. 44, no. 4, pp. 504–514, 1996.
- [96] M. Abramowitz and I. Stegun, *Handbook of mathematical functions*. Washington, DC: US Government Printing Office, 1965.
- [97] E. B. Saff and A. D. Snider, *Fundamentals of complex analysis*, 3rd ed. New Jersey, USA: Pearson Education Inc., 2003.
- [98] A. Sommerfeld, *Partial differential equations in physics*. New York, NY: Academic Press Inc., 1949.
- [99] P. Pawliuk and M. Yedlin, “Truncating cylindrical wave modes in two-dimensional multiple scattering,” *Optics Letters*, vol. 35, no. 23, pp. 3997–3999, 2010.
- [100] K. Wang, A. Barkan, and D. M. Mittleman, “Propagation effects in apertureless near-field optical antennas,” *Applied Physics Letters*, vol. 84, no. 2, pp. 305–307, 2004.

- [101] P. Valle, F. Gonzalez, and F. Moreno, “Electromagnetic wave scattering from conducting cylindrical structures on flat substrates: study by means of the extinction theorem,” *Applied Optics*, vol. 33, no. 3, pp. 512–523, 1994.
- [102] Q. H. Liu and G. X. Fan, “Simulations of GPR in dispersive media using a frequency-dependent PSTD algorithm,” *IEEE Transactions on Geoscience and Remote Sensing*, vol. 37, no. 5, pp. 2317–2324, 1999.
- [103] G. X. Fan, Q. H. Liu, and J. S. Hesthaven, “Multidomain pseudospectral time-domain simulations of scattering by objects buried in lossy media,” *IEEE Transactions on Geoscience and Remote Sensing*, vol. 40, no. 6, pp. 1366–1373, 2002.
- [104] M. Born and E. Wolf, *Principles of optics: electromagnetic theory of propagation, interference and diffraction of light*, 6th ed. Oxford, England: Pergamon Press Ltd., 1980.
- [105] M. Kline and I. W. Kay, *Electromagnetic theory and geometrical optics*. New York, NY: Interscience Publishers, 1965.
- [106] G. J. Gbur, *Mathematical Methods for Optical Physics and Engineering*. Cambridge, UK: Cambridge University Press, 2011.
- [107] J. B. Pendry, A. Holden, W. Stewart, and I. Youngs, “Extremely low frequency plasmons in metallic mesostructures,” *Physical Review Letters*, vol. 76, no. 25, pp. 4773–4776, 1996.
- [108] D. Smith, J. Pendry, and M. Wiltshire, “Metamaterials and negative refractive index,” *Science*, vol. 305, no. 5685, pp. 788–792, 2004.

Appendix A

Diffraction Limit

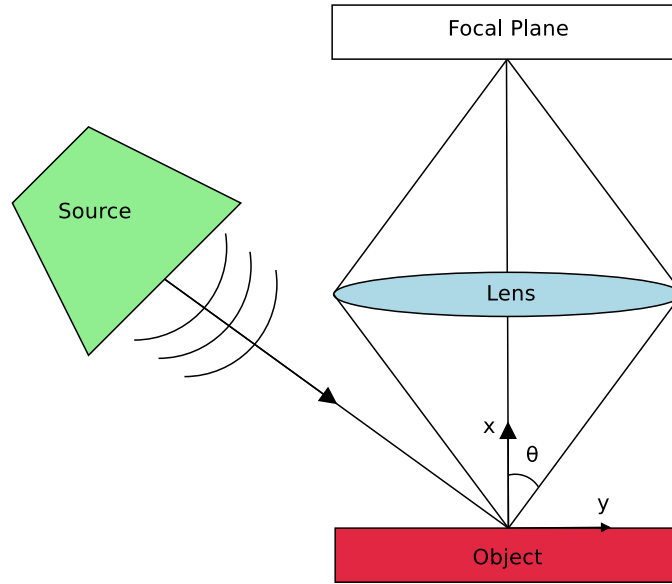


Figure A.1: A basic imaging setup is shown, copied from Figure 1.1.

Referring to the imaging setup in Figure A.1, the diffraction limit can be derived using Fourier optics. Since plane-waves are the eigenfunctions of the homogeneous wave equation in Cartesian coordinates, any arbitrary field can be represented as a sum of plane-waves. Therefore, the scattered field emanating from the object's surface can be described by a plane-wave spectrum

$$V(x, y) = \frac{1}{2\pi} \int_{-\infty}^{\infty} F(k_y) \exp(-jk_y y - jk_x x) dk_y, \quad (\text{A.1})$$

where V is an electric or magnetic field component of the scattered field from the object's surface. The time dependence $\exp(j\omega t)$ is assumed throughout.

The function $F(k_y)$ is defined by the distribution of V along the plane $x = 0$:

$$F(k_y) = \int_{-\infty}^{\infty} V(0, y) \exp(jk_y y) dy. \quad (\text{A.2})$$

Since the wavenumber is defined by $k = \omega\sqrt{\epsilon\mu}$, it must be constant unless the medium changes. Therefore, the x component of the wave-vector can be defined

$$k_x = \begin{cases} \sqrt{k^2 - k_y^2} & |k_y| \leq k \quad \text{radiative} \\ -j\sqrt{k_y^2 - k^2} & |k_y| > k \quad \text{evanescent} \end{cases}. \quad (\text{A.3})$$

The waves emanating from the object (A.1) disperse at various angles defined by $\delta = \arcsin(k_y/k)$. If the collecting lens is in the far-field, we can assume that these waves behave like rays travelling at an angle δ . The lens can only collect rays with a maximum angle of θ , or equivalently, a maximum k_y value of $k_{max} = k \sin(\theta)$. When backpropagated or refocused, the reconstruction of the original wave-field $V(0, y)$ will be

$$V_{rc}(0, y) = \frac{1}{2\pi} \int_{-k_{max}}^{k_{max}} F(k_y) \exp(-jk_y y) dk_y, \quad (\text{A.4})$$

which now has a spatial frequency limit of k_{max} . By the Nyquist sampling criteria for perfect reconstruction, the field V_{rc} needs to be sampled at a frequency $\frac{2k_{max}}{2\pi} = \frac{2n \sin(\theta)}{\lambda_0}$ samples/m, where λ_0 is the wavelength in free space. Inverting this spatial sampling gives the diffraction limit $d = \frac{\lambda_0}{2n \sin(\theta)}$ m/sample. From the sampling criteria, there is no information contained in the reconstructed image about points spaced closer than d apart.

The resolution can be increased by moving the lens closer to the object or by expanding the size of the lens. In the limiting case $\theta \rightarrow \pi/2$ and the resolution reaches $d = \lambda/2$. However, it is clear from the integration extents of (A.1) that infinite resolution exists at the surface of the object and the higher spatial frequencies are manifested as evanescent waves that exist only in the near-field due to their exponential decay. To recover resolution beyond $\lambda/2$, near-field scanning methods must be used to collect evanescent wave

information.

Appendix B

Truncating Cylindrical Wave Modes for Very Small Cylinders

As the cylinder size a becomes very small compared to the surrounding wavelength λ , the minimum mode limits for the two polarizations need to be considered more carefully. Applying Bessel function approximations for small arguments ($ka \rightarrow 0$) [96] to the single scattering coefficients for a PEC cylinder under TM illumination yields

$$-\frac{J_n(ka)}{H_n^{(2)}(ka)} \approx \begin{cases} -\frac{j\pi}{2\ln(ka)} & n = 0 \\ \frac{j\pi(ka/2)^{2|n|}}{|n|!(|n|-1)!} & n \neq 0 \end{cases} \quad (\text{B.1})$$

and under TE illumination yields

$$-\frac{J_n'(ka)}{H_n^{(2)'}(ka)} \approx \begin{cases} j\pi(ka/2)^2 & n = 0 \\ -\frac{j\pi(ka/2)^{2|n|}}{|n|!(|n|-1)!} & n \neq 0 \end{cases} \quad (\text{B.2})$$

The magnitude of the $n \neq 0$ modes for the two polarizations is equivalent for very small cylinders. However, the zeroth mode differs greatly between the two polarizations. Under TM polarization, the PEC cylinders continue to scatter strongly due to the induction of currents along the shafts of the cylinders. Under TE polarization, the zeroth mode approaches the same magnitude as the $n = \pm 1$ modes. Therefore, when modelling the scattering from very small PEC cylinders under TE illumination, it will always be

necessary to include the modes $n = -1, 0, 1$, but under TM illumination, the mode $n = 0$ will dominate over the much smaller modes $n = \pm 1$.

If the cylinder had magnetic properties then the reverse would be true. For a subwavelength PMC cylinder under TE illumination, the mode $n = 0$ will dominate over the much smaller modes $n = \pm 1$. Under TM illumination, the three modes $n = -1, 0, 1$ will approach the same magnitude.

Appendix C

Convergence of Finite Element Method Comparison

Table C.1: The mesh size parameters of the finite element method are compared to the resulting error.

maximum element size	minimum element size	maximum element growth rate	resolution of curvature	resolution of narrow regions	error (%)
19.8	3	2	1	0.9	31.65
7.8	0.36	1.5	0.6	1	1.89
4.02	0.018	1.3	0.3	1	0.55
2.22	0.0075	1.25	0.25	1	0.49

In Section 6.3, a comparison was made between the presented method and the finite element method. To demonstrate the convergence of the two methods, several mesh sizes were simulated for the finite element method and compared to a simulation of the presented method with high precision. A table of the mesh parameters and the resulting error between the two methods is shown in Table C.1. The primary sources of error are the discretization error for the differential equation and the shape mismatch of fitting triangular elements to circular scatterers. Simulating the presented method with even higher precision showed no apparent effect on the resulting error. The decrease in the convergence rate of the error for very fine mesh grids may be attributed to other possible sources of error such as the finite size of the spatial domain or the imperfection of the PMLs.